The Influence of Surface Finish on the Localized Dissipation of Frictional Power at Ultra-Mild Wear

Von der Fakultät für Ingenieurwissenschaften, Abteilung Maschinenbau und Verfahrenstechnik der

Universität Duisburg - Essen

zur Erlangung des akademischen Grades

eines

Doktors der Ingenieurwissenschaften

Dr.-Ing.

genehmigte Dissertation

von

Daniel Stickel

aus

Essen

Gutachter: Prof. Dr.-Ing. Alfons Fischer
Prof. Dr.ir. Rob Bosman

Tag der mündlichen Prüfung: 22.10.2015

Der Lebenslauf ist in der Online-Version aus Gründen des Datenschutzes nicht enthalten.

Abstract

Tribological systems are subjected to a steady decrease of friction and wear due to ecological and economical requirements. These guidelines can change the tribological loads and, therefore, result in more severe conditions. The need for maintaining wear as low as possible towards ultra-mild wear rates an integral approach is needed, which has to regard the contact conditions, surface topography, near- and sub-surface physical properties. The ultra-mild sliding wear rates, in the order of some nanometers per hour, are desired for example for gears of wind turbines, valve and drive train components, and artificial hip joints to maintain or increase service life time and sustainability. These small wear rates imply a non-linear characteristic of wear, because the amount of wear per load cycle falls below the inter-atomic distances of (technical) materials and consequently can not be a continuous process anymore. Here highly localized effects of dissipated friction energy govern the acting wear mechanisms and alterations of tribosystems, which are still not quantified on the micro- and nano-scale. However today mostly empirically determined wear factors are used to calculate the amount of wear for a given tribological load and hence material failure on those scales can not be predict. This technical matter is complicated by the fact that classical investigations of wear like weighing and micro structural analysis are difficult at the scale and extent of occurring wear appearances within the ultra-mild wear regime. Combined wear tests, micro structural analysis and numerical calculations are presented for the individual analysis of the material response to tribological loads. If a quantification of the failure sequence succeeds on those scales, new design guidelines could be developed, in order to further increase the service life time and predict failure modes more precisely.

Kurzfassung

Tribologische Systeme sind aufgrund von ökologischen und ökonomischen Auflagen einer ständigen Verminderung von Reibung und Verschleiß ausgesetzt. Diese Auflagen können dazu führen, dass die tribologischen Belastungen verändert werden und in einer höheren Belastung der entsprechenden Bauteile enden. Um dennoch weiterhin möglichst kleine Verschleißraten, hin zu ultra-milden Verschleißraten, zu erhalten, ist ein integraler Ansatz erforderlich. Dieser Ansatz muss die Kontaktsituation, die Oberflächentopographie und die oberflächennahen physikalischen Eigenschaften der eingesetzten Materialien beinhalten. Ultra-milde Verschleißraten, in der Größenordnung von wenigen Nanometern pro Stunde, werden für Bauteile wie Getriebe von Windkrafträdern, Ventiltrieben, Antriebsstränge und Hüftimplantaten verlangt, um die Standzeit und Nachhaltigkeit dieser Komponenten weiterhin zu gewährleisten bzw. zu erhöhen. Diese kleinen Verschleißraten bedeuten jedoch einen nicht linearen Fortschritt des Verschleißes, da der Verschleiß pro Lastzyklus unterhalb des atomaren Abstandes von (technischen) Materialien liegt und somit kein kontinuierlicher Prozess sein kann. Hier bestimmen hoch lokalisierte Effekte der einbrachten Reibenergie die Verschleißmechanismen und die Veränderungen der Tribosysteme, die bis heute nicht auf der Mikro- und Nano-Skala quantifiziert wurden. Nichtsdestotrotz werden immer noch empirisch ermittelte Verschleißfaktoren benutzt, um den Verschleiß an Tribosystem für eine gegebene Belastung zu berechnen, die jedoch nicht das Materialversagen detailliert beschreiben oder vorhersagen können. In diesem Zusammenhang kommt erschwerend hinzu, dass die Ermittlung und Bewertung des Verschleißes mittels klassischer Analysemethoden wie Wiegen und Mikrostrukturanalysen aufgrund der Größenordnung des anfallenden Verschleißes erschwert ist. Kombinierte Verschleißtests, Mikrostrukturanalysen und numerische Berechnungen werden hier presentiert, um die individuelle Systemantwort der eingesetzten Materialien auf tribologische Belastungen zu bewerten. Wenn eine Quantifizierung auf diesen Größenordnungen gelänge, könnten neue Design-Richtlinien formuliert werden, um weiter die Standzeit zu erhöhen und Schadensarten genauer vorherzusagen.

Table of Contents

Nomenclature

Roman Symbols

Symbol	
a_H	Hertz'ian contact radius
A_{Aff}	Affected Area
A_c	micro contact area
A_H	Hertz'ian contact area
B	auxiliary variable
d	Damage variable
ds	sliding distance increment
d_s	Separation of reference plane between two rough surfaces
dt	time increment
eFric	specific dissipated friction energy
EFric	dissipated friction energy
D_{ij}^p	auxiliary function
ds	displacement increment
D_{sum}	density of roughness summits
D_{ij}^s	auxiliary function
dt	time increment
E'	equivalent Young's modulus
E_i	Young's modulus, $i = 1, 2$ (base and counter body)
eyr	ellipticity ratio
$\widehat{f}$	auxiliary function
$f_{sampling}$	sampling rate
f_{test}	wear test frequency of reciprocating movement
FoO	Frequency of occurrence
F_N	Normal force
F_R	Friction force
$\overline{G}$	dimensionless material parameter
G	shear modulus
h	gap between contacting surfaces
h_{min}^{CHI}	minimum film thickness of CHI test series
h_{min}^{CS}	minimum film thickness of CS test series
H_{cen}	central film thickness
h_{ini}	initial gap between contact surfaces
h_{min}	minimum film thickness
H_{cen}	dimensionless central film thickness
H_{min}	dimensionless minimum film thickness

H_s	hardness of softer contacting body
I_1, I_2, I_3	Stress invariants
k	wear factor
K	specific wear factor
K^p	influence numbers normal deflection
K^s	influence numbers tangential deflection
M	set of contacting nodes which exceed the yield pressure
N	contacting nodes with $p_{ij} > 0$
N_{Elem}	numbers of elements
n_c	Number of contacting elements
O	auxiliary variable
p	contact pressure
p_{max}	maximal pressure
p_{yield}	mean yield pressure
PF	probability function
P_H	Hertz'ian contact pressure
Q	auxiliary variable
R	Radius
R'	equivalent radius of contacting bodies
R_i	principal radius of contacting bodies, $i = 1, 2$ (base and counter body)
R_a	arithmetic average roughness
R_{asp}	mean radius of asperities
R_{ku}	Kurtosis
R_q	root mean square roughness
R_{sk}	Skewness
R_y'	equivalent radius in sliding direction
R_{yield}	yield strength
s	sliding distance
sdfe	specific dissipated friction energy
sdfp	specific dissipated friction power
SDFP	summed specific dissipated friction power
s_{ij}	elements of deviatoric stress tensor
t	time
T_a	average temperature increase
$T^{p,s}$	contact stress influence numbers
$\overline{U}$	dimensionless speed parameter
u_z	normal deflection
v_{rel}	relative sliding velocity
V_{cell}	Volume of one domain cell

$\overline{W}$	dimensionless load parameter
W	Wear volume
x	x-coordinate, orthogonal to axis of movement
y	y-coordinate, axis of movement
z	z-coordinate, height

Greek Symbols

Symbol	
α	auxiliary variable
α_p	pressure-viscosity parameter
β	auxiliary variable
δ	rigid body movement
Δm	resolution of weighing scale
Δx	lateral resolution
Δy	lateral resolution
Δz	depth resolution
ζ	auxiliary variable
η_0	viscosity
λ	Tallian-parameter
μ	coefficient of friction
ν	Poisson's ratio
ξ	Multiaxiality
σ_{ij}	components of cauchy stress tensor
σ_H	hydrostatic stress
σ_{VM}	von mises stress
σ_T	maximum shear stress
$\sigma_1, \sigma_2, \sigma_3$	principal stresses
σ_{tc}	fatigue limit in fully reversed tension-compression
τ	shear stress
τ_t	fatigue limit in fully reversed torsion
Ψ	plasticity index
Ω	calculation domain

Abbreviations

BB	base body
BL	boundary lubrication
CHI	case-hardened spheroidal cast iron wear test series
CB	counter body
CS	self-mating carburized steel wear test series
dof	degree of freedom
EHL	elastohydrodynamic lubrication
GR	ground
HL	hydrodynamic lubrication
ML	mixed lubrication
M	milled
MF	milled & finished
P	polished

Introduction

Today's economic and ecological directives claim highly sustainable machine parts with increased service life achieved by low production cost and overall energy consumption [1, 2]. Following these requirements it is necessary to reduce friction and wear as an ongoing task. Currently a wide range of processes are used to minimize wear by modifying the near-surface mechanical properties (e.g. by carburizing) and/or applying a hard surface layer [3]. In addition improved materials, renewable bio-lubricants [4], surface texturing methods like dimpling [5] or load optimized geometries [6] are tested. Regarding the tribological performance as an inherent system property the operational tribological stresses can change due to such adjustments. The lubrication regime of gears for example can shift from fully separated (EHL) to the mixed and boundary regime [7]. As a consequence the friction and the wear characteristics change too, as the load is carried more and more by direct asperity contact. In order to further improve the frictional performance and the wear resistance of such systems an integral approach is needed which includes the contact conditions, the surface topography and near-surface mechanical properties. As a defined goal today ultra-mild wear rates of $\leq 10\,nm/h$ should be achieved as suggested for the automotive industries [8]. From this small wear rate it follows that the initially processed surface topography is preserved for a long period of time and can even affect the partition of the wear volume between the stationary base body and moving counter body during running-in, this has a major influence on the entire tribological performance [9–11]. In addition the near-surface materials properties and micro structure have to meet certain criteria to allow for such small wear rates. Namely a nano-crystalline layer should be gained e.g. by tribo-mechanical/chemical reactions, which is reported to have superior wear resistance properties [12]. The prediction of the service life time of a machinery part for maintenance scheduling or guarantee agreements is of great industrial interest. But up to now there is no simple parameter/relationship which can describe the performance of such high wear resistant tribosystem a priori. This is attributed to the complex structure of technical materials [13] (see Figure 1) which can change its characteristics regarding chemical, mechanical, physical and wear properties. Furthermore the multi-scale character of tribocontacts regarding their contact duration and contact size [14] aggravates the analysis. Yet not quantified localized dissipative effects lead to micro structural alterations of the near-surface mechanical properties which can lead to crack initiation (e.g. micro pitting during gear meshing). One of the main problems still remaining today is the question about the mechanical parameter which governs the strength of such small affected volumes. Classical mechanical material parameters determined in uniaxial tensile or dynamic fatigue test are far from being realistic if being compared to the multiaxial character and speed of tribological loads. The local gradients of the contact stresses and the gradients with time are so large that it is far from certain whether macroscopically derived fatigue limits or more generally classical failure theories are valid. Furthermore if ultra-mild wear rates are considered, wear should not be modeled as a continuous process anymore, like it is pronounced in the linear Archard's wear equation [15, 16].

1.1 Tribosystems

The term "tribology" was introduced in 1966 within - *The Jost Report (1966)* ,
"Tribology is the science and technology of interacting surfaces in relative motion and of the practices related thereto." . It includes the study of friction, wear and lubrication. Although the naming of the science of friction, wear and lubrication as tribology was in the late 20th century, the study itself of course is older and can be dated back to ancient times. A list of outstanding tribologist/scientists can be found in [17]. Today a system approach [18] is used to investigate tribological systems in which they are classically divided into four elements.

1. Basebody - stationary
2. Counterbody - relatively moving
3. Interfacial medium - e.g. lubrication fluid such as oil etc.
4. Surrounding medium - e.g. ambient environment

Following this system approach a set of inputs (tribological stresses) and outputs (loss off material and dissipation of energy) can be defined. The tribological stresses summarize the acting normal force F_N, the relative sliding velocity v_{rel}, the type of motion (rolling, sliding etc.), the contact temperature increase $\Delta T_{increase}$, the ambient temperature T_a and the loading time t acting on a small volume compared to the dimensions of the whole contacting bodies. Due to their localized character tribological stresses can exceed the mechanical strength limits and chemical resistance at the interface of the contact and, therefore, lead to the removal of material as an adverse reaction to the applied load. During loading time the surface topography will change its shape and additionally the affected near-surface material changes its microstructure and chemical composition [19–21].

1.2 Wear

The extent and mode of occurring material loss is covered by the umbrella term wear. The mechanical and chemical alteration of the near-surface material is not directly covered by this term, although a strong mutual dependency exists. Wear takes place inevitably by interacting surfaces in relative motion under an applied load. It occurs in different facets and can be classified into four major wear mechanisms (abrasion, adhesion, surface fatigue and tribochemical reactions [22], see Figure 2) and more or less specific definitions of submechanisms. These mechanisms can be identified by their corresponding wear appearances. A clear assignment of the acting wear mechanism must be the basis for the development of countermeasures in technical discussions. The driving force of wear is the dissipation of frictional energy which strongly depends on the materials in contact and the tribological stresses. Wear as well as friction is not a material property, wear must be understood as an inherent

system characteristic of the complete tribosystem. The precise prediction of wear rates is of great interests within the design and service time prediction of tribological loaded machinery parts such as gears, camshafts, roller bearings and train rails. One of the most famous wear models was developed by J.F. Archard [15]. In this wear model he made restrictive assumptions about the wear sequence such that the roughness asperities will deform fully plastically, adhesive wear is prevailing and hemispherical wear particles will occur. Experimentally and theoretically he found a linear relationship which reads:

$$W = k \frac{F_N}{H_s} s = K F_N s \tag{1.1}$$

Where W is the wear volume, s is the sliding distance, k can be understood as a probability factor, F_N is the acting normal force and H_s the hardness of the softer contacting body. The capital $K = \frac{k}{H_s}$ factor is then the wear per unit sliding distance and unit load e.g. the specific wear rate (swr). Despite his restricting assumptions, Archard's model pronounces a linear relationship between wear, the acting normal force and the sliding distance which can be easily measured in wear tests [16] and implemented in calculation software. But the wear equation (Eq. 1.1) does not describe the type of wear, nor can it distinguish between different wear regimes [23]. It calculates the wear volume on the basis of the sliding distance and an experimental measured wear factor *k*. Depending on the tribological stresses, non-linear relationships are reported even by Archard himself. This can be mostly attributed to the influence of the contact temperature elevating at higher relative sliding velocities or changing wear mechanism. In order to further investigate the dependency of wear towards the tribological stresses so called wear maps [24] are commonly used. A wear map for steels is shown in Figure 3. One can see that different kinds of wear regimes are found to be predominant at certain operational conditions. The lowest wear regime e.g. the ultra-mild wear regime is set to a wear rate of $K \leq 10^{-9} \left[\frac{mm^3}{mm\,N}\right]$ under steady-state conditions (bottom left in Fig. 3). All that and the great variety of tribosystems and material combinations underline the complexity of wear as a highly non-linear process. Considering technically relevant wear rates this model concept of wear reaches its limits. In fact the wear equation 1.1 can be used to model the amount of wear after a given set of tribological loads, but it can not predict the alterations of the micro structure and, therefore, can not predict transitions of the wear characteristics in time.

1.3 Tribosystems with ultra low wear rates

Considering technical capital goods (e.g. power plants, trucks, airplanes etc.) the service life time should be as high as possible in order to obtain highest possible returns and minimize maintenance costs. Tribosystems involved in these goods (gears, bearings, engines) are strongly connected to the overall service life time due to wear and the loss of functionality if wear exceeds a critical level. If the tribological loads and the geometry of the contacting bodies should not be modified, the material properties, the surface finish of the contacting bodies and the lubrication provide potential

for optimization. In order to obtain the smallest possible wear rates essentially there are four options: to change the material (higher strength, tougher, high corrosion resistance etc.), to manipulate the material properties by mechanical & thermo-mechanical treatment, surface hardening or by applying a hard layer onto the contact interfaces [25], to change the surface finish in order to generate optimized contacts and finally to change the lubricant. Beyond wear considerations all these countermeasures must be considered regarding productions costs, machinability and the functionality of the tribosystem.

Tribologically induced near-surface material alterations

The energy dissipation in tribologically loaded contacts can be divided into heat, wear and significant changes of the near-surface material [12]. Plastic deformations and microstructural alterations within the very early stages of the workload, often denoted as running-in or break in of the tribosystem, can precursor processes like material transfer, mechanical mixing, chemical alterations and fracture of the near-surface material [20, 21]. On this account the analysis of the near-surface alteration plays an important role in the understanding of friction energy or power driven processes of wear. Considering tribosystems with low wear rates the tribologically induced alteration of the near-surface material generates a nanocrystalline layer. This nanocrystalline layer has a typical thickness of 10 nm up to several hundred nanometers [26]. These nanocrystalline layers are held responsible for the superior wear resistance of such systems, which can be discussed in two ways [12]: The nanocrystalline layer is extremely hard and therefore protects the surface from plastic yielding within the highly loaded micro-contacts. A second explanation could be that these layers are superplastic and soft and can act as a lubricant and protect the contact by a highly shearable layer. Still, the wear protective mechanism and sequences of layer generation are still subject of current scientific investigations.

1.4 Rough Surfaces

All real surfaces are rough [27]. Even mirror shine polished surfaces deviate from atomic flatness on the nm-scale (Fig. (4)). Moreover surfaces deviate from the geometric ideal on the μm-scale due to production tolerances and manufacturing strategies. Surface finish is an important link between the manufacturing process and the functionality expected of the surface. This relationship between surface finish, part functionality, and manufacturing process parameters is the primary reason for the measurement, characterization, and study of surface texture. Due to decreasing wear rates the machined surface topography remains intact for a longer period of time during tribological loading, so that it becomes more and more important already in the design of tribological loaded machinery parts [28]. The surface topography is commonly described with a set of statistical roughness parameters, which are used in engineering drawings in order to communicate the surface characteristics from the design to the manufacturing division. The advantage of these statistical parameters is the reduction of surface height into a manageable set of parameters, the disadvantage is generally the loss of information. The

original surface topography cannot be reconstructed from known statistical parameters. The arithmetic average roughness, Ra, is defined as:

$$R_a = \frac{1}{N_{Elem}} \sum_{i=1}^{N} |z(i)| \tag{1.2}$$

Where z is a set of surface height data points and N_{Elem} the total number of data points. The root mean square roughness, Rq, is defined as:

$$R_q = \sqrt{\frac{1}{N_{Elem}} \sum_{i=1}^{N} z(i)^2} \tag{1.3}$$

The skewness is a measure of the asymmetry of the profile and is defined as

$$R_{sk} = \frac{1}{N_{Elem} R_q^3} \sum_{i=1}^{N} z(i)^3 \tag{1.4}$$

and kurtosis is a measure of the spikiness of the profile.

$$R_{ku} = \frac{1}{N_{Elem} R_q^4} \sum_{i=1}^{N} z(i)^4 \tag{1.5}$$

1.5 Contact mechanics

Heinrich Hertz developed fundamental equations to calculate the contact pressure and contact area of (non-)conformal contacting bodies back in 1881 [29]. His basic assumptions were that the contacting bodies are fully elastic, smooth, the contact area is much smaller than the overall geometry of the contacting bodies and the contact is frictionless.
In the case of a sphere with a constant radius R_1 in contact with a plane $R_2 = \infty$ the Hertz'ian contact radius a_H and contact area A_H are calculated by

$$a_H = \left(\frac{3\, F_N\, R'}{4\, E'} \right)^{\frac{1}{3}} \tag{1.6}$$

$$A_H = \pi a_H^2 \tag{1.7}$$

F_N: Normal force acting on the contacting bodies

R': Equivalent contact radius $R' = \left(\frac{1}{R_1} + \frac{1}{R_2} \right)^{-1}$

E': Equivalent Young's modulus $E' = \left(\frac{1-\nu_1^2}{E_1} + \frac{1-\nu_2^2}{E_2} \right)^{-1}$

The maximum contact pressure P_H can be calculated by:

$$P_H = \frac{3}{2}\frac{F_N}{\pi a_H^2} \tag{1.8}$$

Statistical rough contact model

The real contact area between two contacting bodies under an applied load is only a small portion of the apparent or geometric contact area according to Hertz due to the fact that all technical surfaces are rough on the micro-scale. Roughness asperities which are closely correlated to the final production step will cause the initial contact [27] at the highest matching points. With an increasing load one expects an increasing micro contact area and an increasing number of contact spots. If the contact pressures exceed the material strength plastic deformation will occur. Thus the analysis of the real contact area regarding the micro contact area size and hence the acting contact pressure is very important in tribological design and analysis, as it is the origin of friction and wear. One of the first micro contact models is the micro contact model according to Greenwood & Williamson [27]. Within this model the roughness asperities are treated as hemispherical caps having a constant radius R_{asp}, their surface height z follows a Gaussian distribution $\phi(z)$ and any interaction between deformed roughness asperities is neglected. This model enables to analyze the micro contact with statistical methods and allows for the calculation of the number of micro contacts n_c and the micro contact area A_c. If the two surfaces are separated by a distance d, the probability of making contact (z > d) can be calculated by:

$$PF(z > d_s) = \int_{d_s}^{\infty} \phi(z)\,\mathrm{d}z \tag{1.9}$$

The expected number of micro contacts within the nominal contact area given by the Hertzian solution (Eq. 1.7) is then:

$$n_c = D_{sum}\, A_H \int_{d_s}^{\infty} \phi(z)\,\mathrm{d}z \tag{1.10}$$

Where D_{sum} is the density of roughness summits within a unit area. The micro contact area is calculated by:

$$A_c = \pi\, D_{sum}\, A_H\, R_{asp} \int_{d_s}^{\infty} (z - d_s)\,\phi(z)\,\mathrm{d}z \tag{1.11}$$

Where R_{asp} is the mean radius of the roughness asperities. Another very useful parameter is the plasticity-index Ψ [27]. It can indicate whether predominantly elastic ($\Psi < 0.6$) or predominantly plastic deformation ($\Psi > 1.0$) characteristics of surface topographies prevail, which is defined as.

$$\Psi = \frac{E'}{H_s}\sqrt{\frac{\sigma_s}{R_{asp}}} \tag{1.12}$$

E': Equivalent Young's Modulus

H_{soft}: Hardness of softer contact body

σ: Standard deviation of height distribution

R_{asp}: Mean radius of asperities

The advantages of this model are the quick calculative results, the disadvantage of this model is that the actual distribution of the micro contacts and thus the local tribological load is lost within the statistical analysis [30].

Semi analytically rough contact modeling

If the dimensions of the contact area are small compared to the radii of curvature of the contacting bodies, both contacting bodies can be considered as half-spaces. The half-space concept is well established for the calculation of rough contacts [31–35], and is capable of considering 3D rough and technically relevant surface characteristics. Furthermore, Fast Fourier Transform (FFT) techniques further reduce the time to solve rough contact problems in acceptable computational times, even on a personal office computer. Within such a contact formulation the contacting rough surfaces are described by two sets of surface height data sets with a uniformly spaced rectangular grid of surface points. Such surface topography data sets can be obtained e.g. by using a 3D surface scanning device or generated artificially by a computer [36]. The two surface grids are assumed to have the same spacings and numbers of elements in both directions. It is assumed that reference planes of two contacting surfaces become parallel and their grid nodes match in order to use a single grid to calculate the normal deflection and the contact pressure, according to

$$h(x,y) = u^z(x,y) + h^{ini}(x,y) - \delta \geq 0 \tag{1.13}$$

Here h is the resulting gap between the two contacting surfaces, u^z the surface deflection, h^{ini} the initial gap and δ the ridig body movement. The pressure distribution is always greater or equal 0 either outside or inside of the contact area Ω and can be limited to a maximum allowed pressure p_{max}

$$p(x,y) \geq 0 \wedge p(x,y) \leq p_{max} \tag{1.14}$$

$$p(x,y) = 0 \not\subset \Omega \tag{1.15}$$

with a vanishing gap between both surfaces inside the contact area.

$$h(x,y) = 0 \subset \Omega \tag{1.16}$$

The deflection is calculated by convolution of the pressure distribution and influence numbers for the normal K^p and tangential K^s deflection.

$$u^z(x,y) = \int_\Omega K^p(x-x', y-y')p(x',y')d\Omega + \int_\Omega K^s(x-x', y-y')\,\mu\, p(x',y')d\Omega \tag{1.17}$$

$$K^p(x,y) = \frac{1-\nu^2}{\pi E} \int \frac{1}{\sqrt{(x-x')^2+(y-y')^2}} \tag{1.18}$$

$$K^s(x,y) = \frac{1}{\pi G} \int \frac{x-x'}{(x-x')^2+(y-y')^2} \tag{1.19}$$

The formulation of the normal influence numbers reads:

$$K^p(x,y) = \frac{1-\nu^2}{\pi E}\left[\widehat{f}(x_o,y_o) + \widehat{f}(x_u,y_u) - \widehat{f}(x_o,y_u) - \widehat{f}(x_u,y_o)\right] \tag{1.20}$$

$$\widehat{f}(x,y) = x \cdot ln(y + sqrt(x^2+y^2)) + y \cdot ln(x + sqrt(x^2+y^2)) \tag{1.21}$$

The formulation of the tangential influence numbers reads:

$$K^s(x,y) = \frac{1}{\pi G}\left[\widehat{g}(x_o,y_o) + \widehat{g}(x_u,y_u) - \widehat{g}(x_o,y_u) - \widehat{g}(x_u,y_o)\right] \tag{1.22}$$

$$\widehat{g}(x,y) = \frac{y}{2} ln(x^2+y^2) - y + x \cdot tan^-1(\frac{y}{x}) \tag{1.23}$$

Always assuming a constant pressure and deflection over a rectangular grid.

$$\begin{aligned} x_o &= x + \Delta x \quad y_o = y + \Delta y \\ x_u &= x - \Delta x \quad y_u = y - \Delta y \end{aligned} \tag{1.24}$$

1.5.1 Subsurface contact stress distribution

The knowledge of the sub-surface contact stress distribution is critical to the design of a tribological element. The stress fields can be expressed as:

$$\sigma(x,y,z) = \int\int p(x',y')T^p(x-x', y-y', z) + \mu\, p(x',y')T^s(x-x', y-y', z)dx'dy' \tag{1.25}$$

The calculation of the contact stresses stresses according to Eq. 1.25 can be carried out by influence numbers for the normal T^p and tangential load T^s and previously mentioned discrete convolution technique (DC-FFT algorithm). These influence numbers can be found in [37].

$$T^{p,s}_{kl}(x,y,z) = \frac{1}{2\pi}\left[D^{p,s}_{kl}(x_o,y_o,z) + D^{p,s}_{kl}(x_u,y_u,z) - D^{p,s}_{kl}(x_u,y_o,z) - D^{p,s}_{kl}(x_o,y_u,z)\right] \tag{1.26}$$

where k and l represent the cartesian components of the general stress tensor.

$$\begin{aligned} x_o &= x + \Delta x \quad y_o = y + \Delta y \\ x_u &= x - \Delta x \quad y_u = y - \Delta y \end{aligned} \tag{1.24}$$

The normal components are calculated by the following equations:

$$D^p_{xx}(x,y,z) = -2v\ \tan^{-1}\left(\frac{xy}{Rz}\right) + 2(1-2v)\ \tan^{-1}\frac{x}{(R+y+z)} - \frac{xz}{R(R+y)} \tag{1.27}$$

$$D^p_{yy}(x,y,z) = D^p_{xx}(y,x,z) \tag{1.28}$$

$$D^p_{zz}(x,y,z) = -\tan^{-1}\frac{xy}{(Rz)} + \left(\frac{xz}{R(R+y)}\right) + \frac{yz}{R(R+x)} \tag{1.29}$$

$$D^p_{xy}(x,y,z) = -(1-2v)ln(z+R) - \frac{z}{R} \tag{1.30}$$

$$D^p_{xz}(x,y,z) = -\frac{z^2}{R(R+y)} \tag{1.31}$$

$$D^p_{yz}(x,y,z) = -\frac{z^2}{R(R+x)} \tag{1.32}$$

$$R = \sqrt{x^2+y^2+z^2} \tag{1.33}$$

The shear components are calculated by the following equations:

$$D^s_{xx}(x,y,z) = 2ln(y+R) + z(1-2v)\left(\frac{y}{R(R+z)} + \frac{z}{R(R+y)}\right) - 2v\frac{x^2}{R(R+y)} \tag{1.34}$$

$$D^s_{yy}(x,y,z) = 2ln(y+R) + z(1-2v)\left(\frac{y}{R(R+z)}\right) - 2v\frac{y}{R} \tag{1.35}$$

$$D^s_{zz}(x,y,z) = -\frac{z^2}{R(R+y)} \tag{1.36}$$

$$D^s_{xy}(x,y,z) = ln(x+R) - z(1-2v)\frac{x}{R(R+z)} - 2v\frac{x}{R} \tag{1.37}$$

$$D^s_{xz}(x,y,z) = -\frac{xz}{R(R+y)} - tan^{-1}\frac{xy}{Rz} \tag{1.38}$$

$$D^s_{yz}(x,y,z) = -\frac{z}{R} \tag{1.39}$$

Again:

$$R = \sqrt{x^2+y^2+z^2} \tag{1.33}$$

These explicit equation can be used to calculate the contact stresses of 3D and/or 2D contacts and coincide well with other results which can be found in the literature [38].

1.5.2 Multiaxial stresses and fatigue limit

Tribological stresses in sliding of (non)-conformal contacts as well as realistic stresses in machinery parts during operation are generally multiaxial.

$$\sigma_{ij} = \begin{bmatrix} \sigma_{xx} & \sigma_{xy} & \sigma_{xz} \\ \sigma_{yx} & \sigma_{yy} & \sigma_{yz} \\ \sigma_{zx} & \sigma_{zy} & \sigma_{zz} \end{bmatrix} \tag{1.40}$$

Any state of stress (Eq. 1.40) can be decomposed into a hydrostatic σ_H and a deviatoric stress s_{ij}.

$$\sigma_{ij} = \sigma_H + s_{ij} \tag{1.41}$$

The hydrostatic stress tensor reads:

$$\sigma_H = \frac{\sigma_{xx} + \sigma_{yy} + \sigma_{zz}}{3} \tag{1.42}$$

The deviatoric stress tensor reads:

$$s_{ij} = \begin{bmatrix} \sigma_{xx} - \sigma_H & \sigma_{xy} & \sigma_{xz} \\ \sigma_{yx} & \sigma_{yy} - \sigma_H & \sigma_{yz} \\ \sigma_{zx} & \sigma_{zy} & \sigma_{zz} - \sigma_H \end{bmatrix} \tag{1.43}$$

The hydrostatic stress is responsible for volume changes, the deviatoric stress for changing the shape.

Yield criterion

The von Mises criterion [39] (critical distortional energy) and the Tresca criterion [40] (critical shear stress) reduce the general stress state (Eq. 1.40) to a scalar value to predict the onset of yielding of a material under complex loading conditions. This scalar can be compared with the yield strength from simple uniaxial tensile tests. The von Mises stress satisfies the condition that two stress states with equal distortion energy have equal von Mises stress. In terms of principal stresses the von Mises criterion reads:

$$\sigma_{VM} = \sqrt{\frac{1}{2}\left[(\sigma_1 - \sigma_2)^2 + (\sigma_2 - \sigma_3)^2 + (\sigma_3 - \sigma_1)^2\right]} \leq R_{yield} \tag{1.44}$$

The Tresca criterion reads:

$$\sigma_T = max\left(|\sigma_1 - \sigma_2|, |\sigma_2 - \sigma_3|, |\sigma_3 - \sigma_1|\right) \leq R_{yield} \tag{1.45}$$

The principal stresses are the components of the stress tensor (Eq. 1.40) when the basis is changed in such a way that the shear stress components become zero. In these yielding criterions there is no distinction between hydrostatic tensile or compression stress fields, which can have a significant influence on the ductility and thus on the fatigue limit of technical materials [41]. Furthermore the onset of yielding must not necessarily coincide with failure.

Fatigue limits

However, on the mesoscale stresses and strains are responsible for fatigue type of failure of technical materials due to crack initiation and propagation. By the definition of engineering stress, stresses and strains are uniformly distributed over the specimen cross section in uniaxial tensile/compression test, which generally holds not true on the mesoscale [42, 43]. Stresses and strains on the mesoscale will depend on the distribution of grain size and orientation. Moreover in a more sophisticated approach to fracture and associated failure limits the influence of the mean or hydrostatic stress part of the acting stress cannot be neglected. The multi-axiality ξ as a fraction of the hydrostatic stress and the von Mises stress is introduced as follows [41].

$$\xi = \frac{\sigma_H}{\sigma_{VM}} \tag{1.46}$$

In terms of multiaxial fatigue criterion the fatigue limit of metals depends on the hydrostatic stress σ_H and decreases with positive (tensile) hydrostatic stress states [42]. This fatigue criterion reads.

$$Max_t \left[\tau(t) + \alpha\sigma_H(t)\right] \leq \beta \tag{1.47}$$

In Eq.1.47 $\tau(t)$ is the local or mesoscopic maximum shear stress, α and β are material parameters which can be evaluated from reversing tensile and bending or torsion fatigue tests. From Eq. 1.47 one can define a quantity d which quantifies the danger of failure:

$$d = Max_t \left[\frac{\tau(t)}{\beta - \alpha\sigma_H(t)}\right] \tag{1.48}$$

For a general fatigue analysis of machinery parts a maximum of d is sought over characteristic loading times, in tribological contacts the quantity d has to be calculated in each time instance. The variables α and β are defined as follows:

$$\alpha = 3\left(\frac{\tau_t}{\sigma_{tc}} - \frac{1}{2}\right) \tag{1.49}$$

$$\beta = \tau_t \tag{1.50}$$

where τ_t is the fatigue limit in fully reversed torsion and σ_{tc} the fatigue limit in fully reversed tension-compression test.

1.6 Dissipated frictional energy and frictional power; wear criterion

Under laboratory conditions excluding all external energy inputs, the frictional energy is responsible for all possible chemical-physical alterations of the near-surface material including frictional heating, sound emission, chemical reactions on top of the surface and the generation of wear. The measurement and even more so the precise prediction of all these dissipative mechanisms is still not possible due to the inaccessibleness of the tribological contact and the lack of general understanding of the interaction of all those dissipative mechanisms taking place. Macroscopically the frictional energy can be measured indirectly by wear tests, as it is the scalar product of the acting frictional force and the corresponding sliding distance as an integral value. This integral value corresponds to an average value of the whole contact area:

$$E_{Fric}(t) = F_R(t)\, ds(t) \tag{1.51}$$

The frictional dissipated energy is often used to correlate the overall performance of tribocontacts regarding wear and wear transitions [11, 44, 45] as it can be related to the occurring wear volume and thus allows for friction energy related wear considerations. Furthermore this macroscopic approach can be extended to the microscopic scale by locally solving the rough contact problem in the boundary lubrication regime. The specific dissipated friction energy (*sdfe*) then becomes.

$$e_{Fric}(x, y, t) = sdfe(x, y, t) = \mu(t)\, p(x, y, t)\, ds(t) \tag{1.52}$$

The specific dissipated frictional power (*sdfp*) can be calculated from known coefficient of friction, pressure distribution and relative sliding velocity.

$$sdfp(x, y, t) = \frac{sdfe(x, y, t)}{dt} = \mu\, p(x, y, t)\, v_{rel}(t) \tag{1.53}$$

1.7 Lubrication

Depending on the operating conditions different types of lubricants are used to significantly reduce friction and wear. The lubricant can be a liquid, solid, grease or gas [46]. The Stribeck curve [47] is often used to obtain the characteristics of liquid lubricants and identifies different lubrication and friction regimes with increasing lubrication film thickness or increasing Hersey number $\frac{\eta\omega}{p}$. These different regimes are the boundary lubrication regime (**BL**), the mixed lubrication regime (**ML**), elastohydrodynamic lubrication regime (**EHL**) and the hydrodynamic lubrication regime (**HL**). As can be seen from Figure 5 the EHL regime occurs in non-conformal contacts. Here the elastic deformation of the load carrying surfaces becomes significant. In order to incorporate the surface roughness into the lubrication regime approach the Tallian parameter [48] can be calculated which allows for

differentiating the various lubrication regimes by a simple scalar value λ:

$$\lambda = \frac{h_{min}}{\sqrt{R_{q,1}^2 + R_{q,2}^2}} \tag{1.54}$$

where h_{min} is the minimum lubrication film thickness and $R_{q,1}$ and $R_{q,2}$ are the root mean square roughness of the contacting bodies. A Tallian parameter of $\lambda < 1$ represents the BL, $1 <= \lambda < 3$ represents the ML and $\lambda >= 3$ the EHL or HL lubrication regime.

Dimensional Analysis

The minimum film thickness is generally calculated from the Reynolds equation [49] derived from the Navier-Stokes equation for the pressure distribution in a narrow and converging gap between two bearing surfaces. The first fully numerical results of the calculated film thickness and corresponding pressure distribution were shown in [50]. In this publication a first fitted function of the type $h_{min} \propto W, U, G$ was stated. Considering non-conformal contacts and materials of high elastic modulus, the equations 1.55 and 1.56 can be used to approximate the minimum and central lubrication film thickness [46]:

$$H_{min} = 3.63\, \overline{U}^{0.68}\, \overline{G}^{0.49}\, \overline{W}^{-0.073}(1 - ^{-0.68\, eyr}) \tag{1.55}$$

$$H_{cen} = 2.69\, \overline{U}^{0.67}\, \overline{G}^{0.53}\, \overline{W}^{-0.067}(1 - 0.61e^{-0.73\, eyr}) \tag{1.56}$$

H_{min}: dimensionless minimum film thickness $\frac{h_{min}}{R'_y}$

H_{cen}: dimensionless central film thickness $\frac{h_{cen}}{R'_y}$

R'_y: equivalent contact radius in the direction of sliding $R'_y = \left(\frac{1}{R_{y,1}} + \frac{1}{R_{y,2}}\right)^{-1}$

$\overline{U}$: dimensionless speed parameter $\frac{\eta_0\, v_{rel}}{E'\, R'_y}$

η_0: dynamic viscosity at test temperature

$\overline{G}$: dimensionless material parameter $G = \alpha_p E'$

E': equivalent elastic constant $E' = \left(\frac{1-\nu_1^2}{E_1} + \frac{1-\nu_2^2}{E_2}\right)^{-1}$

α_p : viscosity-pressure coefficient

$\overline{W}$: dimensionless load parameter $\frac{F_N}{(E'\, R_y'^2)}$

eyr: ellipticity ratio; eyr = 1 (ball-on-plane contact)

Boundary lubrication

Boundary lubrication [51] gains more and more interest in recent times [52]. The reason for increasing scientific activities can be found in the general trend of thinning lubrication films (Table 6.1) in tribological contacts [53] and film breakdowns during start and stop sequences for maintenance of machinery due to low relative sliding speeds. The boundary lubrication regime therefore usually occurs at high loads and low speed conditions and governs the service life time of machinery components. Within the boundary lubrication regime the average film thickness is less than the composite surface roughness (see Eq. 1.54) and it is generally accepted that the contact load is mostly carried by the roughness asperities. Thus chemical reaction products within the interface of the contacting surfaces and the chemical reaction kinetics play an important role in the reduction of wear and depend on the tribological loads and environmental conditions. The dissipation of energy and the reactive surfaces of the contact are the breeding grounds of boundary lubrication film formation. Chemical reaction involved in this process are oxidation of the surfaces, lubricant oxidation and degradation, surface catalysis, polymerization and organometallic chemistry [54]. Basic and important film formation mechanism are descripted in [46]. Here these are identified as physisorption, chemisorption, chemical reactions and chemical reactions involving the substrate. In order to gain wear protective layer the design of the chemical reactions should aim at strong load-carrying reaction products deposited on the contacting surfaces. Ideally the removal rate should be lower than the growth rate to obtain an self-generating boundary film. Today the growth of such a boundary layer is either modeled by mechanical and thermal activation [55], or as a diffusion driven process [56].

1.8 Aim of this work

The calculation of the wear volume by a linear correlation between the wear volume and the sliding distance works well, if the wear factor or wear rate is experimentally known and the wear mechanism do not change in time. The wear rates of modern tribosystems are steadily decreasing and the concept of wear as a linear and continuous process reaches its limits. In order to further improve the performance of already high wear resistant tribosystems future wear models should incorporate potential tribolayer formation and near- & subsurface microstructural alterations. In this regard it necessary to consider the tribological loads on top of the contacting surfaces and stresses underneath the contact locally. On the one hand this approach might lead to revised tribolayer formation (mechanical mixing and near-surface chemical-alteration) and micro contact fatigue models, on the other hand this also implies tremendous laboratory work in order to validate those new models. Nevertheless a first step in this direction could be done by the calculation of the specific dissipated friction power on top of the contacting surfaces and of the critically affected volume underneath the contact by multiaxial fatigue models.
On that account the aim of this work is divided into two parts. Within the first part reciprocating sliding wear tests are conducted with high wear resistant tribosystems under boundary lubrication. A variation

of the contacting material and surface topography is utilized to generate different types of tribosystems and initial contact conditions. The tribological performances are characterized by classical wear analysis methods. In the second part of this work micro contact and multiaxial fatigue models are implemented to calculate the sdfp and the critically affected volume in regard to the conducted wear tests over one half cycle of the reciprocating wear test movement which represents a characteristic length scale of the wear test. Therefore measured wear test data and surface topography measurements serve as an input to the conducted contact simulation. In a postprocessing step the sdfp and the critical affected volume are presented to reveal the evolution of the tribological performance with wear test time.

Material and Methods

Two reciprocating sliding wear test series were carried out on a custom built tribometer. A schematic representation of the test rig can be seen in Figure 6 together with the definition of the coordinate system used in this work. Within the test series two different material combinations consisting of a self-mating **c**arburized **s**teel 18CrNiMo7-6 (ISO 1.6587) (referred to as CS wear tests) and a 52100 steel against a **c**ase-**h**ardened spheroidal cast **i**ron EN-GJS-HB 265 (referred to as CHI wear tests) were subjected to the same nominal tribological load (Tab. 6.2). The lubrication was differently provided by a gear oil (Mobilgear, SHC XMP 320, $\eta_0 = 335\ \frac{mm^2}{s}$) at 22°C for the CS test series and by an engine oil (Mobile 1^{TM} ESP Formula 5W-30, $\eta_0 = 72.8\ \frac{mm^2}{s}$) for the CHI test series at 80°C.

18CrNiMo7-6 (1.6587)

The carburized martensitic steel 18CrNiMo7-6 (1.6587) can develop a hard wear resistant case up to 750 HV10 and a tough core with a tensile strength up to 1300 MPa. It has good through hardening properties with a high toughness due to the low carbon and relatively high content of alloying elements. Typical applications are bearings and gears. Due to the high tensile strength it can be used uncarburized but through hardened and tempered as well. A cross section after carburizing is shown in Figure 7, the chemical composition of the alloy in Table 6.3. The physical properties are listed in Table 6.4.

EN-GJS-HB 265 (EN-JS 2070)

The physical properties of spheroidal cast iron, better known as ductile cast iron, are determined by the micro structure being either ferritic or perlitic. Especially perlitic types of microstructure are suitable for tribologically stressed machinery parts. Lowering the internal notch effects of the graphite nodules within the metal matrix leads to competitive mechanical properties and ductility compared to steels. The better castability compared to cast steel makes spheroidal cast irons a noteworthy alternative for the design of engines, turbines and pumps. Additionally, ductile cast iron is suitable for case-hardening techniques to generate hard surface layer. Typically EN-GJS-HB 265 has a tensile strength of 700 MPa and a hardness of about 320 HV10 (unhardened), after case-hardening a hardness of about 550-650 HV10 can be achieved. A cross section after flame hardening is shown in Figure 8, the chemical composition in Table 6.5. The physical properties are listed in Table 6.6.

52100 steel (100Cr6, 1.3505)

The bearing steel 52100 (100Cr6) is typically used for bearings and highly stresses machinery components like injection systems in the automobile industry. As delivered, the hardness ranges between 210 - 400 HV10. Hardened, it can achieve a hardness of about 700 HV10. The tensile strength can reach up to 1370 MPa. Within the wear test series bearing balls according *DIN 5401 / ISO 3290* with a radius of

5 mm were used. The chemical composition is shown in Table 6.7. The physical properties are listed in Table 6.8.

2.1 Sample preparation

Four different machining strategies were applied to machine the samples used within the wear test series. The same machining parameters were used for the 18CrNiMo7-6 and the EN-GJS-HB 265 samples [57]. As a result, four different surface topographies were available for both base body materials, namely a milled, a ground, a milled & finished and a polished one. Milling was done by a Deckel Maho DMU 50 eVolution machine (Seebach, Germany), grinding by a Geibel & Hotz FS 635-Z CNC (Homberg, Germany) and finishing by a Supfina 202 (Grieshaber GmbH & Co. KG, Wolfach, Germany). The polished surfaces were prepared by standard metallographic methods using diamond suspension with a particle size up to 1 μm. Surface line profiles of the machined 18CrNiMo7-6 bodies are shown in Figure 9, the machined EN-GJS-HB 265 base bodies are shown in Figure 10. All profiles were measured parallel to the direction of wear test sliding. The root mean square roughness R_q values are listed in Table 6.9.

2.2 Wear test

All tests were carried out as ball-on-plane reciprocating sliding wear tests at a frequency of f_{Test} = 5 Hz with a stroke of $s_{Test} = 6\,mm$ and under a normal force of F_N = 30 N. The radius of the hemispherical counter body is 5 mm; the machined body is cuboid with 10 x 10 x 15 mm^3 (height x width x depth). Care has been taken to ensure that the hardened layer remained after sample preparation. The normal contact force F_N, the friction force in sliding direction F_{RY} and orthogonal to that F_{RX} are measured in-situ with a 3-axis dynamometer (Type 9257A, Kistler Instrumente AG, Winterthur, Switzerland) every 200 cycles with a sampling rate of $f_{sampling}$ = 2048 Hz over a period of three cycles. In this study only F_{RY} is considered and is further mentioned as F_R. In order to record the movement of the counter body the desired and actual displacement as well as the testing time was recorded, too. Figure 11 shows typical sensor data recorded over one half cycle of the reciprocating sliding wear test. The relative sliding velocity was calculated from the actual displacement signal by first order central difference approximation. After a predefined number of test-cycles (50K, 75K, 150K, 300K, 600K, 1.2M and 2.0M) the worn surfaces were examined. Special attention was paid to the remounting of the specimens after examination to avoid or at least minimize the recurrence of running-in effects. Before the specimens were analysed, all specimens were ultrasonically cleaned in ethanol for about 1 min. Two indentation marks on the base body and an engreaved mark on the counter body were used to define the exact position and orientation for topography analysis. The scanning process was done by means of confocal white light microscopy (CWLM, µSurf, Nanofocus, Oberhausen, Germany), with a lateral resolution of $\Delta x = \Delta y = 1.5656$ µm and a spatial resolution of $\Delta z \approx 4nm$. Obtained surface height

data were filtered with a software high pass and low pass Gaussian filter with cut-off-wavelengths of $\lambda_{CH} = 15$ µm and $\lambda_{CL} = 800$ µm, respectively. The high pass filter operation is used to avoid high first and second derivatives of the surface height data, the low pass filter to remove the waviness.

2.2.1 Wear volume calculation

Due to the very small amount of occurring wear in the ultra-mild sliding wear regime the measurement of the wear mass of the contacting bodies is generally aggravated. Therefore the surface subtraction is a preferred method, which depends on precise measurements of the surface topography, and in the case of non-smooth e.g. milled surfaces, on the repeatable alignment of the sample in order to superimpose different measurements. Modern confocal white light microscopy systems allow for large surface topography measurements in reasonable time, an example for a measurement of the milled 18CrNiMo7-6 base body is shown in Figure 12. This topography data set is sufficient to capture the complete wear track on the base body, which is done by stitching of single and individual measurements. During stitching the measurements are compared and overlapped at adjacent borders by height correlation. The exact same alignment of a sample before and after wear tests cannot be fulfilled on the µm -scale without special alignment devices. Small deviations of the alignment of specimen are likely to occur and may be composed from translational and rotational misalignment. Regarding the base body three degrees of freedom are most important. If one assume a plane table combined with the assumption that the overall shape of the sample is not distorted during wear tests, the misalignment consists of to 2 translatoric degrees of freedom (*dof*) and 1 rotational dof. In order to handle the misalignment hardness indentation marks (bottom right (master mark) and upper left corner (slave mark) in Fig. 13) were applied and serve as fix points. The center of the master marks in two measurements were shifted translatorically to be aligned, the slave marks were shifted by rotation around the z-axis until a minimum difference between both slave marks was reached. The calculation of the wear volume of the spherical counter body is possible by the shape which was handled by 2D surface fits of the unworn counter body.

2.2.2 Analysis of wear appearances

The analysis and documentation of the wear appearances after the wear tests were done by means of scanning electron microscopy (Gemini 1530, Leo, Oberkochen, Germany). This technique is very suitable for conductive materials which were exclusively used in this study. It is a scanning technique which makes use of a focused electron beam (0.5 - 10 nm) under high vacuum. Different imaging modes utilize physical interactions of the electron beam with the near-surface material to typically generate grey scale images. The brightness is correlated to the number of detected electrons. The SE mode for example uses secondary electrons which are highly suited to render surface topographical information. The secondary electrons are emitted from the k-shells of the illuminated atoms of the sample due to inelastic scattering. Thus the SE mode was used exclusively in this study. Additionally

macroscopic images were taken by a reflected-light microscope (BX41TF, Olympus Optical Co. Ltd., Tokyo, Japan).

2.3 Lubrication regime calculation

The lubrication regime is calculated by Eq. 1.54 and 1.55. The corresponding surface roughness was extracted from surface topography measurements within the wear track in the direction of sliding within the wear tests. The dynamic viscosity and the pressure-viscosity coefficient used in this calculation are tabulated in Tab. 6.10.

2.4 Contact calculation

The precise contact calculation regarding the contact pressure and contact area on the microscopic scale is a discipline of its own. Generally, 3D methods are needed to accurately calculate the contact conditions in order to design tribological contacts regarding wear and frictional performance. Modern surface topography measurement devices can scan large surface areas with high resolution. Calculating the pressure distribution of rough contacts generally involves the solution of large systems of equations and therefore advanced computational strategies are needed in order to gain the results within affordable computational times. A. Brandt and A.A. Lubrecht proposed a multi-level multi summation technique [34] back in 1990, which made the numerical contact calculation feasible as they reduced the computational time by orders of magnitude compared to older solver strategies. Modern contact algorithm take advantage of iterative solver (conjugated gradient method) and a discrete cyclic convolution method (DC-FFT) proposed in [35]. In order to solve the rough contact the tribological loads (normal force F_N and the acting coefficient of friction μ), the micro geometries of the contacting bodies as a data set of surface heights and the material parameters (Young's Modulus $E_{(1,2)}$ and the elastic Possion's ratio $\nu_{(1,2)}$; [1]) must be known. The tribological loads were measured in the conducted wear tests and served as an input to the contact simulation. In order to calculate the relative movement of the counter body, the actual displacement was used to apply simple kinematic rules (Figure 14). In order to map the displacement increment onto the surface topography data, the displacement increment was divided by the lateral resolution of the surface topography measurement in the direction of sliding. On this account every data point corresponds to a specific time instance of the reciprocation wear test movement and the rough contact is solved with an updated set of tribological loads and surface topographies.

[1] (1) moving counter body, (2) stationary base body

2.4.1 Contact pressure

In order to solve the contact problem the following calculation steps are implemented in MATLAB®. Within the contact solver, the nodal pressure is limited by an upper value p_{max}, as proposed by [58]. A domain Ω, which is expected to include the contact area is chosen. In this domain, contact geometry should be known either from artificially computer generated geometries or real surface topography measurements. Within that formulation the nodes of the grid used in the contact analysis are denoted by *i, j* and correspond to the location in a cartersian grid with the coordinate x,y, where the indices i and j refer to the grid columns and rows. The nodal value of any continuous distribution (such as p(x,y)) over Ω is denoted by p_{ij}. The set of contacting nodes which exceed the yield pressure are denoted by M, all other contacting nodes with $p_{ij} > 0$ are denoted by N. Following relationship then holds true

$$M \subset N \subset \Omega \tag{2.1}$$

The following input must be acquired: grid parameters (e.g. size, spacing), maximum pressure, the accuracy goal ϵ for the conjugate gradient iteration and auxillary variables.

$$p_{ij} > 0,\ G_{old} = 1,\ \delta = 0 \tag{2.2}$$

The surface deflections $u_{ij} \in \Omega$ are computed as a convolution of K^p from Eq. 1.20 and K^s from Eq. 1.22 and p over Ω.

$$u^z_{ij} = \sum K^p_{i-k,j-l}\, p_{kl} + \sum K^s_{i-k,j-l}\, \mu\, p_{kl}, (i,j) \in \Omega \tag{2.3}$$

The gap distribution is normalized by its mean gap over Ω by:

$$\acute{g}_{ij} = u^z_{ij} + h_{ij}\ , (i,j) \in \Omega \tag{2.4}$$

$$\overline{\acute{g}} = N_c^{-1} \sum_{(i,j)\in N-M} \acute{g}_{ij} \tag{2.5}$$

$$\acute{g}_{ij} = \acute{g}_{ij} - \overline{\acute{g}}\ , (i,j) \in \Omega \tag{2.6}$$

then G_{New} is calculated by:

$$G_{New} = \sum_{(i,j)\in N-M} \acute{g}^2_{ij} \tag{2.7}$$

the direction in which the next step will be made is then assessed.

$$\acute{t}_{ij} = \begin{cases} \acute{g}_{ij} + \frac{G_{New}}{G_{old}} \acute{t}_{ij}\ , (i,j) \in N - M \\ \acute{t}_{ij} = 0\ , (i,j) \in (\Omega - N) \cup M \end{cases} \tag{2.8}$$

G_{New} is the stored in G_{Old}. Again a convolution with the descend direction $\acute{t}_{ij}$ is carried out and normalized in $N - M$:

$$\acute{r}_{ij} = \sum K^{p}_{i-k,j-l}\, \acute{t}_{kl} + \sum K^{s}_{i-k,j-l}\, \mu\, \acute{t}_{kl}, (i,j) \in \Omega \tag{2.9}$$

$$\overline{\acute{r}} = N_c^{-1} \sum_{(i,j)\in N-M} \acute{r}_{ij} \tag{2.10}$$

$$\acute{r}_{ij} = \acute{r}_{ij} - \overline{\acute{r}}, (i,j) \in \Omega \tag{2.11}$$

The resulting value r_{ij} is used to derive the length dd of the step to be made in the direction of tt_{ij}:

$$dd = \frac{\sum\limits_{(i,j)\in N-M} \acute{g}_{ij}\, \acute{t}_{ij}}{\sum\limits_{(i,j)\in N-M} \acute{r}_{ij}\, \acute{t}_{ij}} \tag{2.12}$$

Old nodal pressure values are stored for the next iteration step.

$$p^{old}_{ij} = p_{ij}\ , (i,j) \in \Omega \tag{2.13}$$

and the pressure values are adjusted as:

$$p_{ij} = p_{ij} - dd\, \acute{t}_{ij}\ , (i,j) \in N - M \tag{2.14}$$

In the next step, all tensile tractions, namely negative pressures, are set to zero. The corresponding nodes are consequently excluded from the current contact area. At the same time, the upper limitation of contact pressure is imposed. The maximum contact pressure is limited to that of the yield pressure of the considered material, which should be set to 1.1x - 3x the yield strength of the softer material [59]:

$$p_{ij} = p_{max} = p_{yield}\ , (i,j) \in M \tag{2.15}$$

This yield pressure then corresponds to the onset of yielding (1.1 x yield strength) and the fully plastic regime (3 x yield strength), respectively. The numerical load is then computed and the pressure distribution is adjusted to satisfy the static force equation.

$$W_N = \Delta x\, \Delta y \sum_{(i,j)\in\Omega} p_{ij} \tag{2.16}$$

$$p_{ij} = \frac{F_N}{W_N}\, p_{ij} \tag{2.17}$$

The relative error is then compared with the accuracy goal, deciding if a new iteration must be performed:

$$\epsilon = \frac{\sum_{(i,j)\in N} p_{ij} - p_{ij}^{old}}{F_N} \tag{2.18}$$

In the present study, a grid size of 512 x 512 elements was used. This grid size corresponds to the resolution of the surface topography measurement device.

2.4.2 Subsurface contact stress distribution

After the nodal contact pressures p_{ij} are calculated, the subsurface stresses can be calculated for a given depth z underneath the contact by the DC-FFT technique denoted by ($\otimes$) as follows:

$$\sigma_{kl}(x,y,z) = p(x,y) \otimes T_{kl}^{p}(x,y,z) + \mu\, p(x,y) \otimes T_{kl}^{s}(x,y,z) \tag{2.19}$$

Due to the extent of occurring wear and associated near-surface material alterations within the ultra-mild sliding wear regime a depth analysis of the damage variable *d* was conducted up to a depth of 300 μm with an increment of $\Delta z = 2.5 \mu m$. With the grid size of 512 x 512 adopted from the contact pressure calculation, a total number of 33554432 (512 x 512 x 128) elements were used in this contact stress calculation.

2.4.3 SDFP and affected contact area A_{Aff}

The sdfp is the product of the calculated pressure distribution p(x,y), the measured coefficient of friction μ and the relative sliding velocity v_{rel}.

$$sdfp_i = p_i(x,y)\mu_i v_{rel,i} \tag{2.20}$$

The SDFP [$\mathrm{W\,mm^{-2}}$] as the sum of the $sdfp_i$ is calculated over one half cycle of the reciprocating sliding wear test. In order to simulate the relative movement of the counter body, the acutal displacement and basic kinematic rules were used. The data acquisition was conducted with a sampling frequency of f_{sample} = 2048 Hz. Hence with a wear test frequency of f_{Test} = 5 Hz there are N_{DP} = 204 data points available for one half cycle of the reciprocating movement.

$$SDFP = \sum_{n=1}^{N_{DP}} sdfp_i \tag{2.21}$$

An example of the SDFP of the counter body and the body is shown in Figure 15. In order to further examine the SDFP a histogram was calculated from values greater than 0. Here the calculated SDFP values are counted as a frequency of occurrence in discrete and constant SDFP intervals. From this either a histogram or a cumulative frequency diagram (Figure 16) can be derived. The affected

contact area is then proportional to the frequency of occurrence (FoO) and the lateral resolution of the calculation domain Δx and Δy.

$$A_{Aff} = FoO\,\Delta x\,\Delta y \tag{2.22}$$

The affected area is then accumulated and plotted versus the related SDFP (Figure 17).

2.4.4 Multi-axial fatigue criterion

According to Eq. 1.48 the fatigue damage variable d is calculated in each calculation step (time instance) regarding the stationary base and moving counter body. The fatigue limits used to calculate α and β are generally not determined with case hardened test samples. The gradient of the hardness profile can be utilized to approximate theoretical fatigue limits for the case hardened layer. The fatigue limits for the blank-hardened state for reversing tension and torsion are listed in Table 6.11. Fatigue limits from the literature [60, 61] and hardness profile measurements (see. Fig. 18 and 19) were used to correlate the fatigue limits of the carburized and case-hardened layer by linear extrapolation. In order to accelerate the calculation of the hydrostatic stress σ_H and the Tresca shear stress σ_T vectorized formulations were used to calculate the Cauchy stress tensor invariants and principle stresses.
The stress tensor invariants I_1, I_2 and I_3 are calculated as follows:

$$I_1 = \sigma_{xx} + \sigma_{yy} + \sigma_{zz} \tag{2.23}$$

$$I_2 = \sigma_{xx}\,\sigma_{yy} + \sigma_{yy}\,\sigma_{zz} + \sigma_{zz}\,\sigma_{xx} - \sigma_{xy}\,\sigma_{xy} - \sigma_{yz}\,\sigma_{yz} - \sigma_{xz}\,\sigma_{xz} \tag{2.24}$$

$$I_3 = \sigma_{xx}\,\sigma_{yy}\,\sigma_{zz} - \sigma_{xx}\,\sigma_{yz}^2 - \sigma_{yy}\,\sigma_{xz}^2 - \sigma_{zz}\,\sigma_{xy}^2 + 2\sigma_{xy}\,\sigma_{yz}\,\sigma_{xz} \tag{2.25}$$

The calculation of auxiliary values Q, R, ϕ and B is needed to calculate the principal stresses σ_1, σ_2 and σ_3.

$$Q = \frac{3I_2 - I_1^2}{9} \tag{2.26}$$

$$O = \frac{2I_1^3 - 9I_1I_2 + 27I_3}{54} \tag{2.27}$$

$$\zeta = cos^{-1}\left(\frac{O}{\sqrt{-Q^3}}\right) \tag{2.28}$$

$$B = 2\sqrt{-Q} \tag{2.29}$$

Finally the principles stresses become.

$$\sigma_1 = B\,cos\left(\frac{\zeta}{3}\right) + \frac{I_1}{3} \tag{2.30}$$

$$\sigma_2 = B\,cos\left(\frac{\zeta + 2\pi}{3}\right) + \frac{I_1}{3} \tag{2.31}$$

$$\sigma_3 = B\ cos\left(\frac{\zeta + 4\pi}{3}\right) + \frac{I_1}{3} \tag{2.32}$$

The hydrostatic stress σ_H is calculated from the first Invariant of the stress tensor.

$$\sigma_H = \frac{I_1}{3} \tag{2.33}$$

The maximum shear stress is determined the following calculation step.

$$\sigma_T = \frac{1}{2} max\left(\left|\sigma_1 - \sigma_2\right|, \left|\sigma_2 - \sigma_3\right|, \left|\sigma_3 - \sigma_1\right|\right) \tag{2.34}$$

The critically affected volume (CAV) is calculated from the number of elements which fulfill the criterion $d \geq 1$ multiplied by the elementary volume of a calculation cell $V_{cell} = \Delta x\ \Delta y\ \Delta z$.

Results

All eight tribosystems were analyzed regarding their tribological performance during running-in. The results of the wear test as well as the results of the contact simulations introduced in Chapter 2 will be presented in the following chapter.

3.1 Wear test characteristics

3.1.1 Lubrication regime

The calculated minimum film thickness according to Equation 1.55 was $h_{min}^{CS} \approx 70nm$ for the CS wear test conditions and $h_{min}^{CHI} \approx 7nm$ for the CHI wear test conditions. The resulting λ - ratios are shown in Figure 20 for the CS test series and in Figure 21 for the CHI test series. Regarding the CS test series the highest λ-ratio is reached by the polished body of about $\lambda_P^{CS} \approx 0.8$ at the beginning of the wear test, which decreases down to a value of about $\lambda_P^{CS} \approx 0.17$ at the end of the wear test. The milled & finished sample starts with the second highest value of $\lambda_{MF}^{CS} \approx 0.5$ which decreases down to $\lambda_{MF}^{CS} \approx 0.3$ at the end of the wear test. In contrast to those two the lubrication condition of the milled sample improves slightly in the vicinity of $\lambda_M^{CS} \approx 0.2$ and that of the ground sample nearly stays constant at $\lambda_{GR}^{CS} \approx 0.4$. The lubrication condition of the CHI samples improves slightly, except for the polished surface topography. Regarding this wear test series all λ - ratios remain below 0.1. In summary all λ-ratios are less than one for all conducted wear tests.

3.1.2 Coefficient of friction

The coefficient of friction (*CoF*) over wear test time is shown in Figure 22 for the CS wear tests and in Figure 23 for the CHI wear test series. These values correspond to the mean values and the standard deviation of the mean value during each wear test interval. The notation S signifies the CoF within the first wear test interval, the notation E signifies the CoF within the last wear test interval, which should render the overall performance during testing time.

CS test series

The milled and ground samples show a decreasing CoF over testing time. The CoF of the ground surface topography starts and ends with overall highest values of about $\mu_{GR} = 0.12 \pm 0.005(S) \rightarrow 0.108 \pm 0.003(E)$, the milled exhibits a CoF of about $\mu_M = 0.099 \pm 0.003(S) \rightarrow 0.084 \pm 0.003(E)$. In contrast to that the milled & finished surface topography shows a mainly constant CoF of about $\mu_{MF} \approx 0.088 \pm 0.0005(S\&E)$. In case of the polished surface topography a slightly increasing CoF of $\mu_P \approx 0.088 \pm 0.0005(S) \rightarrow 0.093 \pm 0.002(E)$ was measured over testing time.

CHI test series

Regarding the CHI wear tests the milled and the milled & finished surface topography display high coefficients of frictions over test time. The milled surface topography displays a mean CoF of about $\mu_M = 0.12 \pm 0.0017(S) \rightarrow 0.12 \pm 0.0025(E)$. An increasing CoF was recorded for the milled & finished surface topography, of $\mu_{MF} = 0.12 \pm 0.005(S) \rightarrow 0.14 \pm 0.0012(E)$. The polished and the ground base body surface topography reveal a decreasing CoF up to 300K and 600K wear test cycles followed by an increasing CoF towards the end of the wear test. The polished sample starts with a slightly lower mean CoF of $\mu_P = 0.09 \pm 0.024(S)$ decreasing to $\mu_P = 0.06 \pm 0.008$ in the first 300.000 wear test cycles and then increases up to $\mu_P = 0.073 \pm 0.003(E)$ towards the end of the wear test. The ground sample starts with a CoF of $\mu_{GR} = 0.11 \pm 0.0152(S)$ decreasing to $\mu_{GR} = 0.05 \pm 0.025$ in the first 600k wear test cycles which then increases up to $\mu_{GR} = 0.074 \pm 0.007$ towards the end of the wear test.

3.1.3 Wear volume

The wear volume of both test series is shown in Figure 24 and Figure 25 separately for the base and the counter body after 2.0M wear cycles. Regarding the CS test series the wear volume of the milled & finished and of the polished surface topography could not be measured by a weighing scale (resolution $\Delta m = 10^{-4} g$) nor by surface subtraction techniques as described in Chapter 2.2.1. The total wear volume of the ground surface topography shows the highest value of about $W_{GR} = 6.74\,x\,10^5\,\mu m^3$ of all tested surface topographies in this test series, which is mainly attributed to the wear of the counter body.

Regarding the CHI wear test all wear volumes are greater compared to the CS tests series. The milled & finished surface topography exhibits the highest total amount with about $W_{MF} = 2.4\,x\,10^6\,\mu m^3$ in this test series. All the other couples have wear volumes in the range of $W_M \approx W_{GR} \approx W_P \approx 1.5\,x\,10^6\,\mu m^3$. However the contribution to the total wear volume from the counter body and the base body varies. By looking at the partitioning of the wear volume it turns out that the counter body of the ground sample has worn the most.

3.1.4 Wear appearances

SEM images of the wear appearances after 2M wear test cycles of the CS test series are shown in Figure 26, the wear appearances of the CHI wear test series are shown in Figure 27. In these figures the wear appearances of the base bodies are depicted on the left side, those of the counter bodies on the right side.

CS test series

The characteristic wear appearances are smoothing of the wear track and a small number of grooves which are aligned in the direction of sliding and which developed on both the base and the counter body. On the milled base body (Fig. 26 (a)) vertical machining marks are still visible. Inside the wear track the summits of the machining marks are partially flattened, smooth and show slight grooves. The wear track on the counter of the milled sample (Fig. 26 (b)) is hardly visible. It can be distinguished by fine grooves and small indentations, presumably from wear particles. The machining marks of the ground base body (Fig. 26 (c)) are clearly visible. A differentiation between machining marks and wear grooves is not possible from this image. The counter body shows flattening, grooves in the direction of sliding and flaking within the nominal contact area. The polished as well as the milled & finished sample show few grooves (Fig. 26 (e & g)) on the base body, while the milled & finished base body still shows some machining marks. Both corresponding counter bodies (Fig. 26 (f & h)) do not clearly show a circular flattened nominal contact area. On the counter body of the polished sample grooves appear more severe compared to the counter body of the milled & finished sample.

CHI test series

Regarding the CHI the wear appearances are quite similar, but differ in detail. A circular shaped nominal contact area is clearly visible on all counter bodies of this wear test series. The grooves on the milled base body (Fig. 27 (a)) appear quite similar to those on the milled steel base body, but are more pronounced. The counter body is flattened and slight grooves appear and an early state of flaking can be seen (Fig. 27 (b)). Test residue from lubricant and wear particles remain after cleaning. The machining grooves of the ground sample are dominant in Figure 27 (c). Again grooves and flattening from tribological loads can not be clearly differentiated. The corresponding counter body shows a clear boundary of the contact, grooves and small pittings (Fig. 27 (d)). The polished base body shows a smooth surface with residue from lubricant and a crack in the center of the figure (Fig. 27 (e)). The crack tends to follow the direction of sliding, but is changing its direction several times. On the counter body a small number of wear particles and small pitting can be seen (Fig. 27 (f)). The milled & finished base body (Fig. 27 (g) exhibits flattening on the remaining machining summits. The counter body displays grooves, small pitting and adhering wear particles (Fig. 27 (h)).

3.2 Contact Analysis

The contact pressures, the corresponding subsurface contact stress distributions and SDFP surface plots will be presented for the initial contact condition in order to illustrate the differences between the tested tribosystems. Furthermore SDFP vs acc. A_{Aff} and micro contact fatigue analysis will be presented at characteristic wear test intervals. Regarding the contact fatigue analysis of the the CS test series the critically affected volume is presented for the base and the counter body in one graph due

to the self-mating contact and similar fatigue limits, regarding the CHI test series the contact fatigue analysis is presented for the base and counter body separately.

3.2.1 Contact Pressure

The pressure distributions of the initial contact are calculated from measured unworn surface topographies. The topographies measurements have typically a dimension of 0.8 mm x 0.8 mm with a lateral resolution of of Δx = Δy = 1.5656 µm. The point of origin of contact pressure calculation is in the middle of the presented domain.
The maximum contact pressure threshold of the CS couples is set to assumed yield pressure of about $p_{max} = p_{yield}^{CS} = \left(\frac{650x9.81}{3.0}\right) x2.0 \approx 4251$ [MPa] and $p_{max} = p_{yield}^{CHI} = \left(\frac{550x9.81}{3.0}\right) x2.0 = 3597$ [MPa] from hardness measurement (see Figure 18 & 19). The initial calculated contact pressure distribution of the CS and the CHI wear test series are presented in Figure 28 (a-d) and in Figure 29 (a-d), respectively. As can be seen from these figures different contact pressure distributions arise as a result of the orientation and the height of the surface finish machining marks and surface topography features.

CS test series

Regarding the milled surface topography mainly 3 vertical contact spots are obtained within the initial contact situation 28 (a), one main contact spot in the middle and two smaller contact spots nearby. Within the main contact spot the yield pressure is reached by a small amount of the contact area. The initial pressure distribution of the ground surface topography exhibits row type and highly loaded contact spots 28 (b). Here the yield pressure is reached primarily. Beside the row type contact spot, scattered and individual contact spots are obtained as well. The milled & finished and the polished surface topography achieved a Hertz'ian type circular contact 28 (c & d). The milled & finished surface topography is similar to the polished contact distribution and exhibits a circular contact area. The influence of remaining machining marks of the milling process is apparent. At the edges of this remaining machining marks, increased calculated contact pressures do occur. At this machining marks contact spots reach the predefined yielding pressure. In case of the polished pressure distribution the defined yield pressure is not reached. The maximum calculated contact pressure is 1890 MPa and therefore 30 % higher than the maximum theoretical Hertz'ian contact pressure.

CHI test series

The contact pressure distribution of the initial contact of the CHI wear test series depends strongly on the machining and surface finish of the cast iron. The distribution of near-surface graphite nodules (se Fig. 27) affect the surface topography and, therefore, the calculated contact pressure. The milled surface topography exhibits a clearly localized and discontinuous pressure distribution (Fig. 29 (a)); spherical contact spots reach the yielding pressure. The machining marks are slightly visible but do not dominate the contact characteristics. The pressure distribution of the ground surface topography again

exhibits a row like character (Fig. 29 (b)). Contact spots reaching the yield pressure are concentrated in the middle of the contact area. The milled & finished surface topography shows a clearly divided contact pressure distribution (Fig. 29 (c)). Two main contact spots can be observed which are addressed to the final surface finish. Within these contact spots the yield pressure is reached commonly. A spherical contact spot in the middle of both main contact spots is present, which again yield the defined pressure limit. The polished contact exhibits a circular contact area with relative low contact pressures (Fig. 29 (d)). Here a small number of contact spots reach the yielding pressure.

3.2.2 Subsurface contact stress distribution

The contact stresses are a successive result of the calculated contact pressure distributions and the measured coefficient of friction (see. Eq. 2.19). As the pressure distributions vary within the wear test series, the contact stresses do as well. The initial Von Mises contact stresses are shown in Figure 30 (a - d) and Figure 31 (a - d) for the CS and the CHI test series, respectively. Contact stresses are a 3D volumetric phenomena, here one slide in the y-z plane through the point of origin is presented up to a depth of 300 μm.

CS test series

The contact stress of the milled contact displays three section which can be matched with the contact spots of the pressure distribution (Fig. 30 (a)). A maximum of ≈ 1050 MPa arises at 10 μm beneath the surface. At a depth of 150 μm the contact stress decreases to ≈ 350 MPa. The contact pressure of the ground surface topography causes highly localized contact stresses underneath the surface (Fig. 30 (b)), which occur in comparable small patches. Within those patches calculated Von Mises contact stress of about 2380 MPa is reached at a depth of 5 μm underneath the surface. The contact stress decrease to 130 MPa at a calculated depth of 300 μm. The milled & finished as well as the polished contact pressure distribution of a smooth Hertz'ian like contact (Fig. 30 (c & d)). Due to the occurrence of high pressure peaks at the edges of machining marks of the milled & finished surface topography, stress concentration do occur. Here the calculated Von Mises stress can reach $\approx$ 900 MPa close to the contacting interface. At a depth of $\approx$ 50 μm the Von Mises stress of the polished reaches $\approx$ 800 MPa. Very high stresses calculated are an results of the contact model, used in this study as the influence of the plastic deformation are mostly underestimated. During running-in those high stresses would immediately produce wear particles and plastic deformations of the near-surface material.

CHI test series

Regarding the CHI contacts, higher stresses are calculated compared to the CS contacts, which are attributed to the different contact pressure distributions. Here Von Mises stresses of 1500 - 2000 MPa are reached more commonly up to a depth of $\approx$ 30 μm underneath the surface. Within the maximum calculated depth of 300 μm the Von Mises stresses decreases down to 130 - 150 MPa for all

tribosystems within the CHI test series. Except the Von Mises stress characteristic of the ground CS couple, the Von Mises stress of the CHI couples are more concentrated compared to the CS couples.

3.2.3 SDFP distributions

SDFP surface plots are shown separately for the base and the counter body in Figure 32 - 47 for the first half cycle of the conducted wear tests.

CS test series

The SDFP surface plots of the base body of the CS wear test series are shown in Figure 32 - 35, the SDFP surface plots of the corresponding counter bodies are shown in Figure 36 and 37.

SDFP surface plots - BB: The surface topography of the milled sample exhibits a periodic SDFP distribution. Due to the contact stiffness the surface summits are deflected less than the summit height and, therefore, only the peaks of the summits are affected (Fig. 32). A maximum of 181 $\frac{W}{mm^2}$ is reached calculatively in scattered contact spots over this half cycle of the reciprocating movement. The SDFP of the ground sample generally displays higher SDFP values. A maximum of 620 $\frac{W}{mm^2}$ is obtained at scattered contact spots caused by discontinuities of the surface topography (Fig. 33). The milled & finished sample initially exhibits a maximum SDFP value of 87 $\frac{W}{mm^2}$ (Fig. 34), the polished sample 43 $\frac{W}{mm^2}$ (Fig. 35). Due to the fact that the milled & finished and polished couple features the Hertzian contact pressure characteristics, the corresponding SDFP surface plots appear compact and smooth.

SDFP surface plots - CB: The counter body of the milled sample displays a maximum SDFP of 1028 $\frac{W}{mm^2}$ at the center of the power distribution (Fig. 36 (a)). The highest SDFP values are achieved by the ground sample with about 3313 $\frac{W}{mm^2}$ (Fig. 36 (b)). The SDFP of the counter bodies of the polished and milled & finished samples are concentrated in the center of the affected area. Again this is attributed to the Hertz'ian like pressure distribution, which features a parabolic pressure characteristic over the contact area. Due to this fact the SDFP accumulates in the center, higher values are achieved here compared to the milled sample. The counter body of the polished sample (Fig. 37 (a & b)) exhibits the second most maximum SDFP value of 1320 $\frac{W}{mm^2}$, the counter body of the milled & finish sample exhibits a maximum calculated value of 1470 $\frac{W}{mm^2}$ regarding the first half cycles of the wear test.

CHI test series

The SDFP surface plots of the base bodies of the CHI test series are shown in Figure 42 - 45, the SDFP surface plots of the corresponding counter bodies are shown in Figure 46 and 47.

SDFP surface plots - BB: Initially the SDFP distribution of the milled sample of the CHI test series exhibits a periodic character superimposed with localized spots of high calculated SDFP values. A

maximum value of 682 $\frac{W}{mm^2}$ is calculated over the first half cycle of the reciprocating wear test (Fig. 42). A maximum of 328 $\frac{W}{mm^2}$ is calculated regarding the SDFP distribution of the ground sample (Fig. 43). The SDFP of the polished sample displays a relatively smooth and compact characteristic (Fig. 45). Still a maximum of 280 $\frac{W}{mm^2}$ is calculated. The base body milled and the milled & finished sample display a periodic character of the SDFP distribution. Here a maximum SDFP of 286 $\frac{W}{mm^2}$ (Fig. 44) is calculated. Surface discontinuities have a distinct effect on the achieved SDFP distribution. These discontinuities contribute as concentrated SDFP spots or as voids within the SDFP distribution. Both types can mainly contribute as circular and scattered patches over the affected area.

SDFP surface plots - CB: The SDFP of the counter body of the milled sample appears blurred with a maximum value of 1574 $\frac{W}{mm^2}$ (Fig. 46 (a)), the SDFP of the counter body of the ground sample appears concentrated in rows with a maximum value of 2853 $\frac{W}{mm^2}$ (Fig. 46 (b)). The distribution of the SDFP of the milled & finished and the polished samples is circular with scattered spots of high power inputs. Within those localized spots maximum values of 4598 $\frac{W}{mm^2}$ (polished) and 2420 $\frac{W}{mm^2}$ (milled & finished) are achieved (Fig. 47 (a & b)).

3.2.4 SDFP vs. acc. A_{Aff}

In order to render the evolution of the SDFP and the affected area, the SDFP vs. A_{Aff} was analyzed for the first, the 600 thousandths and 2 millionth half cycle of the reciprocating wear test. Single plots are referred to as power lines. Important features are the evolution with testing time, the maximum and minimum SDFP and accumulated A_{Aff} values and the almost zero slope part of these curves.

CS wear test series: The SDFP vs. acc. A_{Aff} plots are shown in Figure 38 - 41 for the CS wear test series. All samples depict different characteristics. The milled base body exhibits the greatest enlargement of the affect area of this wear test series. From Figure 38 (a) it can be recognized that this enlargement occurred predominately within the first 600k cycles. An increase of the maximum calculated SDFP can be recognized between the power lines of the 600 thousandth and 2 millionth wear test cycle. The corresponding SDFP vs acc. A_{Aff} characteristics of the counter body do not follow this characteristic (Fig. 38 (b)). The enlargement of the affected area is not that pronounced. After 2M wear test cycles the affected area decreases and increases depending on the SDFP compared to the power line of the 600 thousandths wear test cycle. Up to a SDFP value of 230 $\frac{W}{mm^2}$ the affected area increases, thereafter it decreases. The SDFP vs. A_{Aff} power lines of the ground surface topography (Fig. 39 (a)) show a significant increase of the affected area after 600k wear test cycles. The corresponding maximum SDFP value decreases from initially 620 $\frac{W}{mm^2}$ down to 104 $\frac{W}{mm^2}$ at 2000k wear cycles. The rate of change between the 600k - 2000k is small compared to the rate of change between the first and the 600 thousandth wear test cycles. Again the characteristics of the SDFP vs. acc. A_{Aff} of the corresponding counter body (Fig. 39 (b)) differ significantly from those of the base body. A steady increase of the affected area can be observed with testing time. The rate of change depends on the

SDFP and vanishes below a SDFP of 60 $\frac{W}{mm^2}$. The characteristics of the SDFP vs. acc. A_{Aff} of the milled & finished (Fig. 40 (a)) and the polished (Fig. 41 (a)) base body are quite similar to each other, but differ in detail. Considering the polished sample a tilt of the characteristic can be recognized, which does not occur in the case of the milled & finished sample. A sequence of high calculated SDFP values at 600k wear test cycles vanishes towards the end of the wear test at 2M wear test cycles. In contrast to that the polished sample exhibits a steady increase of the power input. The power lines of the corresponding counter bodies ((Fig. 40 (b) & 41 (b)) display quite constant characteristics over testing time. The A_{Aff} is increasing slightly. The maximum SDFP decrease in case of the milled & finished and increases for the polished sample.

CHI wear test series: The SDFP vs. affected Area plots of the CHI test series are shown in Figure 48 - 51. Different characteristics can be observed for the tested base bodies as well as for the tested counter bodies. Regarding the milled base body the increase of the affected area is almost stunted after 600k wear test cycles. The characteristics of the 600 thousandths the 2 millionth wear test half cycle coincide quite well (Fig. 48 (a)). The affected area of the corresponding counter body renders a general increase after 20 $\frac{W}{mm^2}$ (Fig. 48 (b)). The ground sample exhibits different characteristics (Fig. 49 (a & b)). The power lines of the base body coincide well for the first and the 600 thousandths wear test cycles and the zero slope zone shifts to higher SDFP values. Towards the 2 millionth wear test cycles the affected area increases. Regarding the corresponding counter body the affected area increases for all SDFP values and all regarded wear test intervals. The affected area of the milled & finished base body increases steadily over wear testing time (Fig. 50 (a)). The counter body shows the same trend (Fig. 50 (b)). The polished surface topography starts with a highly localized character (zero slope part of the curve of the first wear test cycle, Fig. 51 (a)). The affected area increases over testing time. The zero slope part of the power lines does not change significantly over testing time. The corresponding counter body starts (Fig. 51 (b)) with the highest power input and a small affected area at the same time. Over testing time and the maximum power input decreases.

3.2.5 Contact fatigue analysis

The contact fatigue analysis was conducted on the basis of characteristic stress distributions of the tested tribosystem over one half cycle of the reciprocation sliding wear test. Those calculative elements which fulfill and/or exceed the fatigue limit criterion ($d \geq 1$) are summarized as to the critically affected volume (CAV). The presented results are statistics (mean values and standard deviations) of the critically affected volume over one half cycle. The statistics should highlight the fatigue load over testing time.

CS test series

The fatigue analysis of the base and the counter bodies of the CS test series is identical due to the self-mating contact and, therefore, similar fatigue limits. Thus the analysis represents the base bodies as well as the counter bodies. The theoretical fatigue limit $d \geq 1$ is exceeded by all contact conditions, except the initial polished contact. The mean values and standard deviations of the critically affected volume are shown in Figure 52. Here the CAV of the ground couple reaches the largest critically affected volume with $CAV_{GR} = 32445 \pm 22607$ [μm^3], followed by the milled couple with $CAV_M = 841.47 \pm 1500$ [μm^3]. The MF couple has a comparable small critical affected volume $CAV_{MF} = 9.58 \pm 24.195$ [μm^3] within the first half cycle of the wear test. The polished couple starts with a $CAV_P = 0$. Expect the ground couple the CAV is slightly increasing over testing time. High standard deviations compared to the mean value indicate the localized occurrence of critically affected volumes over the wear test movement.

CHI test series

Due to different fatigue limits the analysis is divided into the base and the counter bodies. The theoretical fatigue limit $d \geq 1$ is fulfilled by all contact conditions at least at the contacting interface. The mean values and standard deviations of the CAV are shown in Figure 53 and Figure 54. A trend to smaller volumes towards the end of the wear test can be observed from that analysis. The largest CAVs are calculated for the milled sample with ($CAV_M^{BB} = 14384 \pm 4375.3$ [μm^3], $CAV_M^{CB} = 541510 \pm 188710$ [μm^3]) followed by the milled & finished sample with ($CAV_{MF}^{BB} = 9647.4 \pm 3343.9$ [μm^3], $CAV_{M\&F}^{CB} = 684110 \pm 167380$ [μm^3]). Generally the counter bodies exhibit larger CAVs by an order of magnitude compared to the base body in this test series. The standard deviations are smaller than the average value, which indicated a more smooth distribution over the corresponding half cycle of the wear test.

Discussion

4.1 Wear test characteristics

4.1.1 Lubrication regime

The conducted wear test were designated to run under boundary lubrication. As can be seen from the results in Fig. 20 & 21 all calculated Tallian-Parameter are less than one. Thus according to the classical theory, all conducted wear tests can be considered to run under boundary lubrication conditions. Because in boundary lubrication the solids are not separated by the lubricant, fluid film effects are negligible and the load is carried by the deformation of the asperities. Additionally the friction coefficient should be independent of the fluid viscosity and its characteristics mainly driven by the properties of the contacting material and the chemical reactions at the contacting interface [46]. The variation of the Tallian-parameter is determined by the change of the equivalent surface roughness during wear test time. Within the CS test series the lubrication condition of the milled sample increases due to smoothing of the surface roughness. The lubrication condition of the ground surface topography can be considered as being constant, the milled & finished and the polished samples are roughen over testing time, attributed by wear groove generation. Here the lubrication of these both samples deteriorate over testing time. Within the CHI test series the variation of the Tallian-parameter should be neglected due to the uncertainties and simplifications of that model. All Tallian-parameter are less than 0.1 which signifies stable boundary lubrication condition. This is mainly attributed to the minimum film thickness of $h_{min}^{CHI} \approx 7$ nm. The equation for the minimum film thickness were developed for elliptical conjunctions, applied to materials of high elastic modulus under fully flooded and steady-state operation conditions [46]. The conditions might never been reached during the reciprocating sliding movement and, therefore, the real minimum film thickness might be even smaller than the calculated minimum film thickness.

4.1.2 CoF

The wear characteristics depends strongly on the surface finish achieved by different machining processes [9]. In this study industrial machining processes are used to machine a set of surface topographies in order to investigate the tribological performance of such surface finishes. The tribological characteristics differ significantly and basically two types of CoF characteristics [62] could be distinguished in each wear test series. The discussion can be lead by two aspects. One the one hand by the different local contact pressures, and, on the other hand by the differing microstructures. Regarding the aspect of the local contact pressure, shear stresses at points of the true contact depend linearly on the contact pressure [63, 64] which was also found in the conducted wear tests. Regarding the

microstructure, one has to keep in mind that the ductile cast iron features distributed graphite nodules, which can contribute to the friction characteristics as a solid lubricant [11].

CS test series

The contact conditions of the ground surface topography are predominately plastic. Due to this fact the highest initial CoF is reached by this surface topography. The second highest CoF is reached by the milled sample. Both CoFs decrease with wear test time, by implication the number of plastic contact spots decreases and milder contact conditions prevail. The milled & finished and the polished samples initially exhibit sufficient lower contact pressures and, therefore, generate lower CoF over wear testing time. The milled & finished sample displays small patches of plastic contact spots within the real contact area at remaining machining grooves. But these small patches of plastic contacts do not raise the CoF compared to the CoF of the polished sample. The slightly increasing CoF might be traced back to trajectory of wear particles within the contact. In case of the polished surface topography these (Fig. 26) act as third-bodies [65] and promote high contact pressures and more abrasive grooves. Remaining machining marks on the milled & finished can facilitate the removal of the wear particles out of the contact, if their size is smaller than the average valley width and depth [66].

CHI test series

The milled and the milled & finished samples display the highest CoF in this wear test series. Again high contact pressures and intermittent contacts spots result in high CoF characteristics over testing time in this test series. Opposed to this the CoF of the ground and the milled surface topography decreases with testing time. These CoF characteristics of the CHI wear test series can not be explained without taking the features of the microstructure and surface finish into account. One explanation could be the release of graphite from the nodules (see Fig. 55), which can act as a solid lubricant, if the surface finish and remaining metal cover on top of the graphite nodules allow for that [11]. The metal cover on top of the graphite nodules appear differently on all CHI wear test samples (Fig. 27), which depends on the final machining steps.

4.1.3 Wear Volume

The wear volume is divided as to the amount of wear volume of the counter and the base body. In this representation it is obvious that the counter body and the base body wear at different wear rates depending on the surface topography for both wear test series. Generally the base and the counter body do not share the same tribological load (counter body is constantly in contact, whereas the base body is not). Thus different wear rates might be an indication of mean stress sensitivity. The correlation of the wear performance with classical roughness parameter (see Chapter 1.4) is not possible. Although contact parameters like the plasticity index can render the tendency of from predominately plastic to elastic contact conditions [27, 67, 68], the tribological performance and the wear volume can not be

foreseen by them. The discussion of the measurement error associated with the surface subtraction technique is aggravated due to the fact that the surface height difference of two measurements must not necessarily coincide with the true wear volume. Contamination of the sample surfaces, the development of tribofilms and cyclic creeping during wear tests can influence the result of this technique. Thus the alignment of the reference marks is left to analysis experts. In order to achieve highly reliable wear volumes / rates the radionuclide technique can be applied. This technique allows for online-monitoring of the wear rate with a resolution of some nanometers per hour [69].

CS test series

The figures 56 and 57 display the wear volume characteristics over testing time. It can be seen that the characteristics of both samples are differently regarding the counter and base bodies. This is quite remarkable, since both material properties are alike. In case of the milled sample a similar wear rate is achieved after 600k wear test cycles, but the wear volume of the counter body is less than the wear of the base body which is mainly attributed to different wear rates between 300k and 600k wear test cycles. The characteristic of the wear volume of the ground surface topography exhibits different characteristics. The counter body wears approximately 5x more than the base body. The wear rate of the base body becomes vanishingly small after 75k wear test cycles. The wear volume of the polished and the milled & finished sample can not be measured either by weighing or surface subtraction techniques. Combined with the more stable CoF characteristics of the milled & finished surface topography, the enhanced performance can be attributed to the trajectory of the wear particles within the contact. Here the remaining valleys of the milling allow for the ejection of wear particles more easily compared to the polished surface topography and, therefore, these can not act as third bodies within the contact. Since the milled & finished sample achieved comparable tribological performances, it suggests that polishing as the final manufacturing step is not always superior.

CHI test series

The partition of the wear volumes of the CHI wear test series depends on the final surface finish, too. Interestingly the overall wear volumes are not influenced by the final machining step, except for the milled & finished contact couple. The milled & finished sample exhibits the highest overall wear volume, which can be attributed to the severe contact conditions. In order to optimize this tribosystem an friction energy related wear rate approach can be applied [11]. Figure 58 displays the approximation of the mean friction energy over one wear test cycle as the area of the red rectangular. The friction energy related wear rate is than the fraction of the total friction energy and the wear volume. The calculated energetic wear rates are shown in Figure 59. The base body of the ground surface topography exhibits the smallest energetic wear rate. Thus an optimization of this tribosystem should focus on the counter body.

4.1.4 Wear appearances & Wear mechanism

The presented SEM pictures of the worn surfaces display the wear appearances after 2M wear test cycles. From these pictures it can be seen, that the surface were mainly flattened and smoothed in both wear test series. Conventional interpretation of the wear appearances would imply abrasion and mild surface fatigue as the acting wear mechanism. To allow for such small wear volumes, submechanisms like microploughing [22] and low stress three body abrasion are required. An indication of tribochemical reactions and tribofilm generation can be seen from macroscopic images. Figure 60 displays the counter body of the milled surface topography of the CS wear test series. A formation of a tribofilm can be seen after 75k wear test cycles, which vanishes after 2M wear test cycles. The opposite can be seen for the counter body of the polished surface topography of the CHI wear test series in Figure 61. The formation of a brown layer is documented after 2M wear test cycles, whereas the formation of this tribofilm is interrupted in the middle of the nominal contact area. This suggests an tribosystem dependens on an optimal contact load for tribofilm generation [70], which is achieved temporarily and locally during the wear test time. Generally a precise identification of a classical wear mechanism is aggravated for such low wear volumes; obviously the wear includes chemical and mechanical mechanism [44]. Wear grooves might occur from few highly localized friction power inputs. Those are the fraction of the acc. affected area with the highest SDFP values as can be seen e.g. in Figure 36, represented by the almost zero slope part of the curves. The greater part of the affected area experiences smaller SDFP-inputs can be assumed to undergo mild surface fatigue and tribochemical wear.

4.2 Calculative contact analysis

4.2.1 Contact pressure and subsurface stress distribution

The discussion about the local contact pressure and associated contact stresses should be focused on the numerical contact solver scheme and the material parameters. The contact solver used in this work solves the contact with idealized linear-elastic and ideal-plastic material properties [58] (see. Fig. 62). By that pressure nodes which exceed a predefined maximum pressure value are set to maximum value and excluded from further iteration steps. The solver is neither able to calculate plastic deformations nor it is capable to calculate or incorporate residual stresses underneath the contacting surface, as can be looked up in [71–76]. The maximum pressure is set to 2x the mean yielding pressure. In this context 3x the yielding pressure is set equal to the hardness (HV10), which is correlated to the fully plastic region of an ideal plastic metal [59]. The macro hardness was chosen to represent a contact width characteristic property. But local hardness might differ significantly. Especially for the ductile cast iron, as graphite nodules are essentially softer than the metal matrix. The characteristic of the contact solver is shown in Figure 63 for the milled & finished surface topography of CHI wear test series. By

increasing the mean yield pressure, the micro contact area decreases. Whereas the maximum contact pressure is reached in every micro contact calculation in this particular case. Beside this limits of the contact solver, the material properties are modeled as homogeneous and isotropic. Especially this holds not true for the ductile cast iron. Due to the presence of the graphite nodules, which are distributed within the bulk material, one might expect higher contact pressures and stresses due to notch effects [76]. Nevertheless these restrictions can be expected to be compensated by using measured and ran-in surface topographies and wear test data, which served as an input to the contact solver. Since these measurements were carried out at predefined wear test intervals during wear tests, a quantitatively and realistic representation of the tribological performance over wear test time is insured.

4.2.2 SDFP vs. acc. A_{aff}

The SDFP and the affected Area A_{aff} are contact parameters, which are resolved on the μm-scale in this work. The SDFP represents a combined contact parameter, which incorporates numerically solved contact pressures and experimentally measured wear test data. These are the frictional coefficient and the relative sliding speed. The SDFP is the total amount of the specific dissipated friction power over a characteristic contact length of the conducted wear test series, which is one half cycle of the reciprocating movement. As it is a combination of numerically calculation and measured test rig data, it represents the contact load over wear testing time and is able to render the tribological load quantitatively. In this work it is represented separately for the counter and base body and should be used as a tool to analyze the wear and near-surface alterations of the contacting bodies. Still the exact partition of the dissipated frictional power into microstructural alterations, heat and wear particle generation is not known and should be addressed in future research [77]. The term affected area, purposely not mentioned as the micro contact area, draws attention to the fact that the local tribological load depends on the complete stroke of the wear test movement and surface topography variations. It can differ significantly from one specific solved contact situation [72, 76]. The summation of real contact areas must not be equal to the affected area over one half cycle of the reciprocating movement, as contact spots might come into contact several times while others do not. This is an important fact in the assessment of micro structural alterations, wear and wear particle generation (see Figure 64). As a theoretical assumption, tribosystems should tend from the bottom right to the upper left corner of these power line plots as can be seen from the characteristics of the milled base body of the CS wear test series. That means, that the tribosystems seek from high SDFPs and small affected areas to low SDFPs and larger affected areas. By that these plots could be used to formulate design guide lines, if corresponding threshold values are known. Regarding the high power proportions of the SDFP and associated A_{Aff} (red line in Fig. 64) these are thresholds for wear particle & grooves generation or crack initiation, regarding low power proportions (blue line in Fig. 64) threshold for beneficial tribofilms or tribolayer formations [70]. Between the low and high power thresholds there might be an optimum design space for high wear resistant tribosystems. An indication of the running-in performance is

the gap between two following power lines. But the evolution of the SDFP characteristic with wear testing time is still under discussion [11, 77]. They are quite sensitive to the initial tribological loading condition as can be seen from their variety of characteristic as presented (see Figure 65). This enlarges the classical understanding of running-in effects and should motivate to review dimensioning of tribosystems. The size and shape of contact spots together with the amount of dissipated friction power might influence the wear rates well, which again must be attributed in furhter analysis.

4.2.3 Contact fatigue analysis

The contact fatigue analysis is conducted on the basis of the calculated contact stresses over one half cycle of the reciprocation movement. The application of multi-axial fatigue according to Dan Vang to tribological loaded contacts is already shown by others and problems arise concerning the calibration of the fatigue limit [78, 79]. Regarding carburized and case-hardened samples, the material fatigue limits vary with the depth from the contacting surface to the bulk material. A linear correlation of the fatigue limit was utilized to estimate the fatigue limit of the hardened near-surface material by measured hardness value and know fatigue limits of unhardened fatigue samples [60, 61]. This simplification should be addressed in future studies and enhanced by measured fatigue data in order to model the fatigue properties of the near-surface material more precisely. Generally the results suggest that the critically affected volume is decreasing with wear test time, which match with a general understanding of running-in and decreasing wear rates. The results also suggests that the rate of decreasing depends on the surface topography and, therefore, the application of such fatigue models can increase the understanding of running-in processes. Furthermore it is distributed localized over the wear track, which coincides well with the presented wear appearances. In case of the polished sample of the CS wear test series, the $CAV_P = 0$ and, therefore, can not predict the occurrence of wear grooves which might be attributed to the simplifications made in that analysis. Regarding the CHI wear test series, the contact fatigue approach reveals general larger CAVs of the counter bodies, which agrees well with the larger wear volumes of the counter bodies in this wear test series. In optimization processes the ratio of the torsional and tension/compression fatigue limit, expressed by the fatigue parameter α, should be addressed. The analysis of the contact fatigue can be understood as an additional tool to design tribosystems. The prediction of the CAV and wear cycles to failure could be further improved, if low and high-cycle fatigue data would be available for the material and hardened state. An in-depth analysis of the damage variable reveals gradients to higher values of the damage variable *d* towards the contacting interface for all samples. The Figures 66 - 71 display the in-depth analysis of the damage variable d up to a depth of 0.3 mm underneath the contact for the first and last contact condition of the wear test. This analysis is presented in colormaps. The colorcode is proportional to the affected volume by counting the frequency of occurrence. At the contacting interface all tested samples are endangered to fatigue type of failure. The characteristics of these gradients depend on the considered surface topography. An intensification of the fatigue load can be recognized directly underneath for

all contacts with sustainable changes up to a depth of $\approx 100\ \mu m$. The shape of the distribution of the M&F couple of the CS wear test series is the most unaffected over testing time although the initially distribution of the damage variable features similar characteristics compared to the polished couple in the worn stage. Below the contacting interface the damage variable decreases rapidly. Regularly this gradient changes it characteristic up to 2000k wear cycles and follows the trend to smaller endangered volumes.

Summary & Outlook

In this work the specific dissipated friction power vs the affected contact area and contact fatigue analysis are utilized to evaluate wear experiments. Referring to technical relevant tribosystems, wear tests were carried out with self-mating carburized steel (18CrNiMo7-6) and case-hardened ductile cast iron (EN-GJS-HB 265) against 52100 steel couples under boundary lubrication. Different machining processes were used to obtain a set of surface topographies by means of commercially available industrial machining processes [57]. All tested tribosystems exhibits different running-in characteristics. The utilized micro contact parameters reflect the tribological load on top and underneath the contacting surface for the counter and base body separately and are capable to render the tibological loads over a characteristic contact length scale. The prediction of the tribological performance is still challenging due to not quantitatively described failure and wear sequences on the micro scale. The presented method should be understand as a starting point of a complete set of tribological and fatigue type material analysis as both types of loads render the service life time of modern and high wear resistant tribosystems. Mostly these material and/or system properties are considered separately, which aggravates their correlation. In order to model and predict material failures on a microscopical level, such as micropitting [80] and wear particle generation, transition of the tribological response and critical loads are to be determined without neglecting time-wise and local effects. This implies tremendous effort in numerical and laboratory investigations and should be targeted in future research activities. Here well aimed and combined tribological, high cycle fatigue tests and subsequently microstructural analysis has to be carried out. The cyclic deformation and fatigue properties are of great interest [81]. Thus cyclic high pressure torsion (HPT) [82, 83] experiments and galling resistance test methods [84, 85] are promising to render such cyclic fatigue and wear characteristics. Due to a large parameter space of multi-axial fatigue tests, in-phase HPT experiments near the torsional and tensile/compression fatigue limits could represent the starting point of investigation. Concerning the transferability to wear, the finite-life fatigue strength and the multi-scale character [86] of associated microstructural alterations [87] and crack initiation [88] has to be incorporated in post test analysis. Due to the great variety of wear mechanism, galling resistance test methods could render critical loads by load increasing tests to identify transitions of the tribological response. Furthermore the controlled generation of a wear resistant tribolayer can be promoted by well aimed tribological loads and selected lubricants as can be seen by the presented SDFP vs. A_{Aff} characteristics. Still those characteristics are challenging. Nevertheless all these efforts can lead to new design guidelines and parameters which then could be applied within the design step of tribologically loaded contacts, which illustrate the potential benefits of this new approach.

Tables

Table 6.1: Film thickness trends in tribological contacts

Period of time and Application	Film thickness [m]
Late 19th cemtury; Plain bearings	$10^{-4} - 10^{-5}$
Mid 20th century (1950)	10^{-5}
Late 20th century	$10^{-5} - 10^{-6}$
Late 20th century; dynamcially loaded	$10^{-6} - 10^{-8}$
End 20th century Asperity lubrication	$10^{-7} - 10^{-9}$

Table 6.2: Definition of tribosystem

Normal Force F_N	30 N
Stroke s	6 mm
Test frequency f_{test}	5 Hz
Sampling rate $f_{sampling}$	2048 Hz
Relative sliding velocity v_{rel}	60 mm/s

Table 6.3: Typical chemical composition of 18CrNiMo7-6

Element	Mass [%]
Fe	bal.
C	0.18
Si	0.20
Mg	0.70
Cr	1.65
Ni	1.55
Mo	0.30

Table 6.4: Physical Properties of 18CrNiMo7-6

Young's Modulus E	210 GPa
Possion's ratio ν	0.3
Thermal conductivity λ	49 $\frac{W}{mK}$
Spec. Heat capacity c	431 $\frac{J}{kgK}$
Density ρ	7770 $\frac{kg}{m^3}$

Table 6.5: Chemical composition of EN-GJS-HB 265

Element	Mass [%]
Fe	bal.
C	3.3 .. 3.8
Mg	0.02 .. 0.07
Mn	0.2 .. 0.5
Ni	0 .. 1
Si	2 .. 3

Table 6.6: Physical Properties of EN-GJS-HB 265

Young's Modulus E	170 GPa
Possion's ratio ν	0.275
Thermal conductivity λ	32.5 $\frac{W}{mK}$
Spec. Heat capacity c	515 $\frac{J}{kgK}$
Density ρ	7200 $\frac{kg}{m^3}$

Table 6.7: Chemical composition of 100Cr6

Element	Mass [%]
Fe	bal.
C	0.93 .. 1.05
Si	0.15 .. 0.35
Mn	0.25 .. 0.45
Cr	1.35 .. 1.6

Table 6.8: Physical Properties of 100Cr6 steel

Young's Modulus E	210 GPa
Possion's ratio ν	0.3
Thermal conductivity $\lambda_{Thermal}$	42.6 $\frac{W}{mK}$
Spec. Heat capacity c	470 $\frac{J}{kgK}$
Density ρ	7610 $\frac{kg}{m^3}$

Table 6.9: Root mean square roughness of machined base bodies

	$R_q[\mu m]$ - 18CrNiMo7-6	$R_q[\mu m]$ - EN-GJS-HB 265
Milled	0.358	0.551
Ground	0.151	0.378
Milled & Finished	0.1	1.062
Polished	0.007	0.056

Table 6.10: Oil data

	Mobile Gear SHC 320 (22 °C)	Mobile 1 ESP Formula 5W (80 °C)
Viscosity [cSt] η_0	320	72.80
Pressure-viscosity coefficient α_p [MPa^{-1}] [89]	0.015	0.012

Table 6.11: Fatigue limits of tested material

	Hardness HV 10	τ_t [MPa]	σ_{tc} [MPa]
18CrNiMo7-6 (blank-hardened) [60]	450	305	480
18CrNiMo7-6 (carburized)	650	440	693
EN-GJS-HB 265 [60]	300	205	240
EN-GJS-HB 265 (flame-hardened)	550	375	440
AISI 52100 (hardened) [61]	700	360	625

Figures

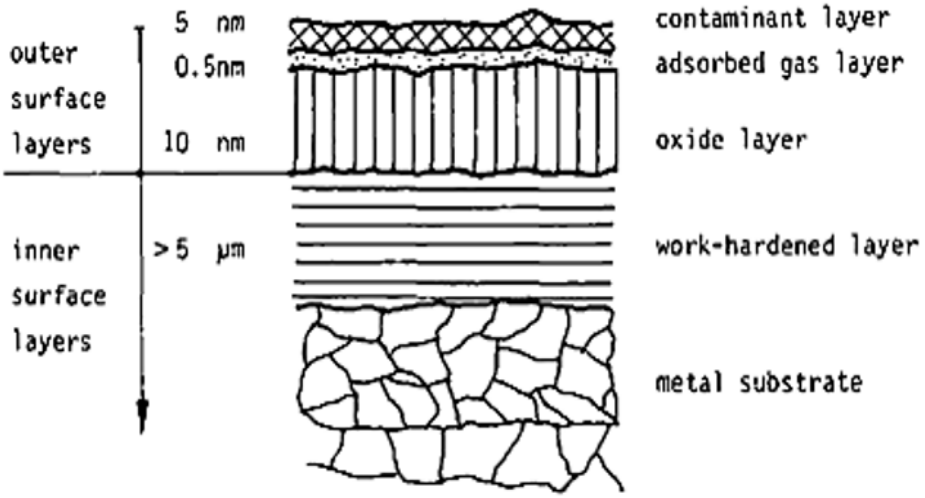

Figure 1: Sub-surface of technical materials

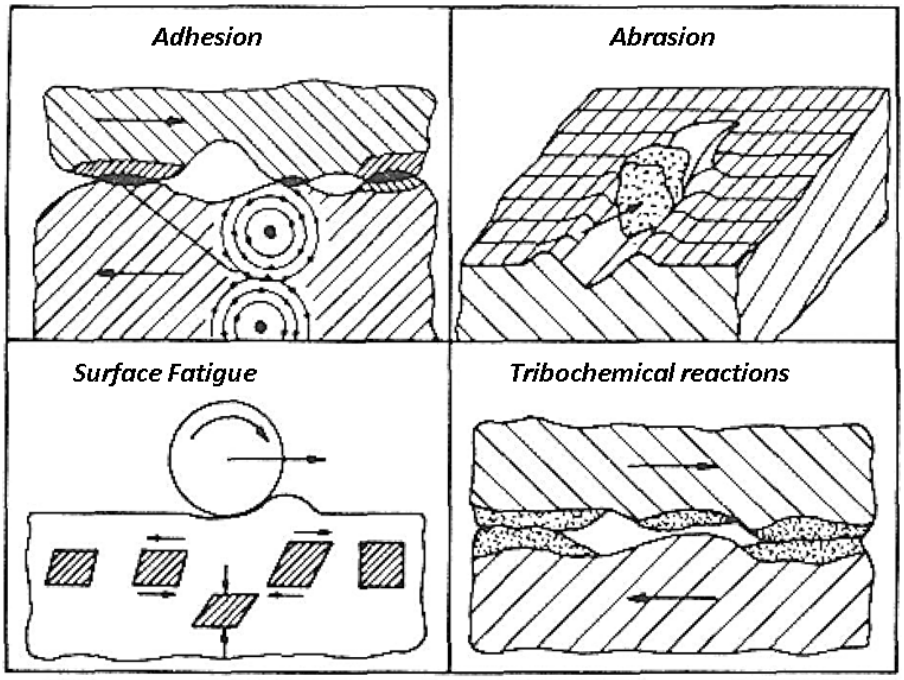

Figure 2: Four major wear mechanism

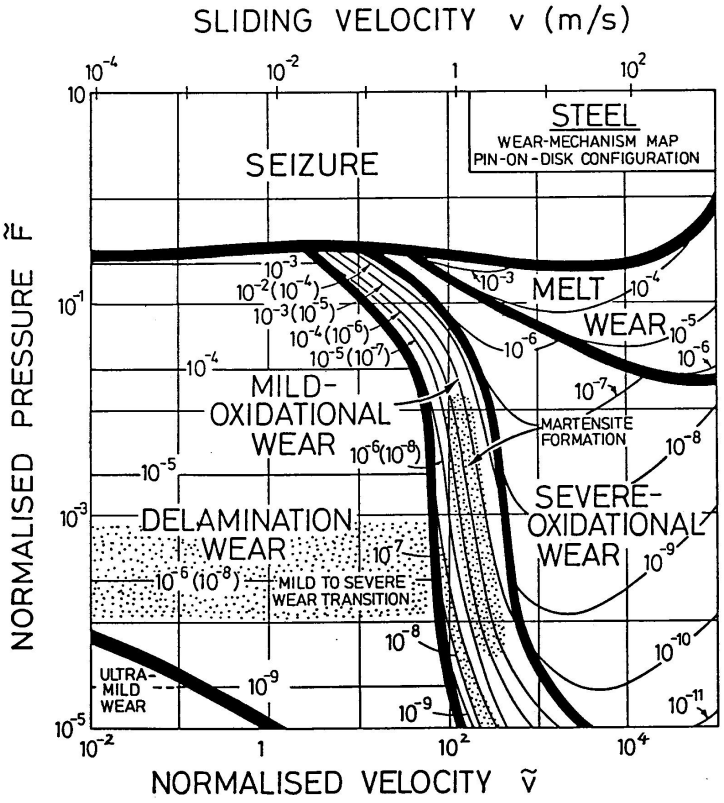

Figure 3: Wear map of steels [24]

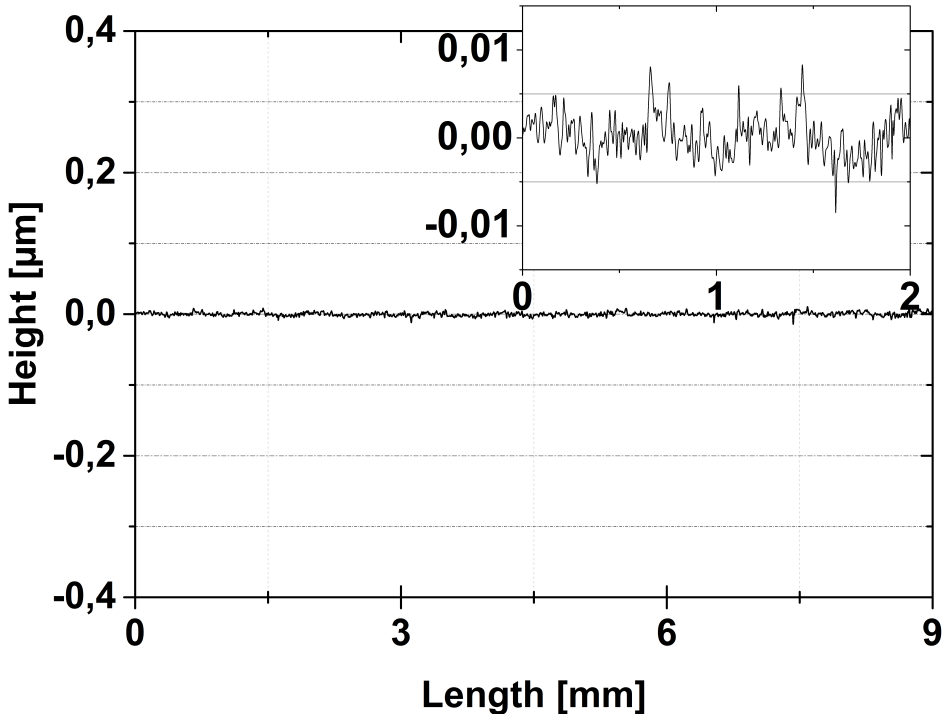

Figure 4: Mirror shine polished surface profile; $R_a = 0.002\ [\mu m]$, $R_q = 0.00257\ [\mu m]$

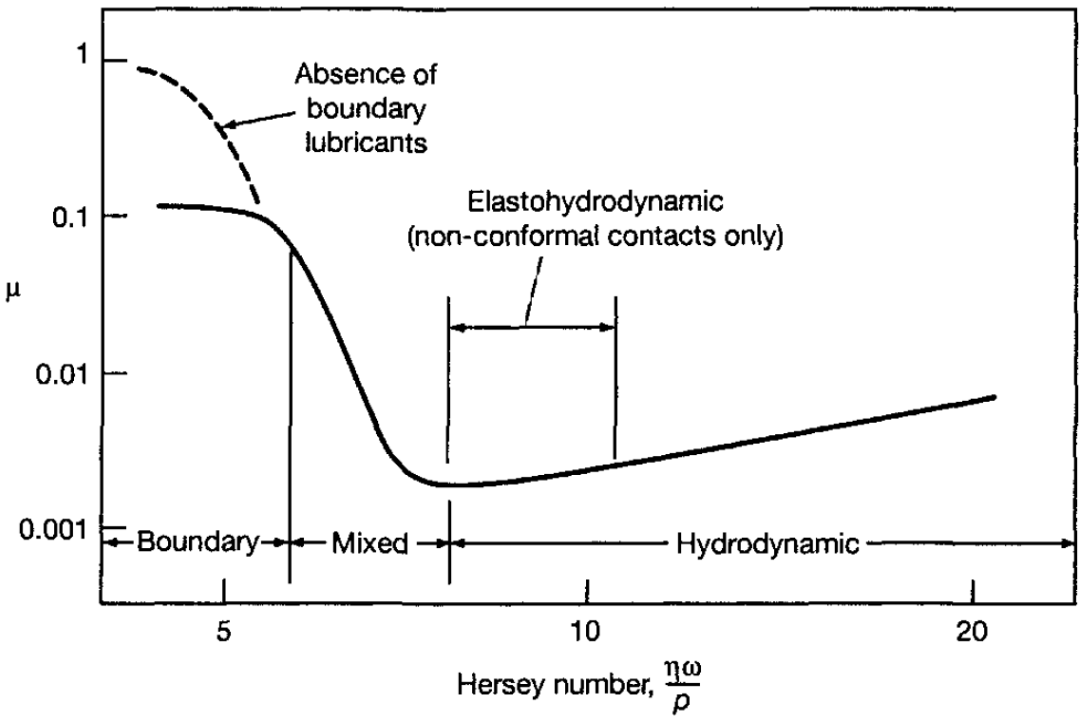

Figure 5: Stribeck curve [46]

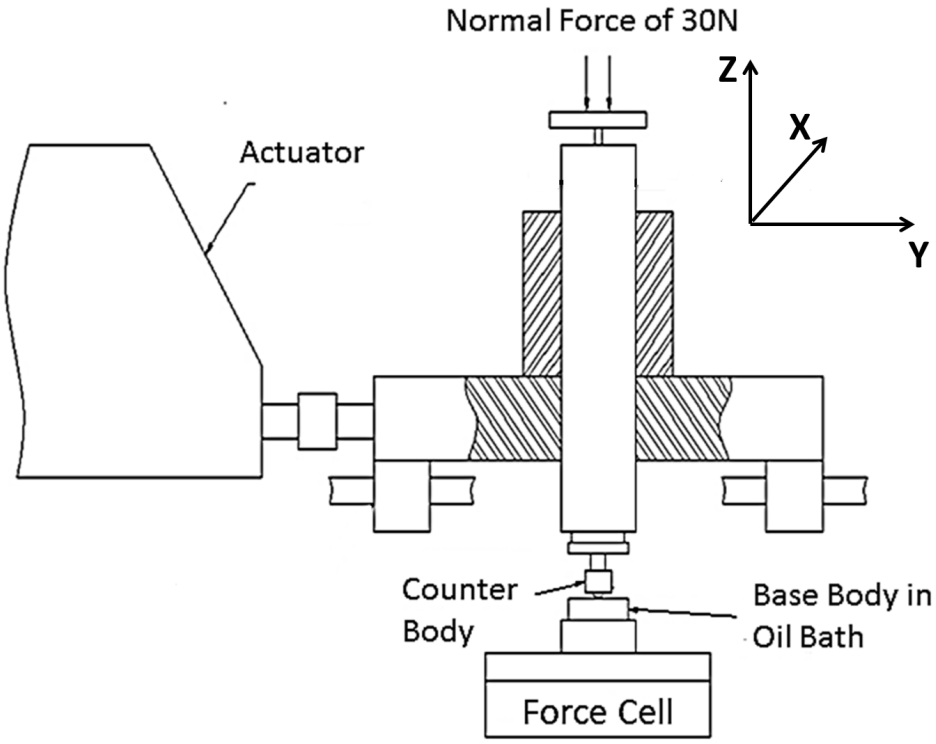

Figure 6: Custom built test rig (schematic) for reciprocating sliding wear tests

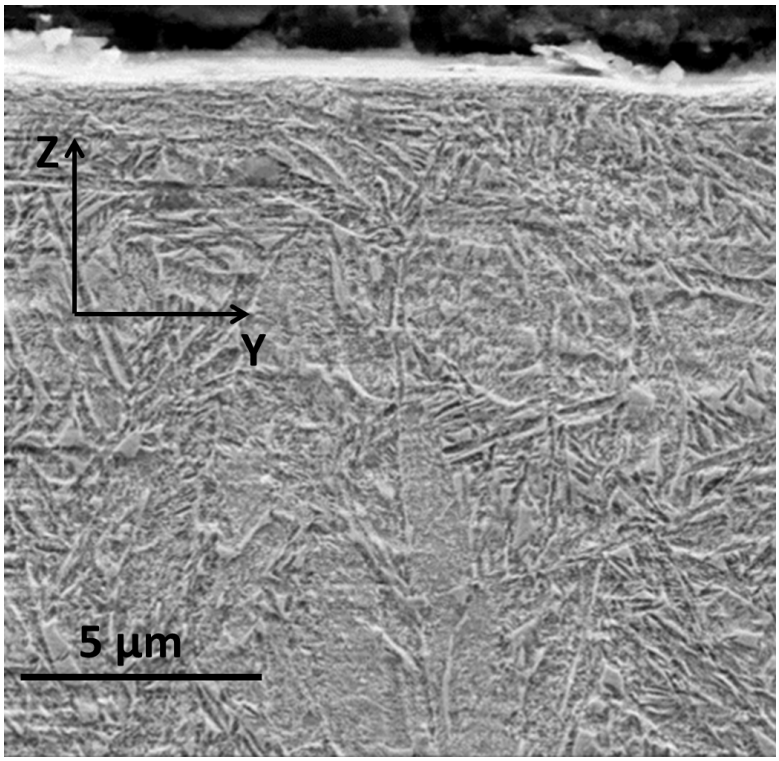

Figure 7: Typical microstructure of carburized 18CrNiMo7-6; SEM picture

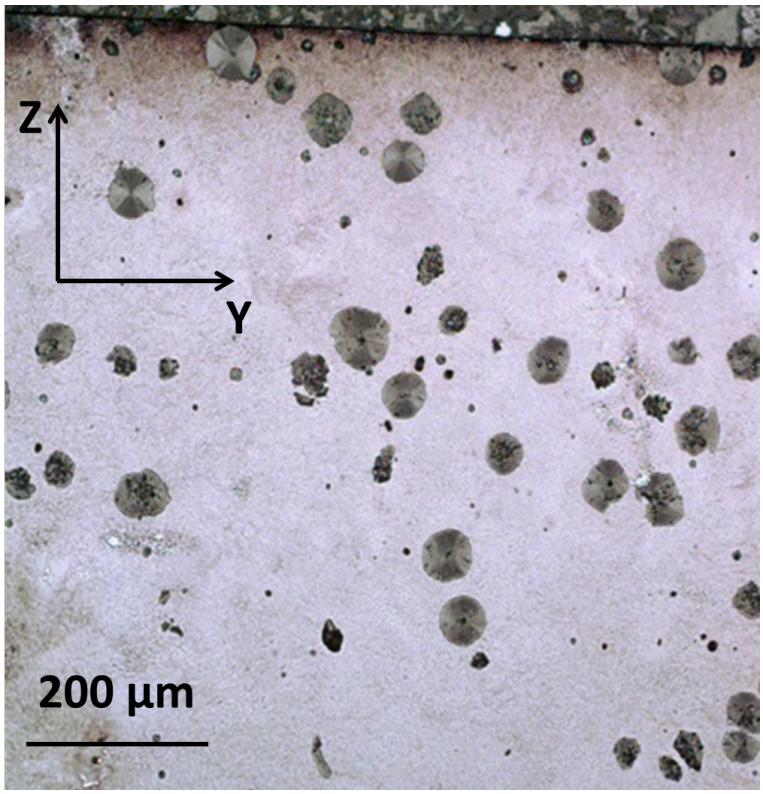

Figure 8: Typical microstructure of flame hardened EN-GJS-HB 265; white-light microscopy picture

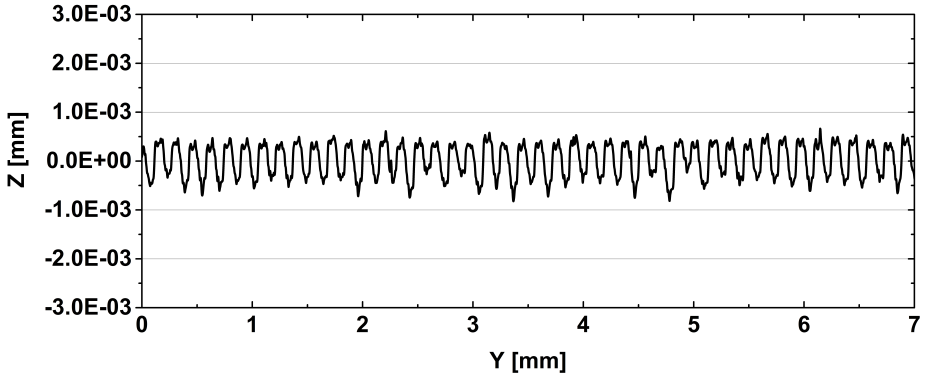

(a)

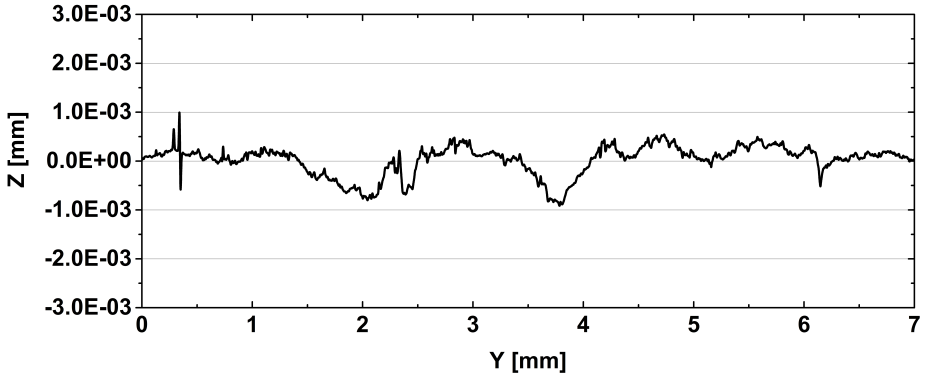

(b)

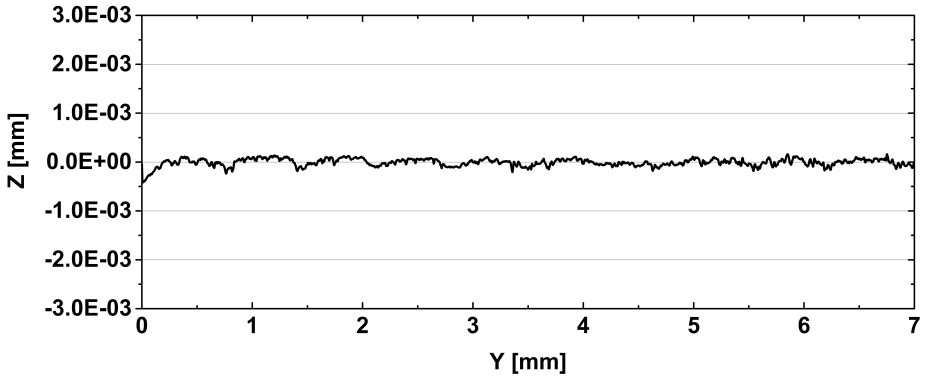

(c)

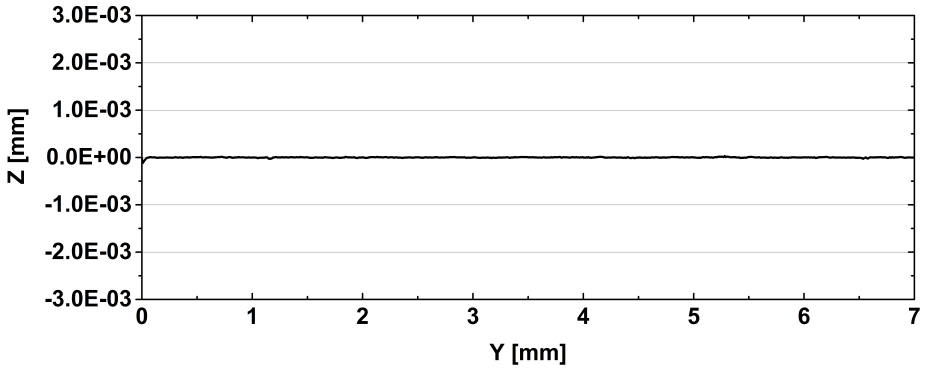

(d)

Figure 9: Surface line profiles of 18CrNiMo7-6 bodies; (a) milled, (b) ground, (c) milled & finished, (d) polished

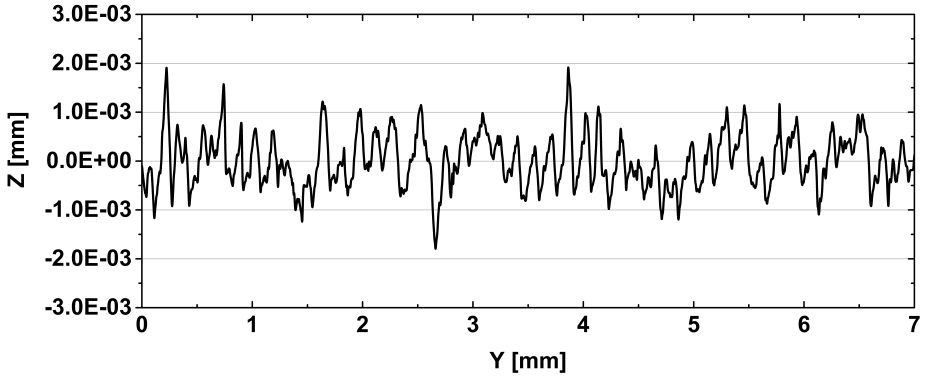

(a)

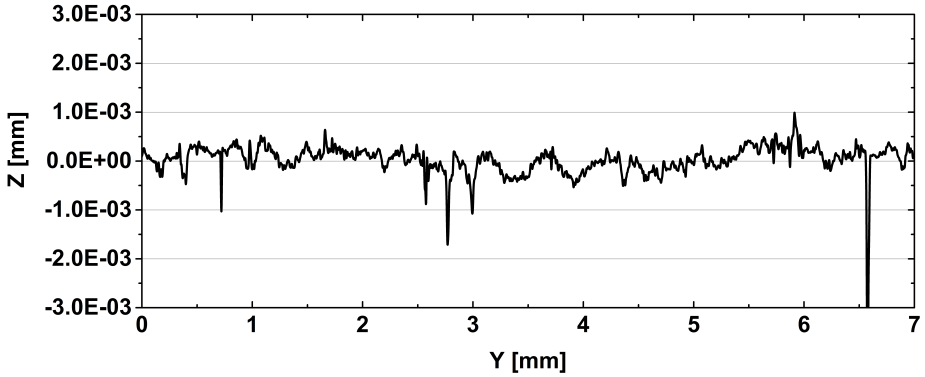

(b)

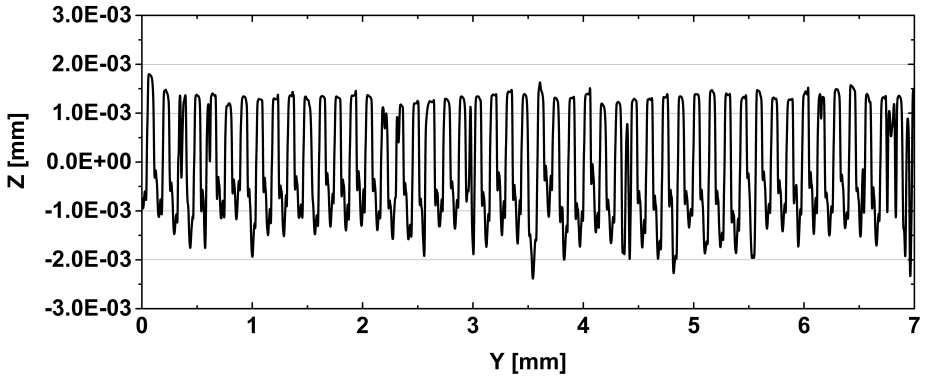

(c)

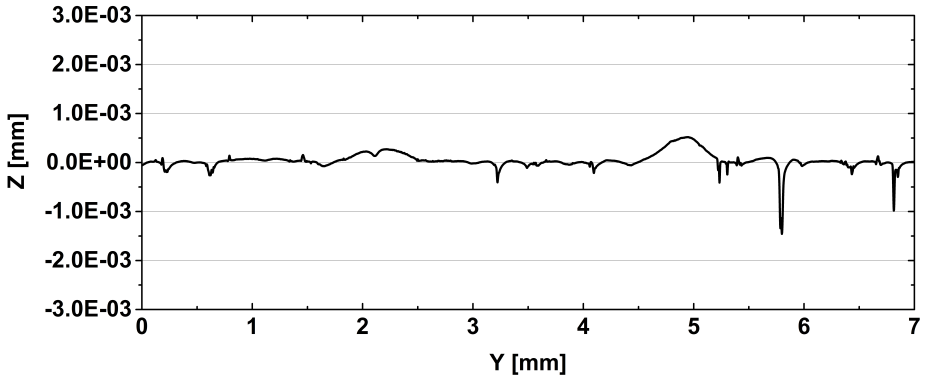

(d)

Figure 10: Surface line profiles of EN-GJS-HB 265 bodies; (a) milled, (b) ground, (c) milled & finished, (d) polished

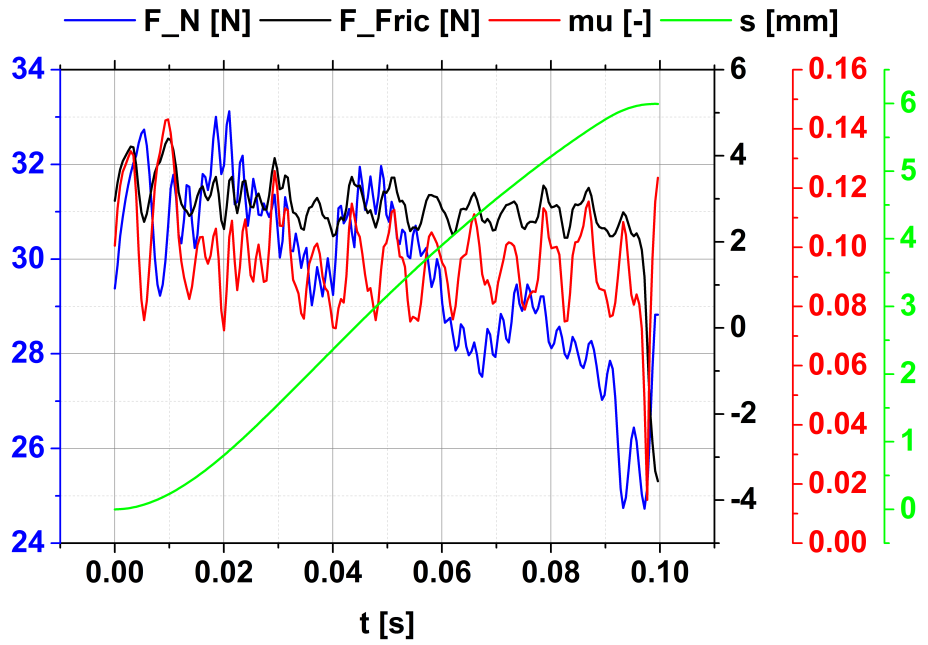

Figure 11: Example of test rig data over one half cycle of the reciprocating sliding wear test

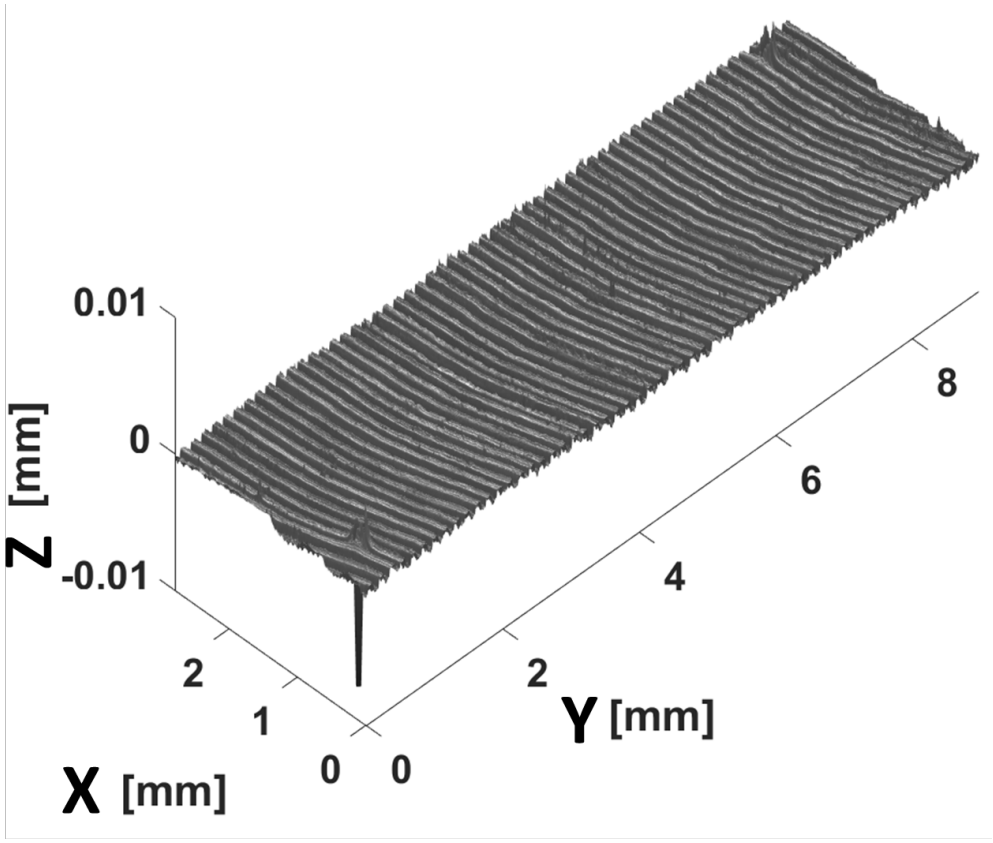

Figure 12: Surface topography measurement
Milled surface topography, 18CrNiMo7-6 (Axis-ratio $1 : 1 : \frac{1}{200}$)

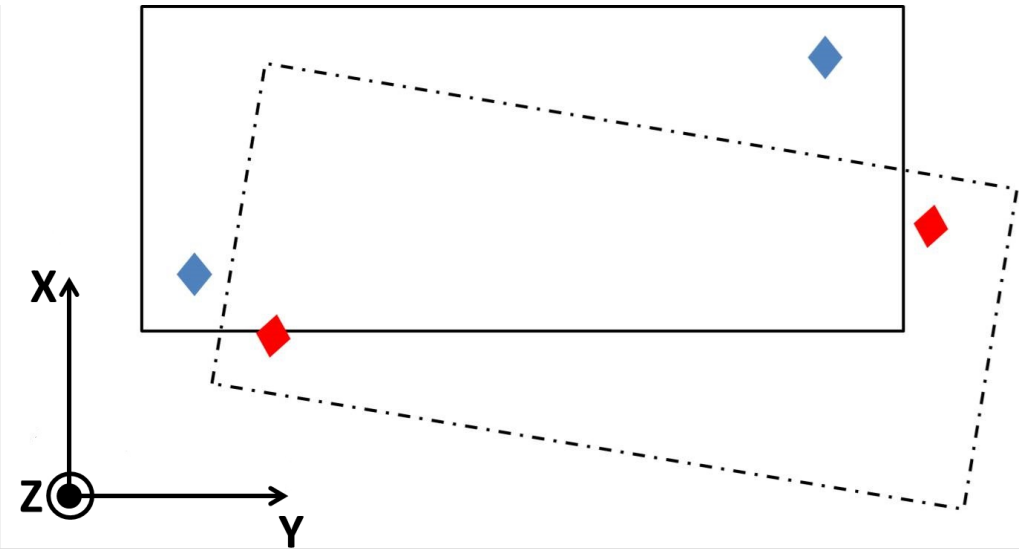

Figure 13: Potential misalignment of two surface topography measurements

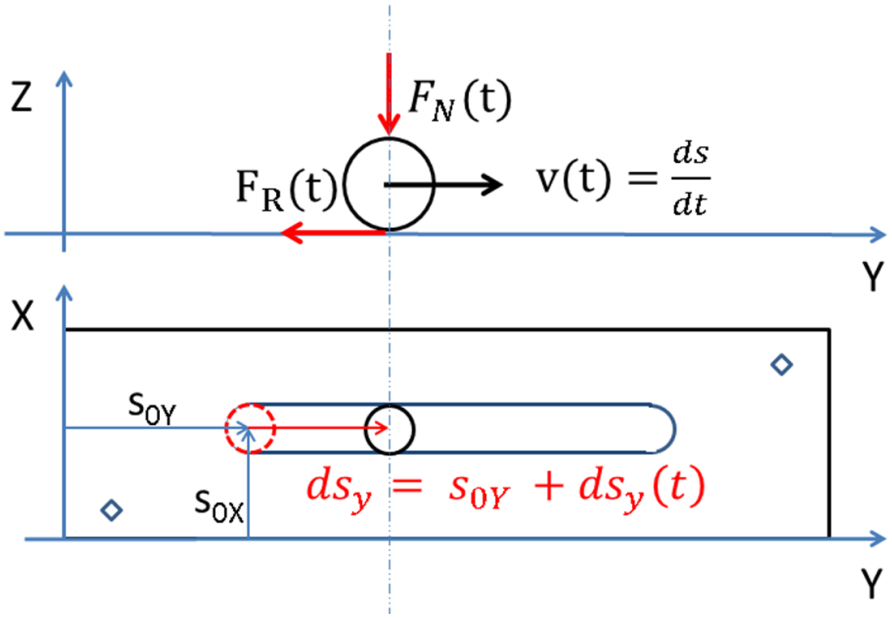

Figure 14: Calcution scheme for the calcuation of the SDFP

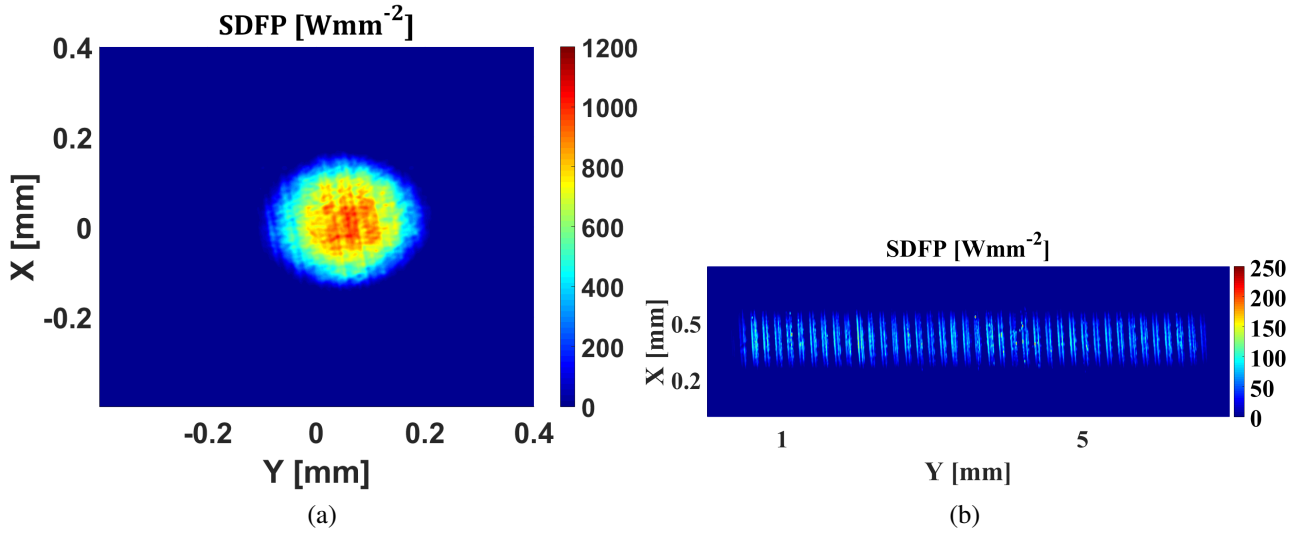

Figure 15: Example of calculated SDFP over one half wear test cycle; (a) counter body, (b) base body

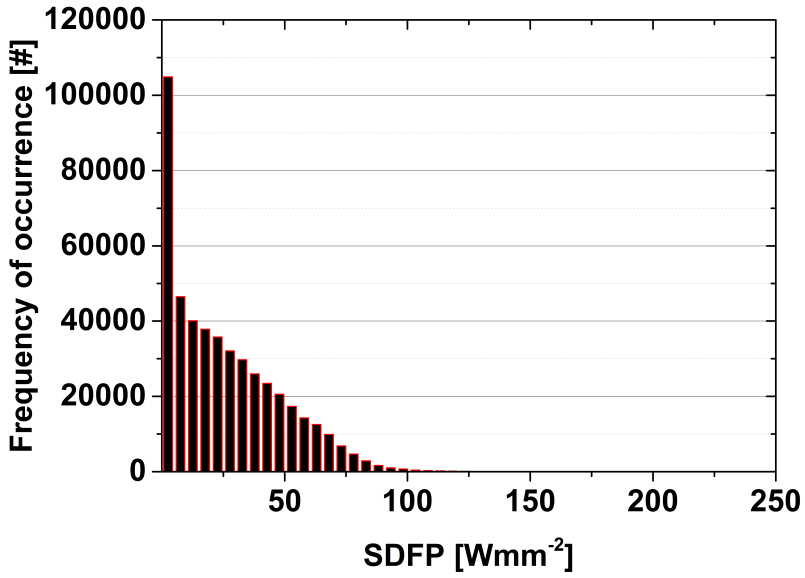

Figure 16: Histogram representation of SDFP (base body) seen in Fig 15 (b)

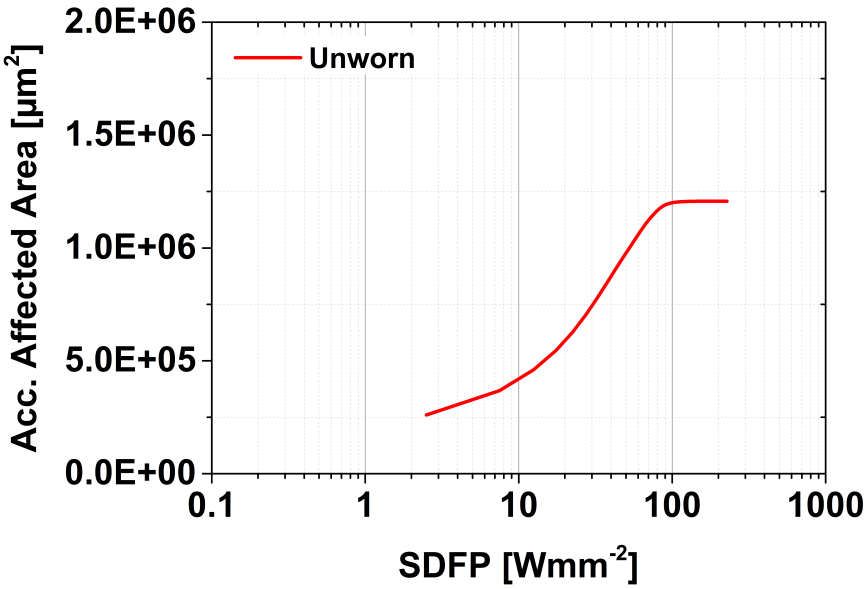

Figure 17: Accumulated affected area vs. SDFP

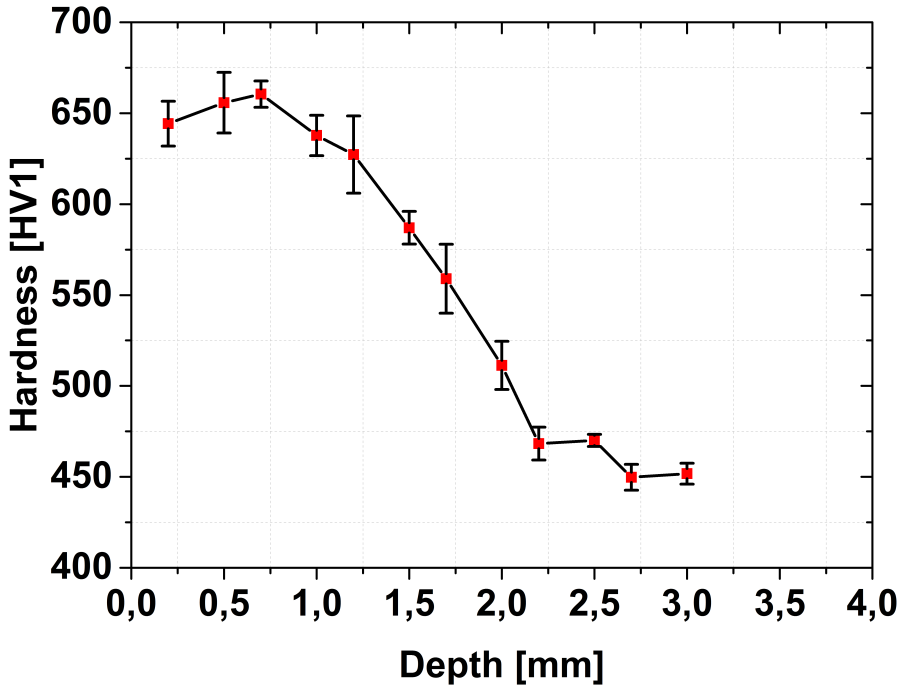

Figure 18: Hardness profile of carburized 18CrNiMo7-6

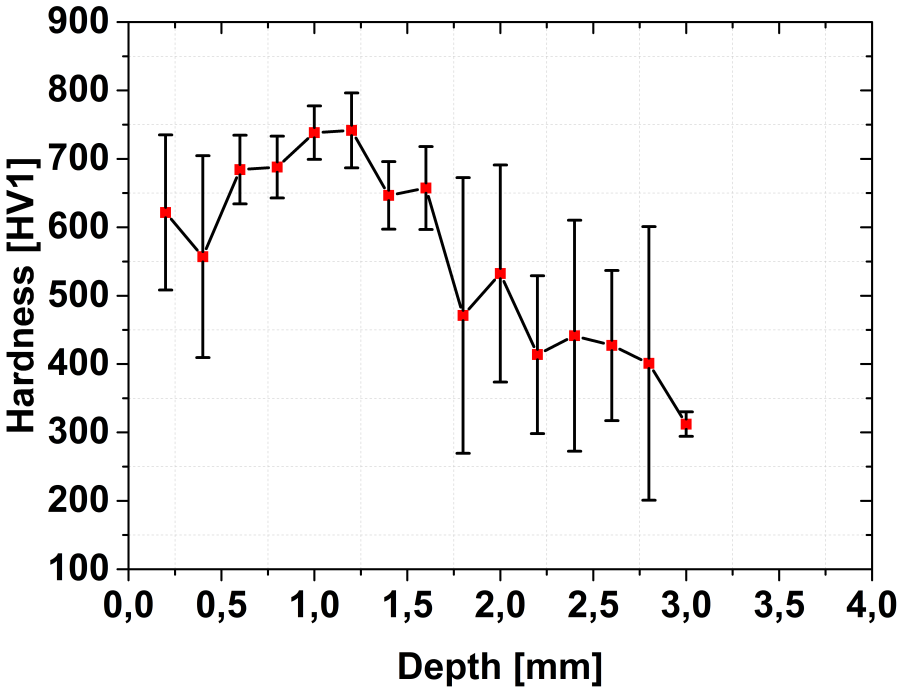

Figure 19: Hardness profile of case hardened EN-GJS-HB 265

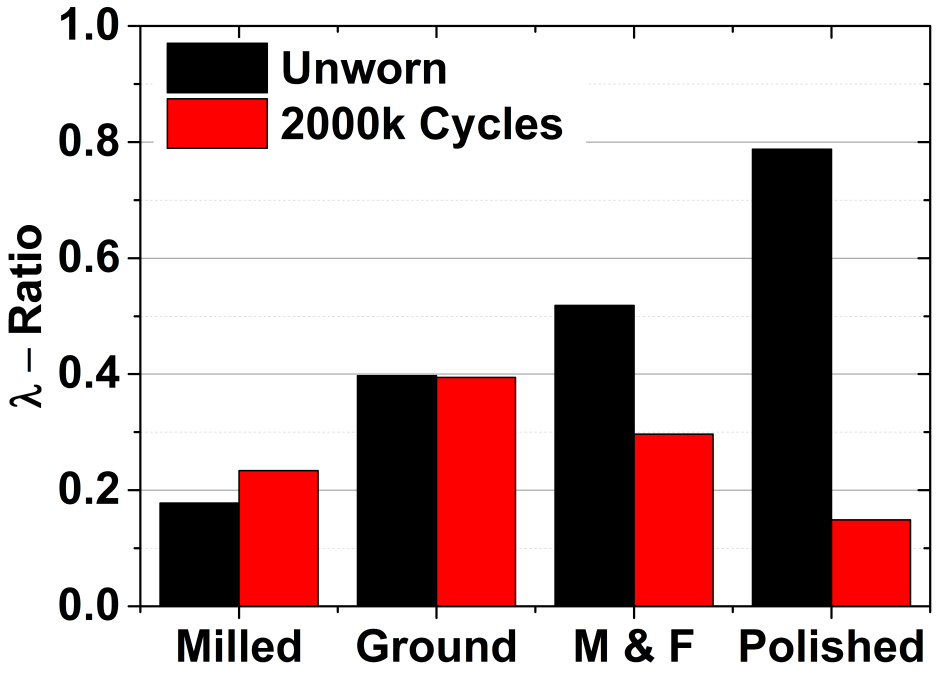

Figure 20: Tallian Parameter; 18CrNiMo7-6 wear tests

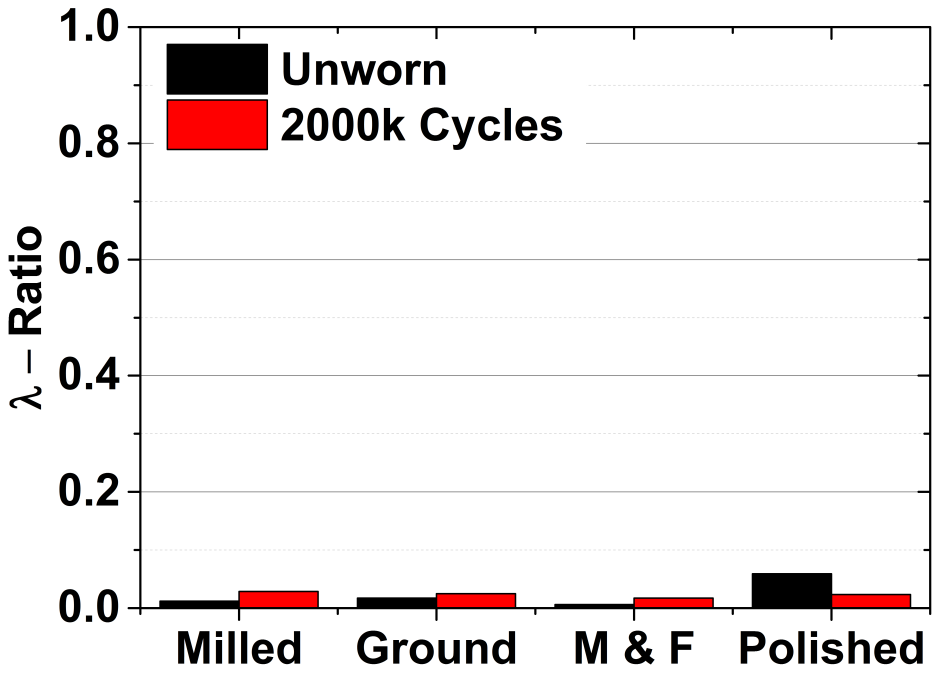

Figure 21: Tallian Parameter; EN-GJS-HB 265 wear tests

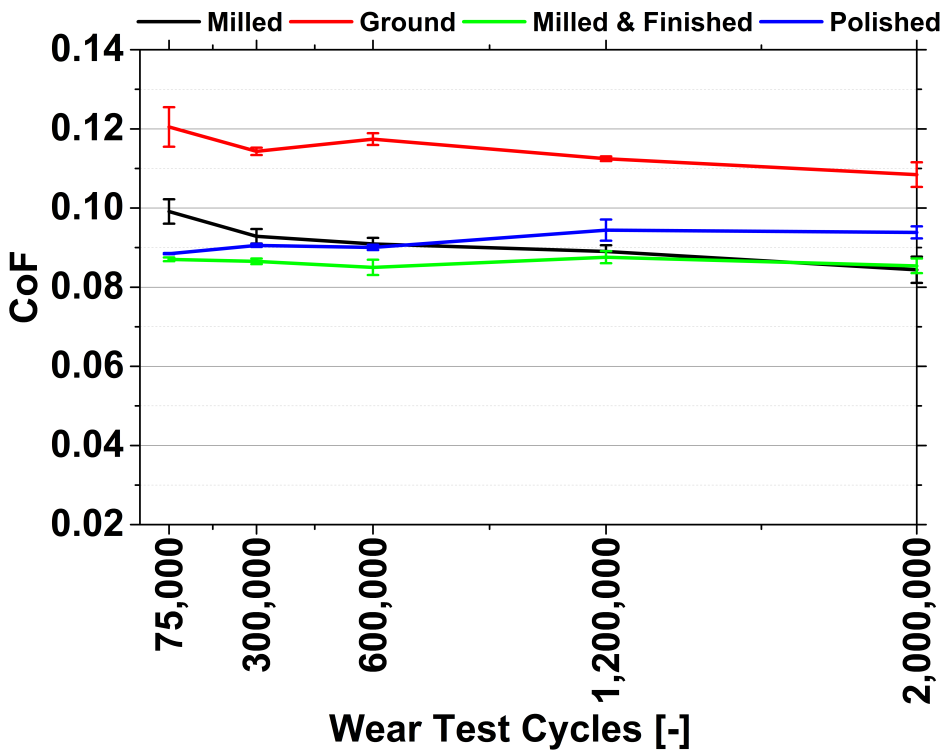

Figure 22: Mean value of coefficient of friction over wear test cycles; 18CrNiMo7-6

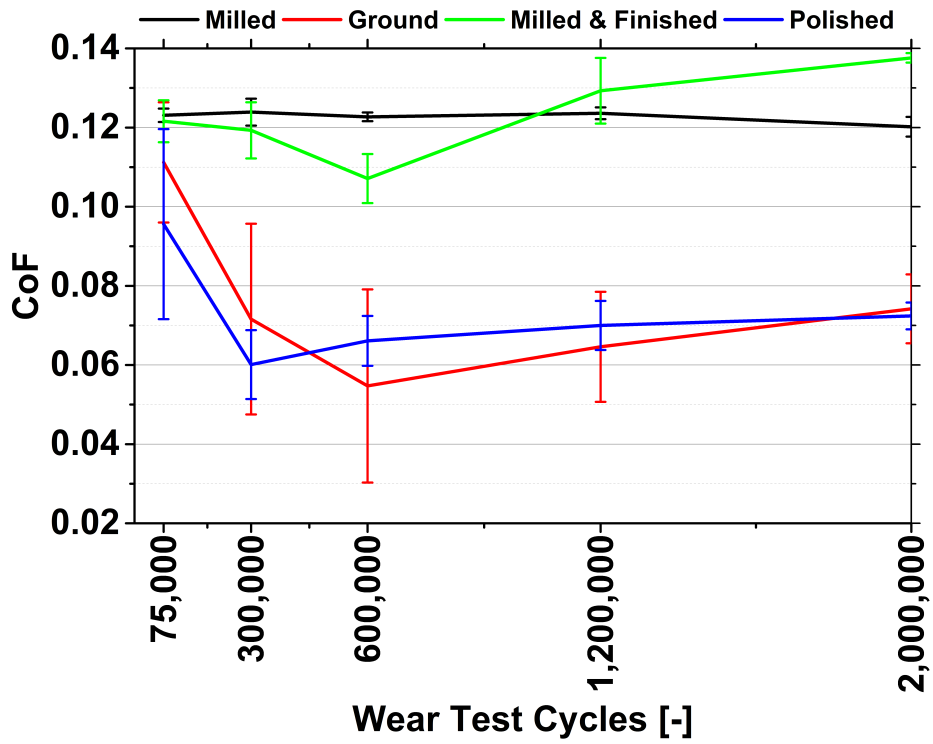

Figure 23: Mean value of coefficient of friction over wear test cycles; EN-GJS-HB 265

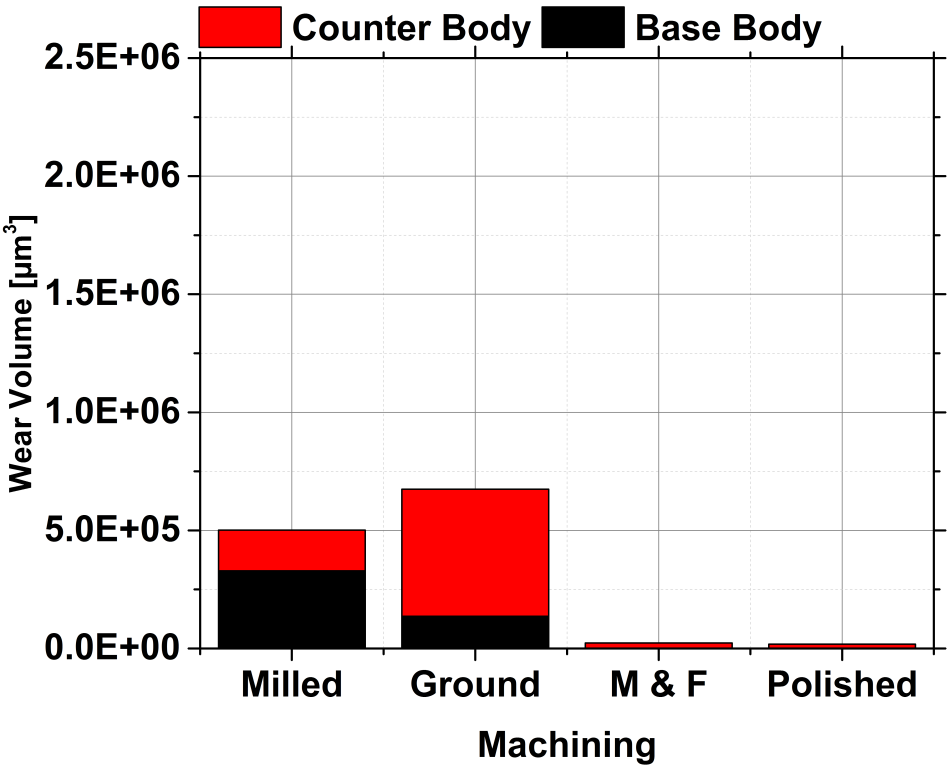

Figure 24: Wear Volume after 2M wear test cycles; 18CrNiMo7-6

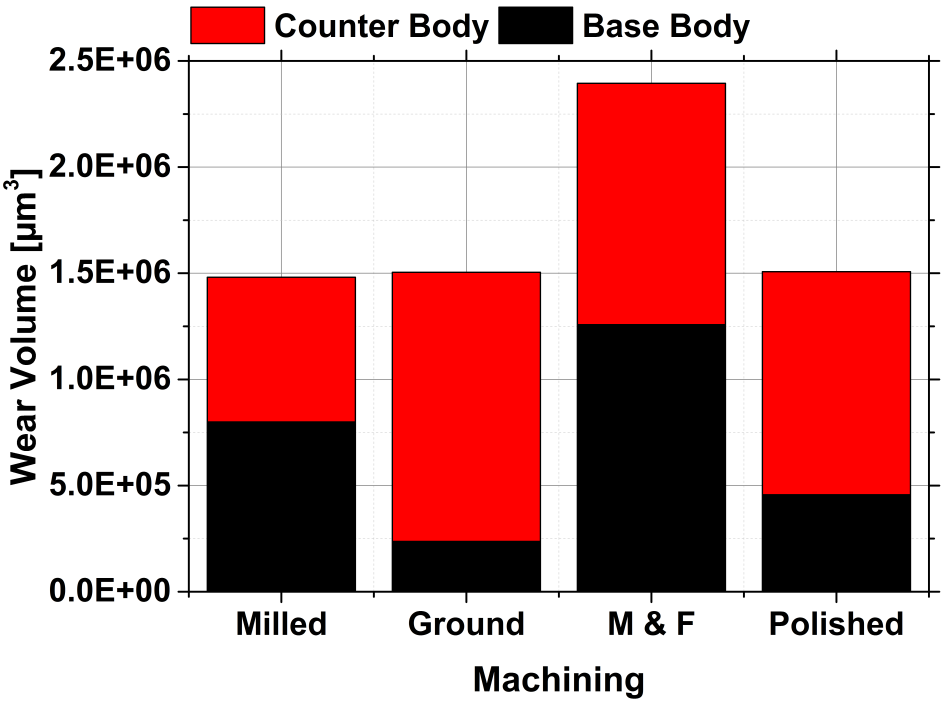

Figure 25: Wear Volume after 2M wear test cycles; EN-GJS-HB 265

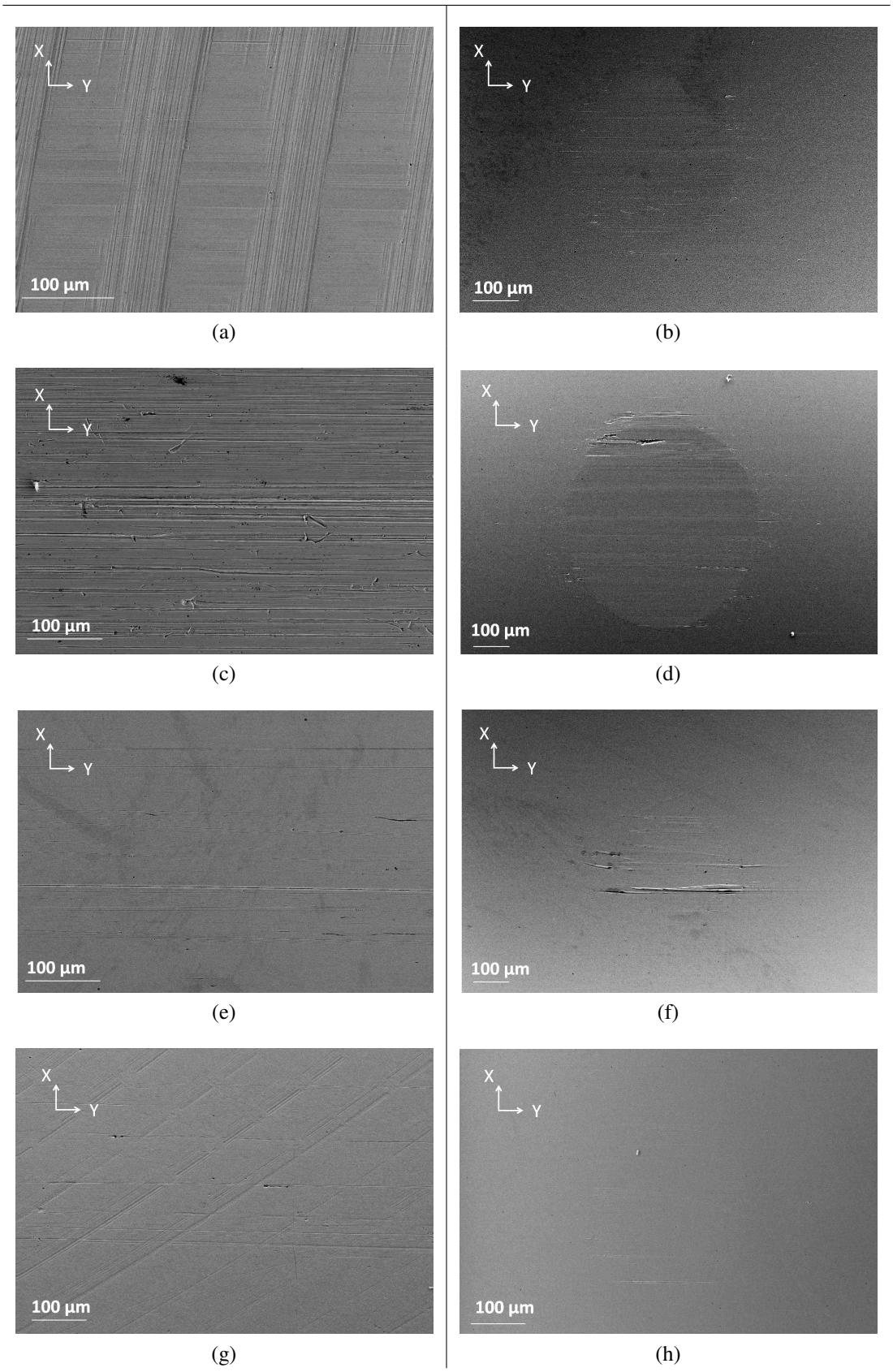

Figure 26: Wear appearances after 2M wear test cycles; 18CrNiMo7-6 ((a&b) Milled, (c&d) Ground, (e&f) Polished and (g&h) M&F)

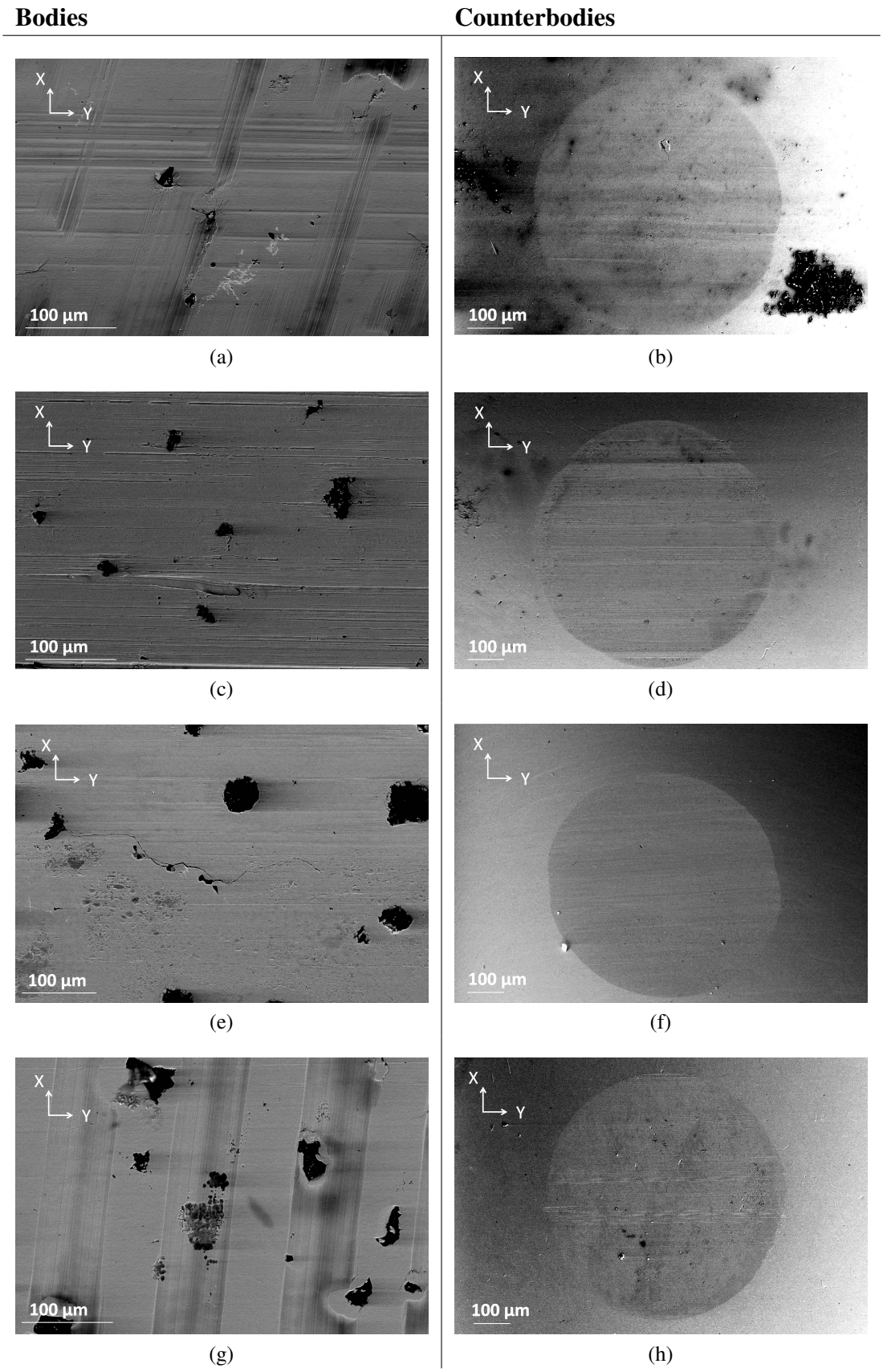

Figure 27: Wear appearances after 2M wear test cycles; EN-GJS-HB 265 ((a&b) Milled, (c&d) Ground, (e&f) Polished and (g&h) M&F)

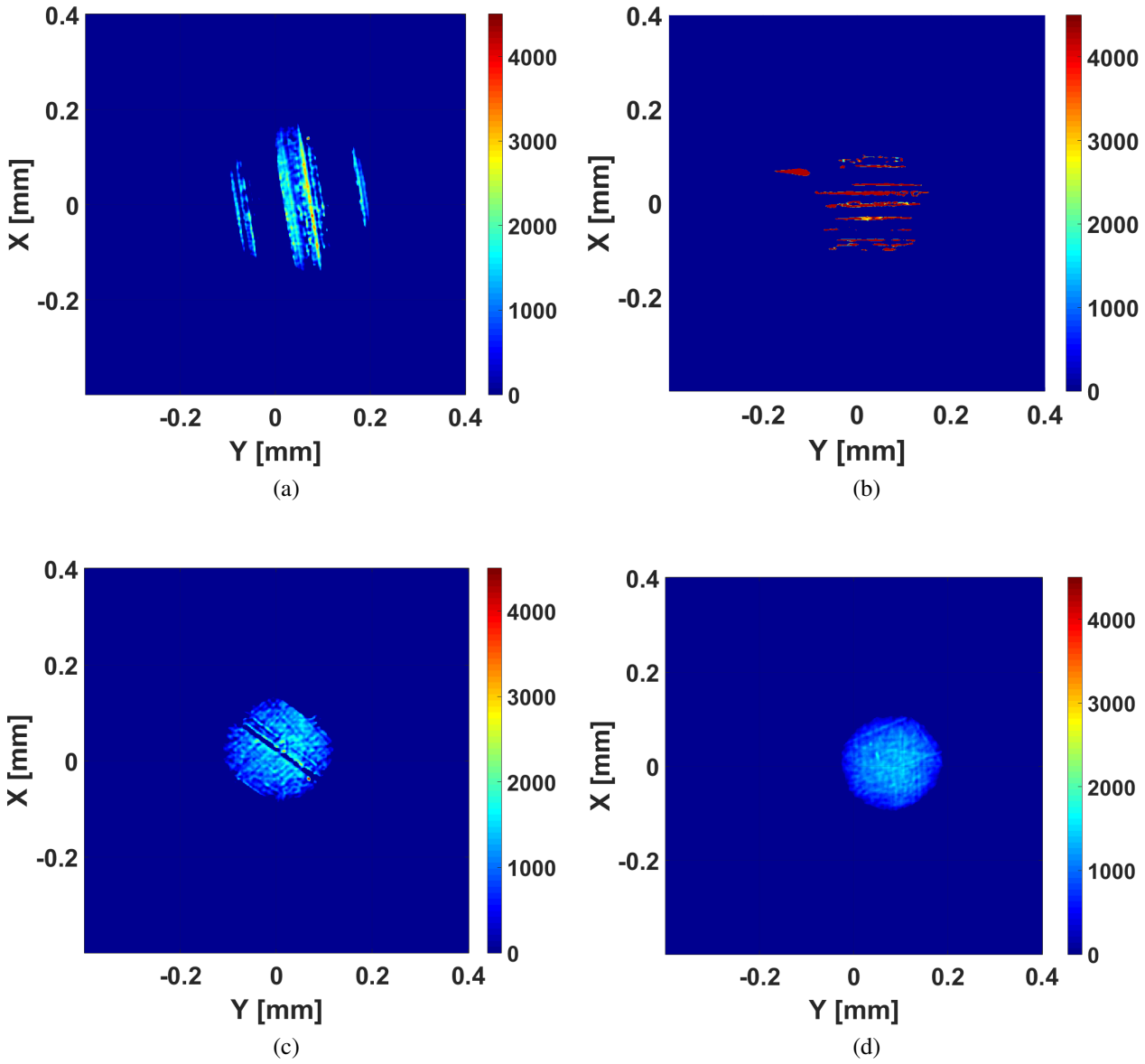

Figure 28: Calculated pressure distribution p(x,y) [MPa]; CS wear test series
(a) milled, (b) ground, (c) milled & finished, (d) polished

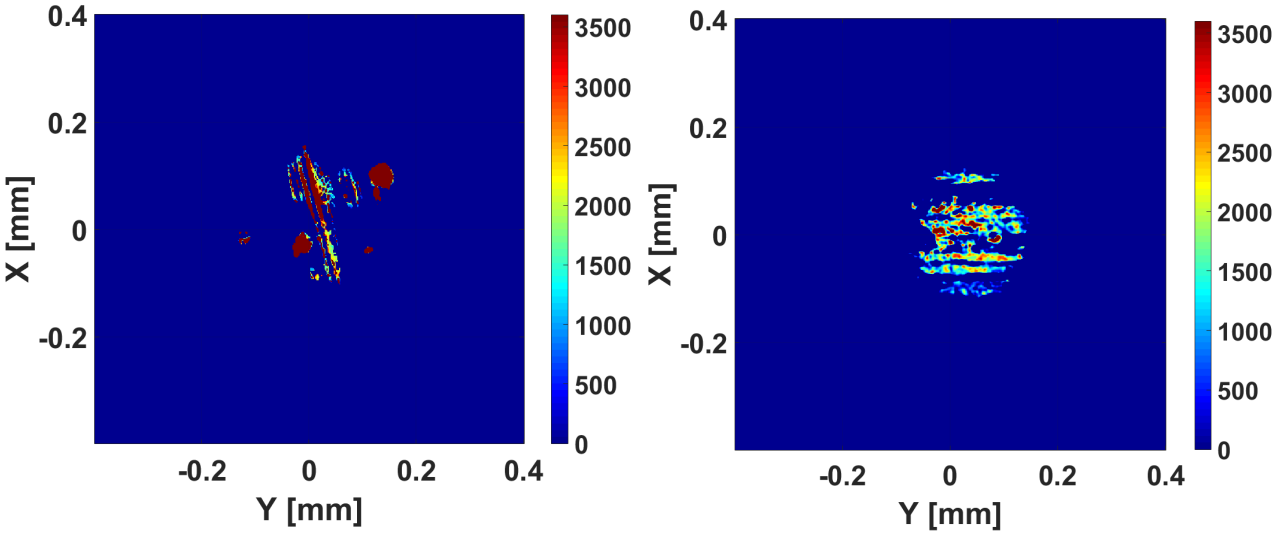

(a)

(b)

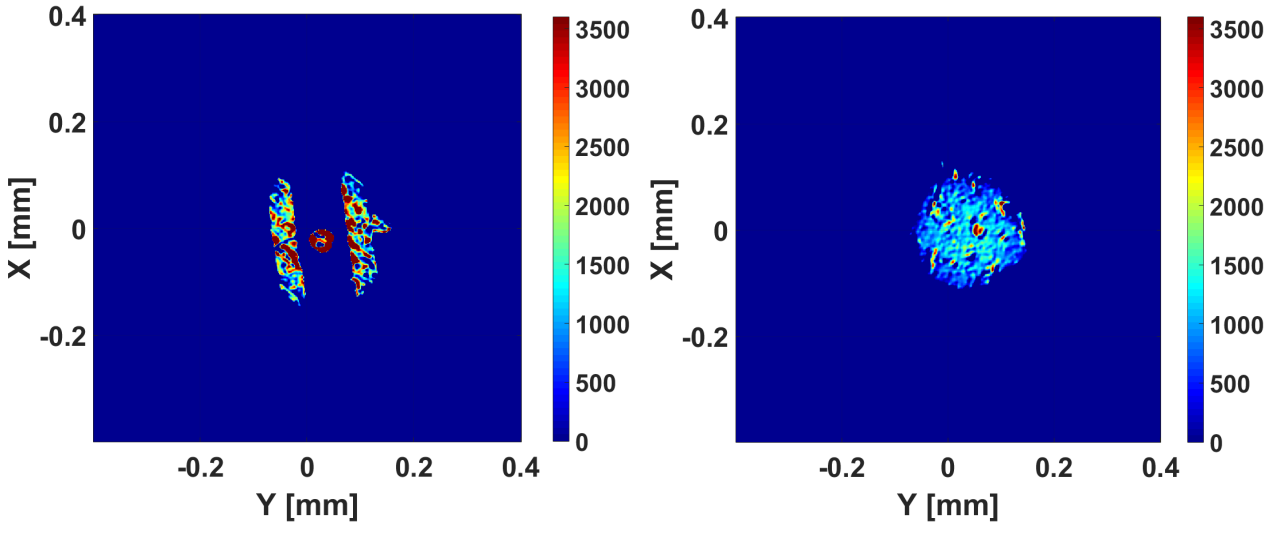

(c)

(d)

Figure 29: Calculated pressure distribution p(x,y) [MPa]; CHI wear test series
(a) milled, (b) ground, (c) polished, (d) milled & finished

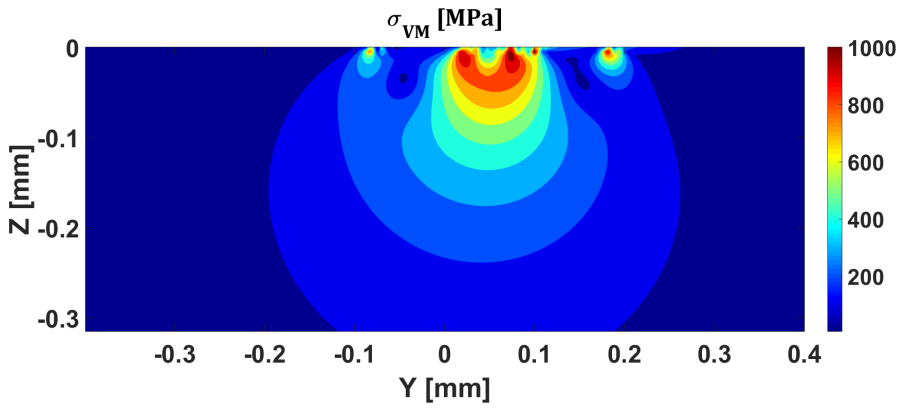

(a)

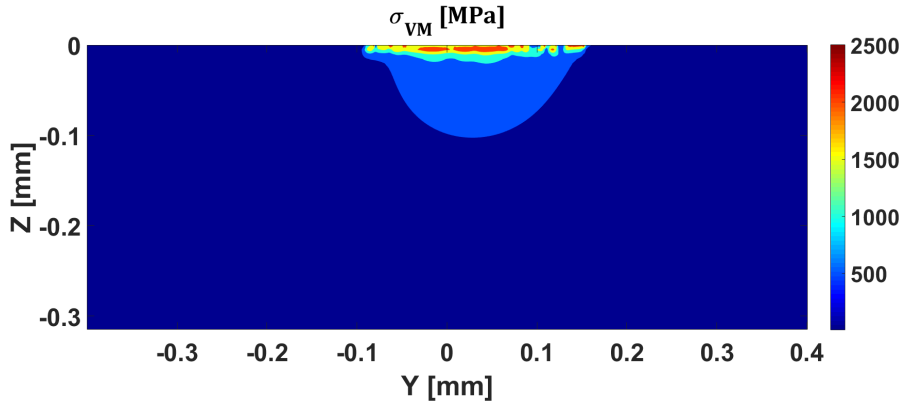

(b)

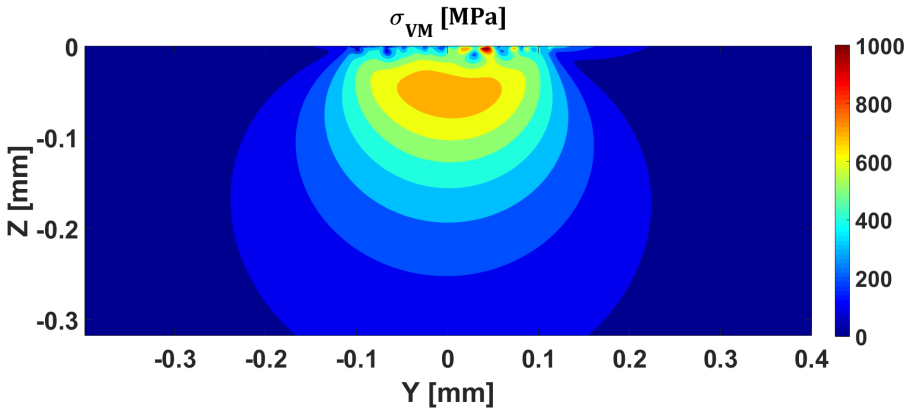

(c)

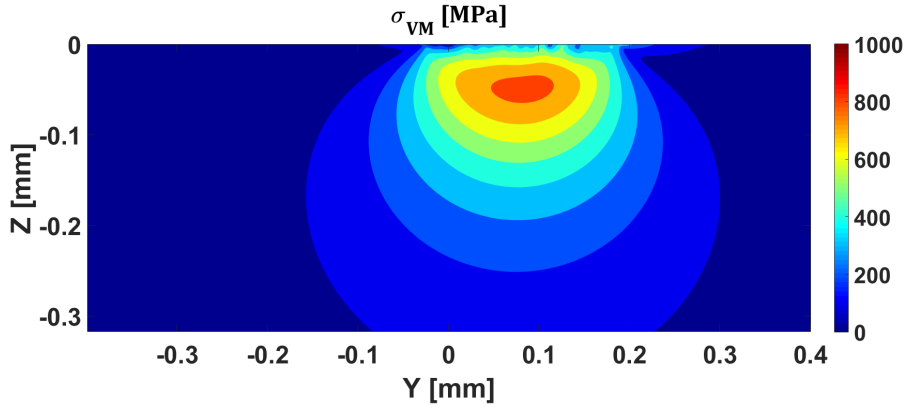

(d)

Figure 30: Calculated contact stresses σ_{VM} [MPa]; CS wear test series
(a) milled ($\mu = 0,11$), (b) ground ($\mu = 0,124$), (c) milled & finished ($\mu = 0,086$), (d) polished ($\mu = 0,081$)

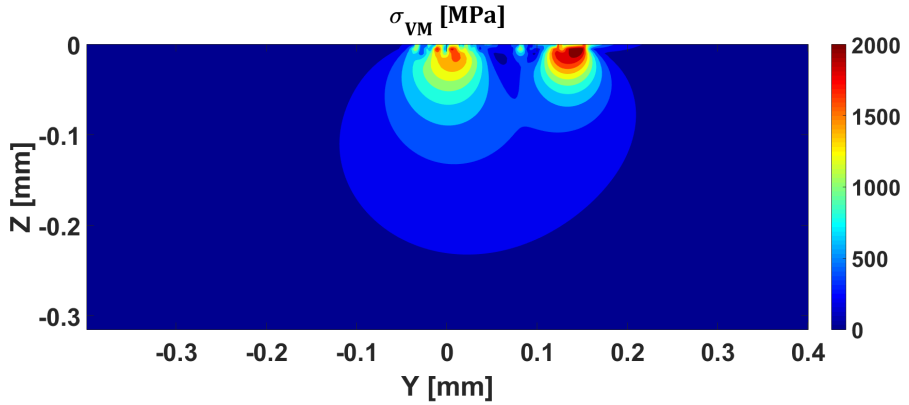

(a)

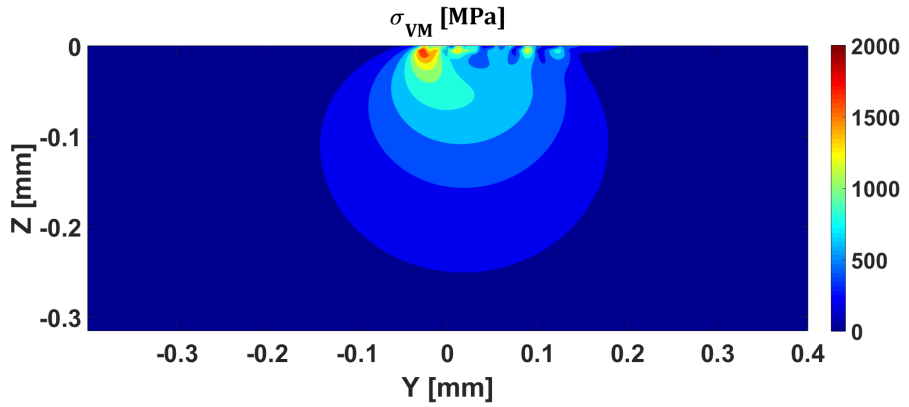

(b)

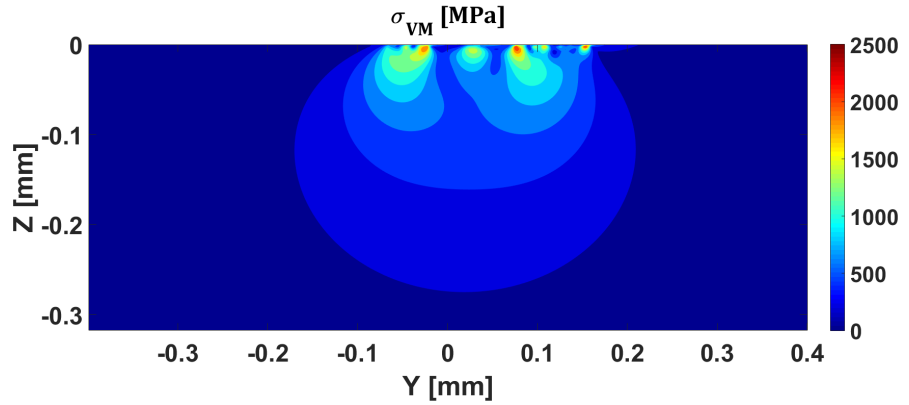

(c)

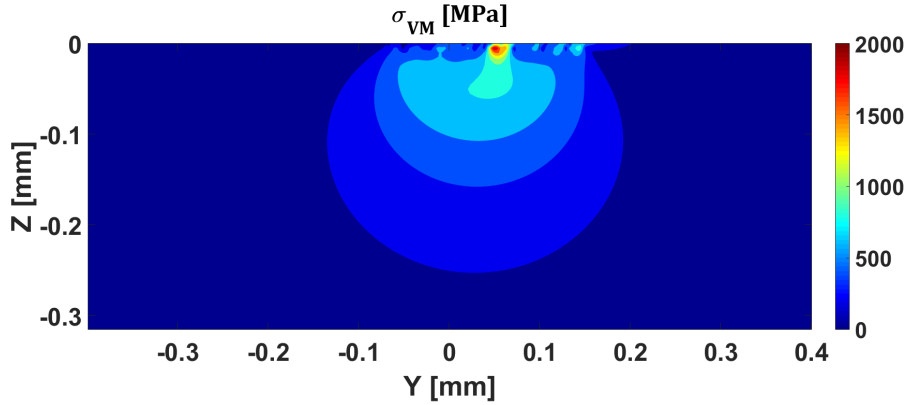

(d)

Figure 31: Calculated contact stresses σ_{VM} [MPa]; CHI wear test series
(a) milled ($\mu = 0,12$), (b) ground ($\mu = 0,11$), (c) milled & finished ($\mu = 0,127$), (d) polished ($\mu = 0,096$)

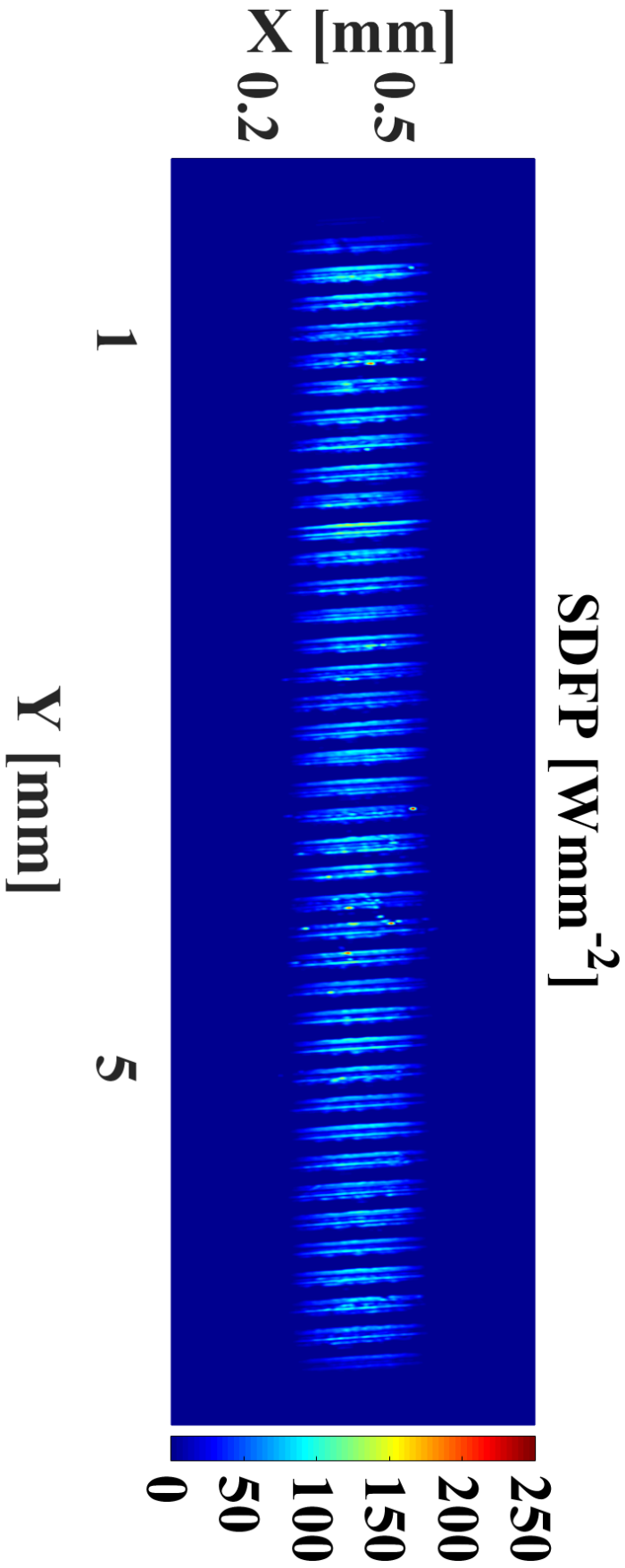

Figure 32: Distribution of the SDFP (base body), first half cycle; Milled surface topography; CS wear test series

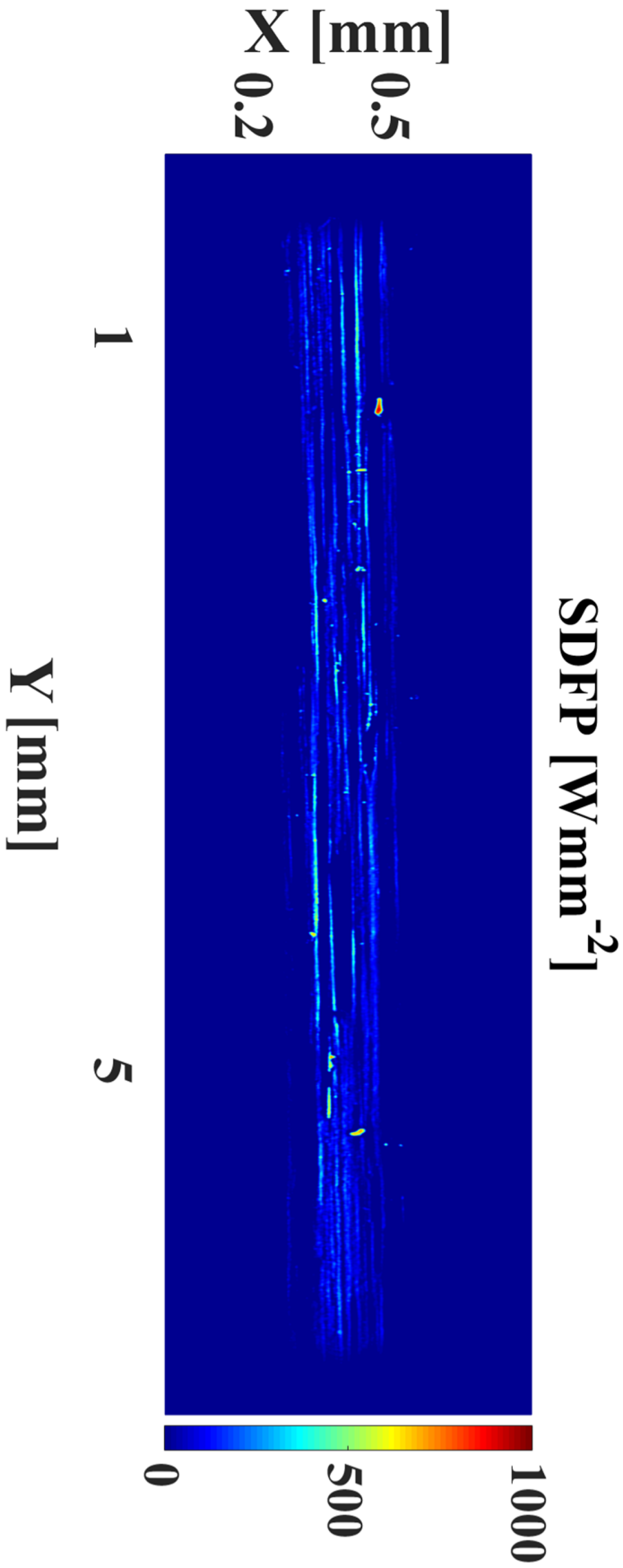

Figure 33: Distribution of the SDFP (base body), first half cycle; Ground surface topography; CS wear test series

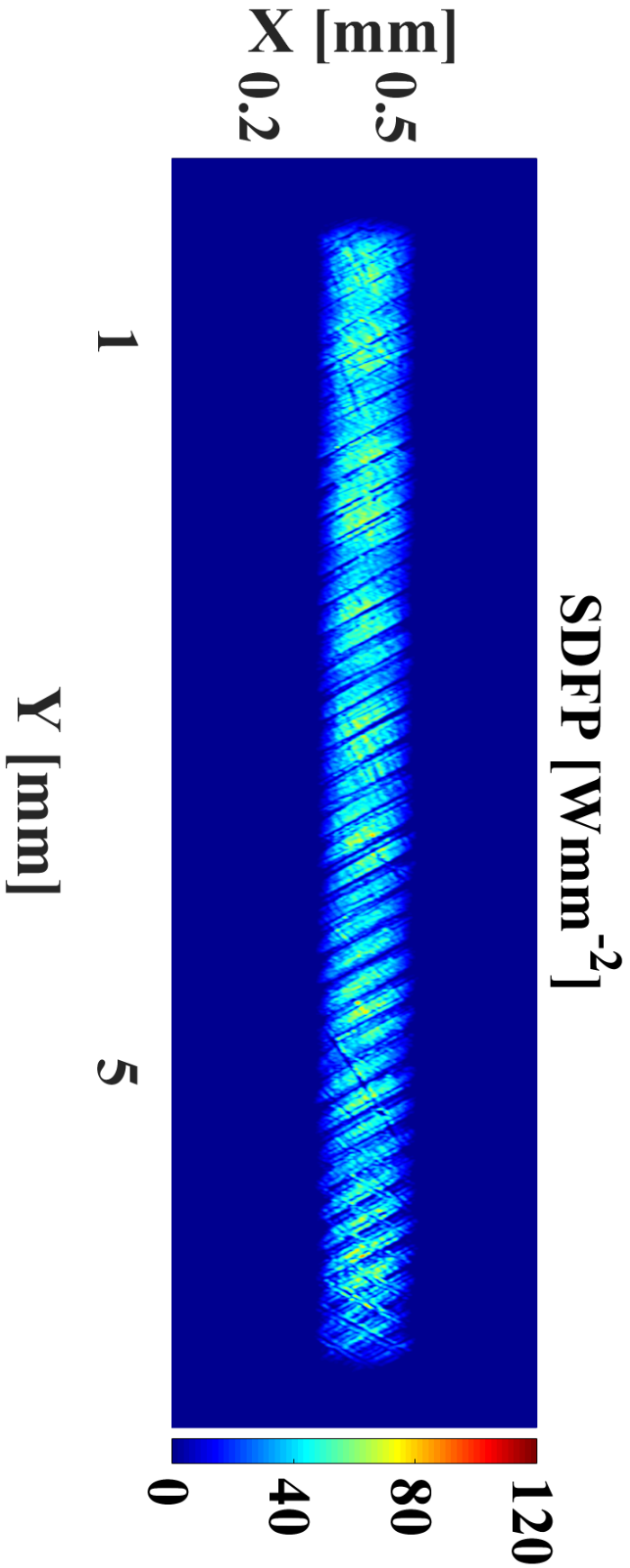

Figure 34: Distribution of the SDFP (base body), first half cycle; Milled & finished surface topography; CS wear test series

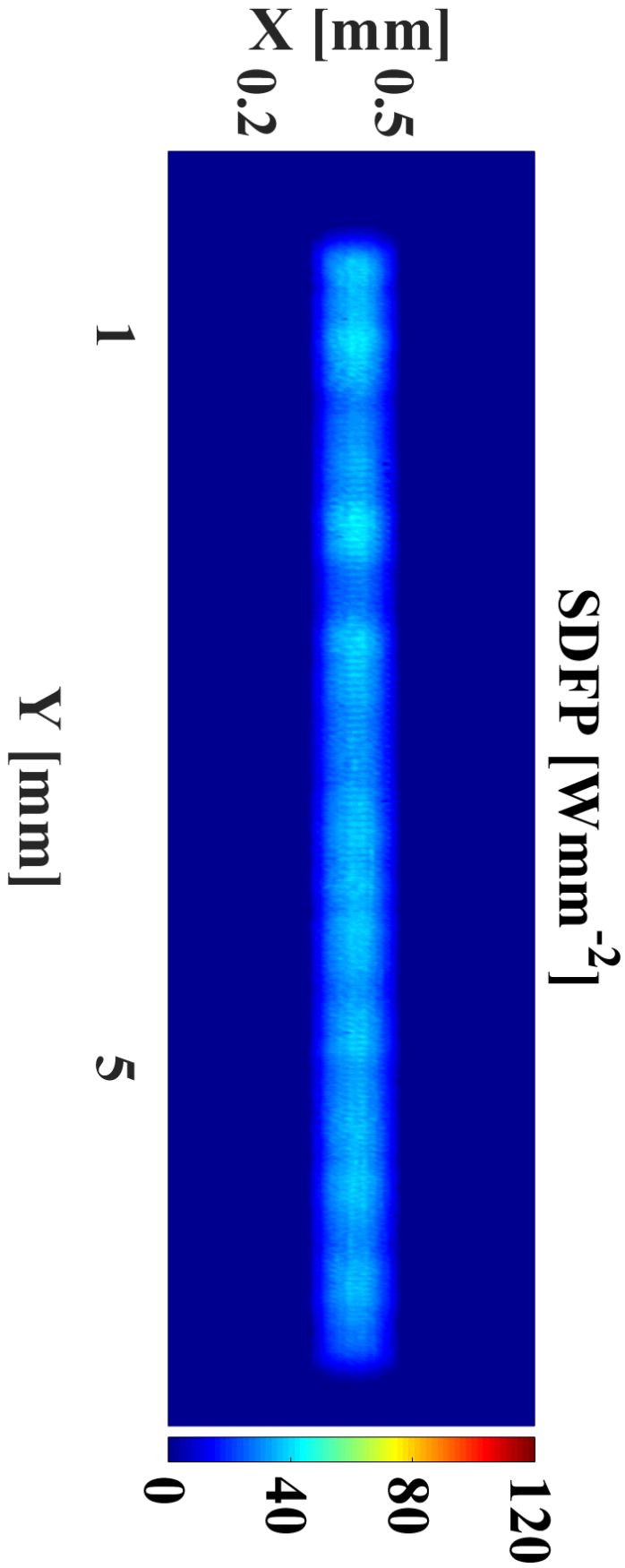

Figure 35: Distribution of the SDFP (base body), first half cycle; Polished surface topography; CS wear test series

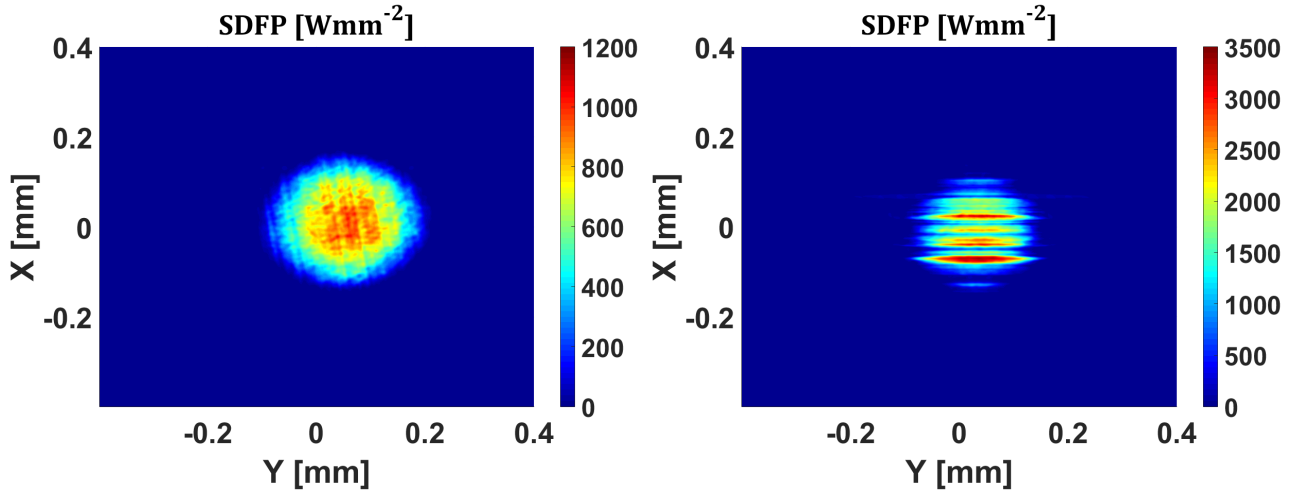

(a) (b)

Figure 36: Distribution of the SDFP (counter body), first half cycle; CS wear test series
(a) milled, (b) ground

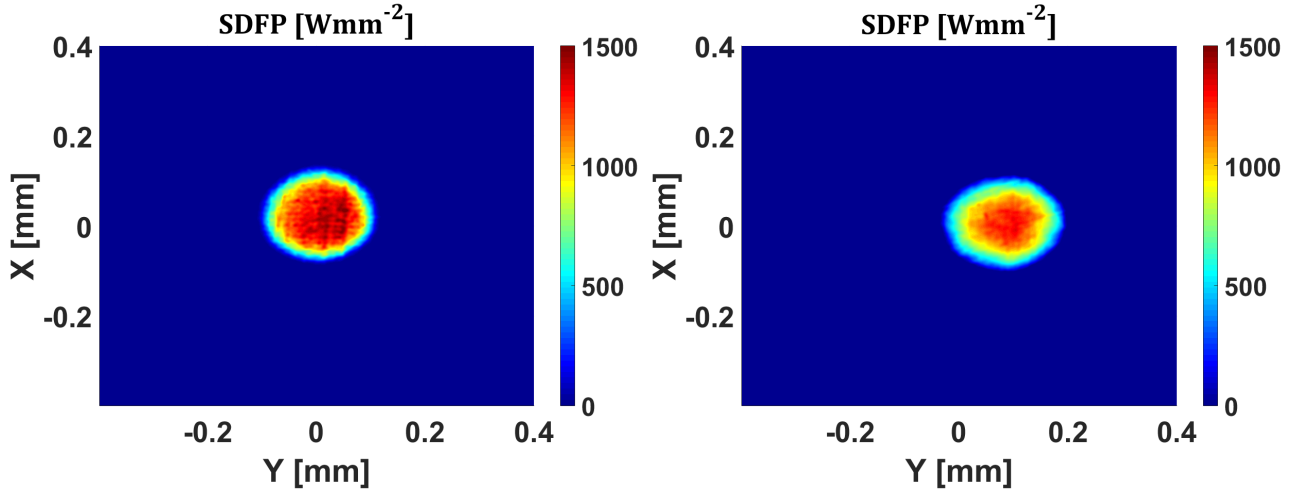

(a) (b)

Figure 37: Distribution of the SDFP (counter body), first half cycle; CS wear test series
(a) M&F, (b) polished

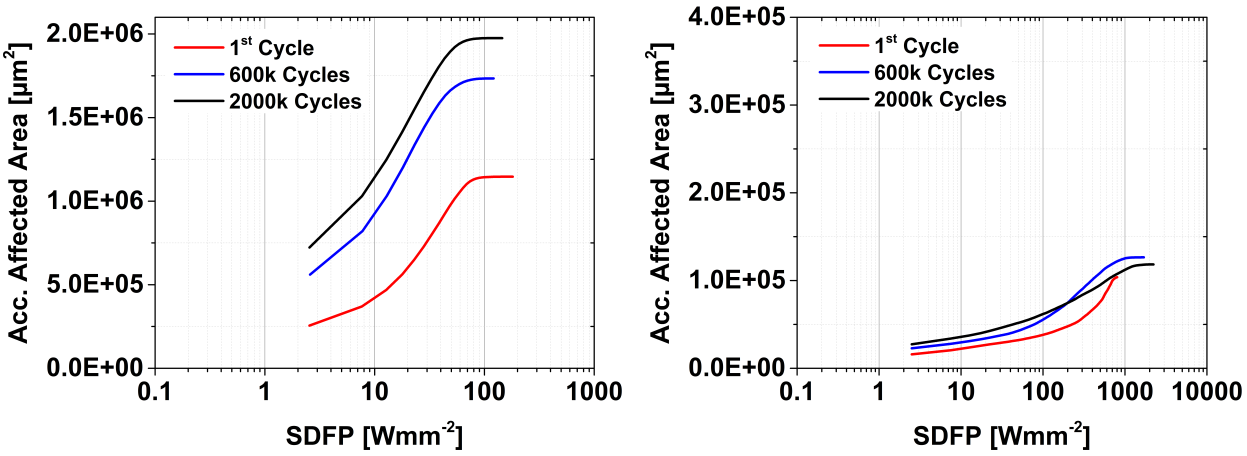

Figure 38: SDFP vs. acc. A_{Aff} of milled surface topography, CS wear test series; (a) base body, (b) counter body

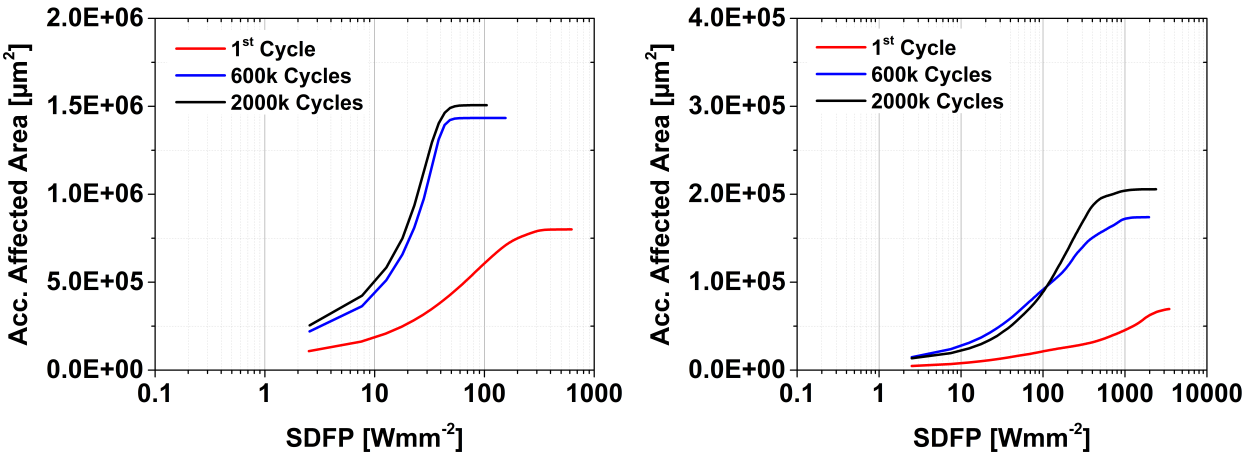

Figure 39: SDFP vs. acc. A_{Aff} of ground surface topography, CS wear test series; (a) base body, (b) counter body

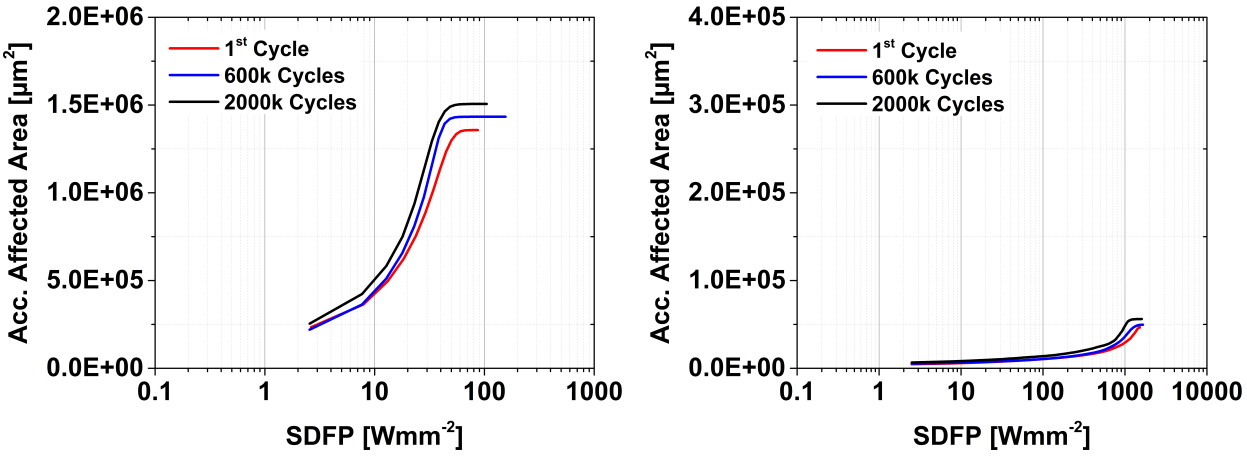

(a) (b)

Figure 40: SDFP vs. acc. A_{Aff} of M&F surface topography, CS wear test series; (a) base body, (b) counter body

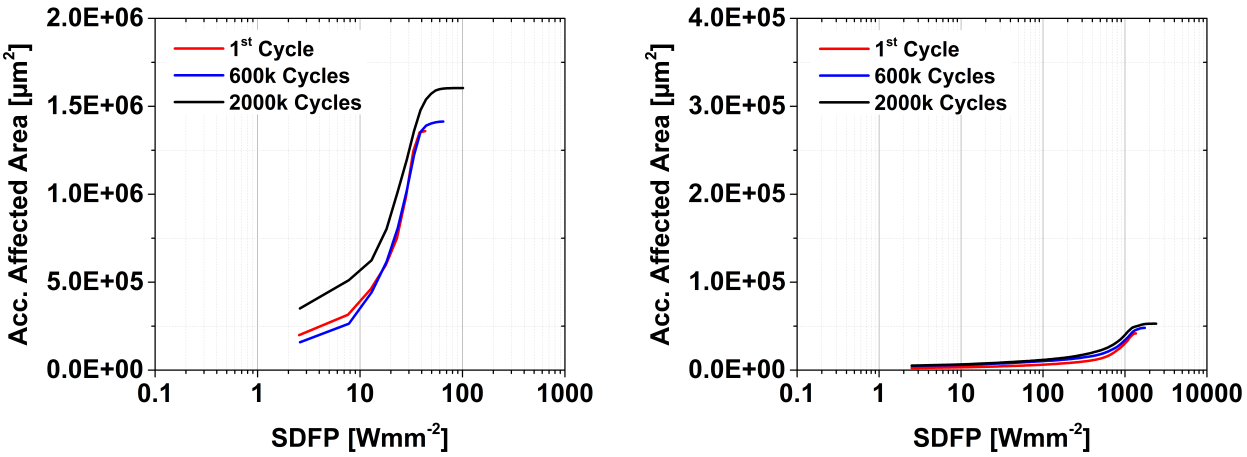

(a) (b)

Figure 41: SDFP vs. acc. A_{Aff} of polished surface topography, CS wear test series; (a) base body, (b) counter body

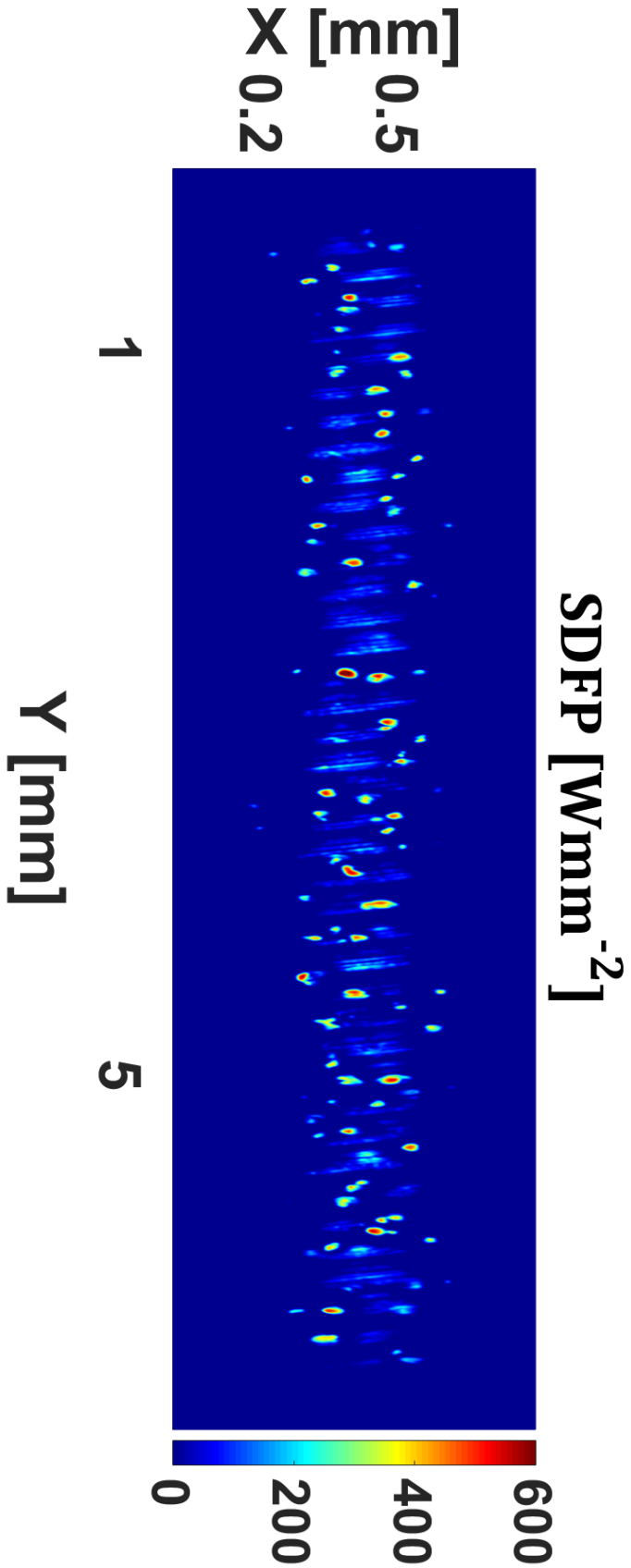

Figure 42: Distribution of the SDFP (base body), first half cycle; Milled surface topography; CHI wear test series

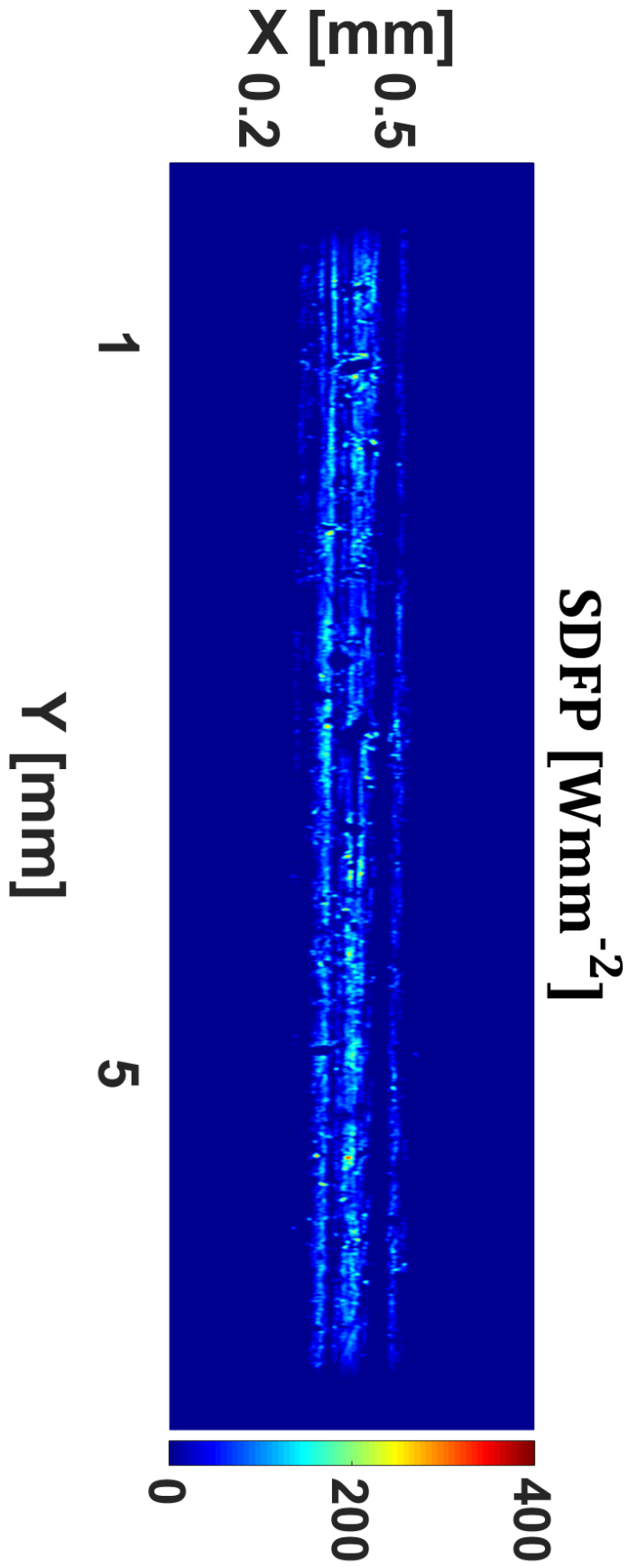

Figure 43: Distribution of the SDFP (base body), first half cycle; Ground surface topography; CHI wear test series

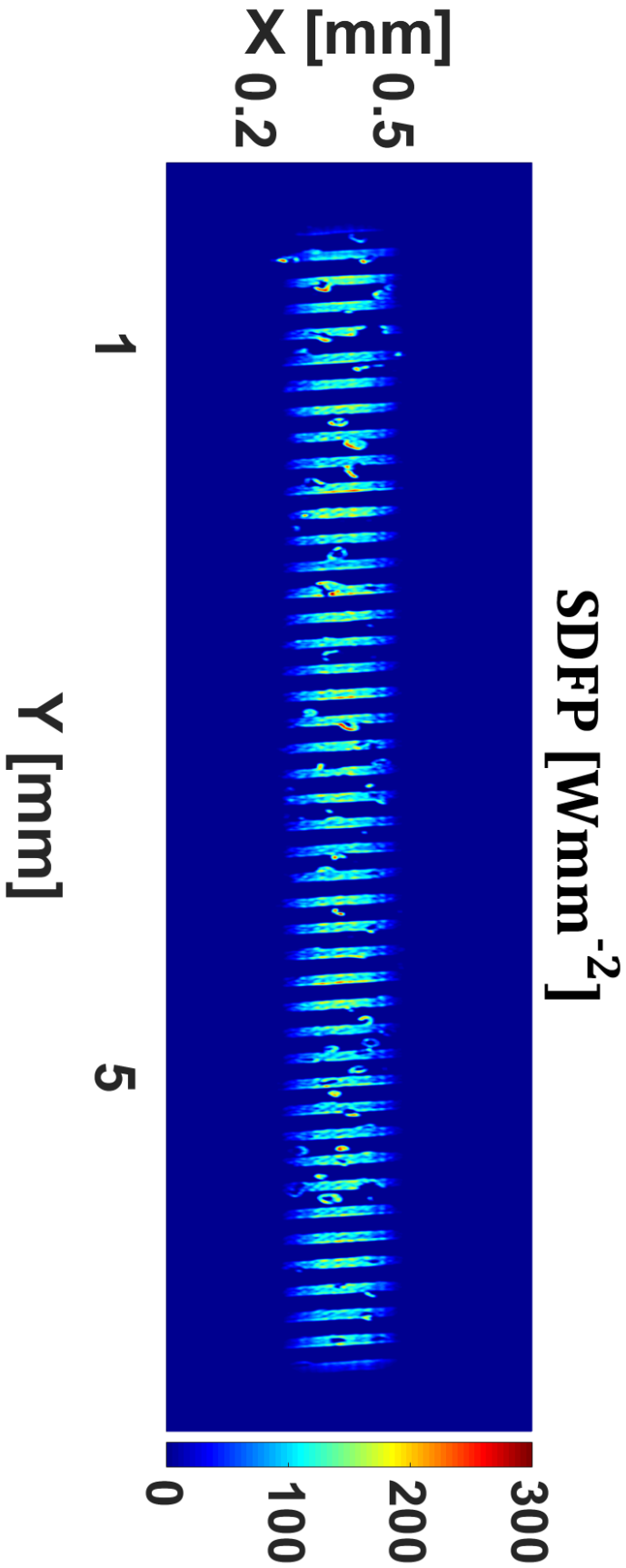

Figure 44: Distribution of the SDFP (base body), first half cycle; M&F surface topography; CHI wear test series

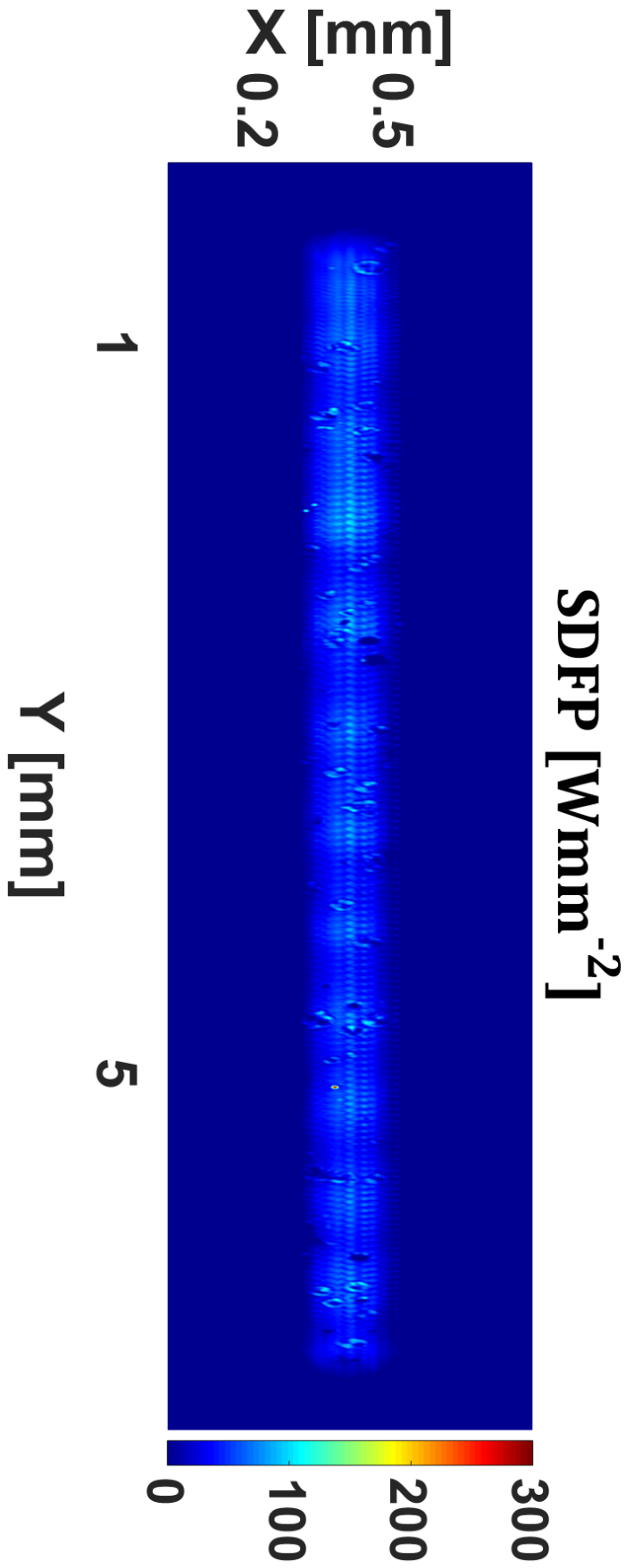

Figure 45: Distribution of the SDFP (base body), first half cycle; Polished surface topography; CHI wear test series

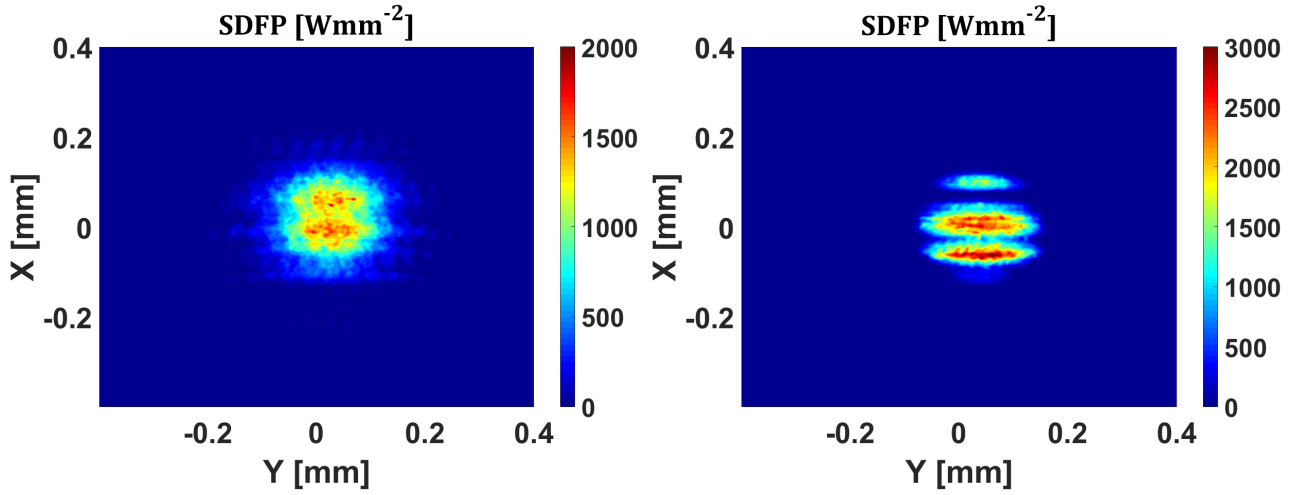

(a) (b)

Figure 46: Distribution of the SDFP (counter body), first half cycle; CHI wear test series
(a) milled, (b) ground

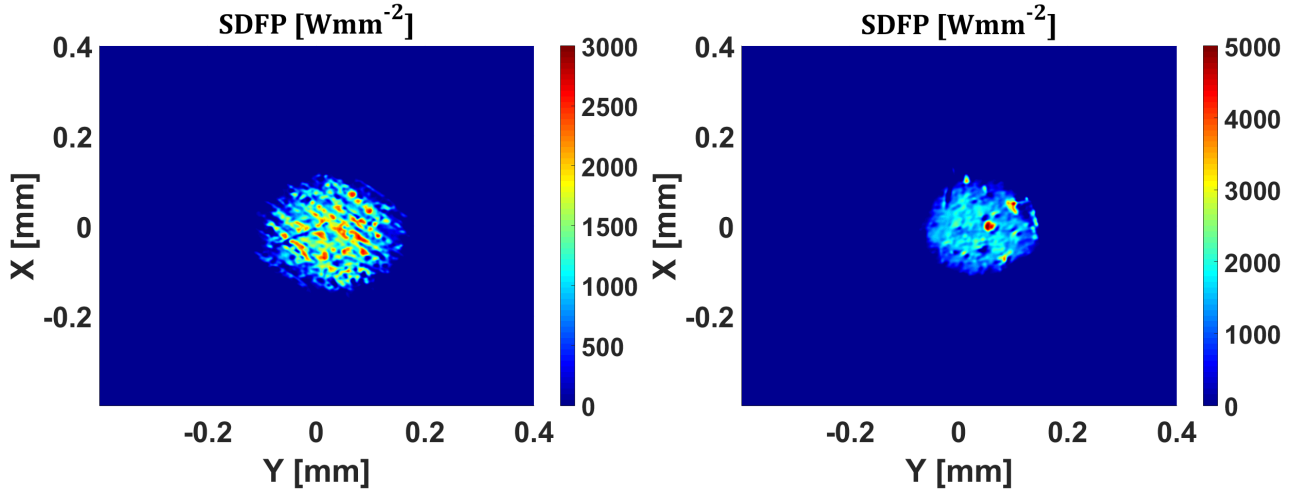

(a) (b)

Figure 47: Distribution of the SDFP (counter body), first half cycle; CHI wear test series
(a) M&F, (b) polished

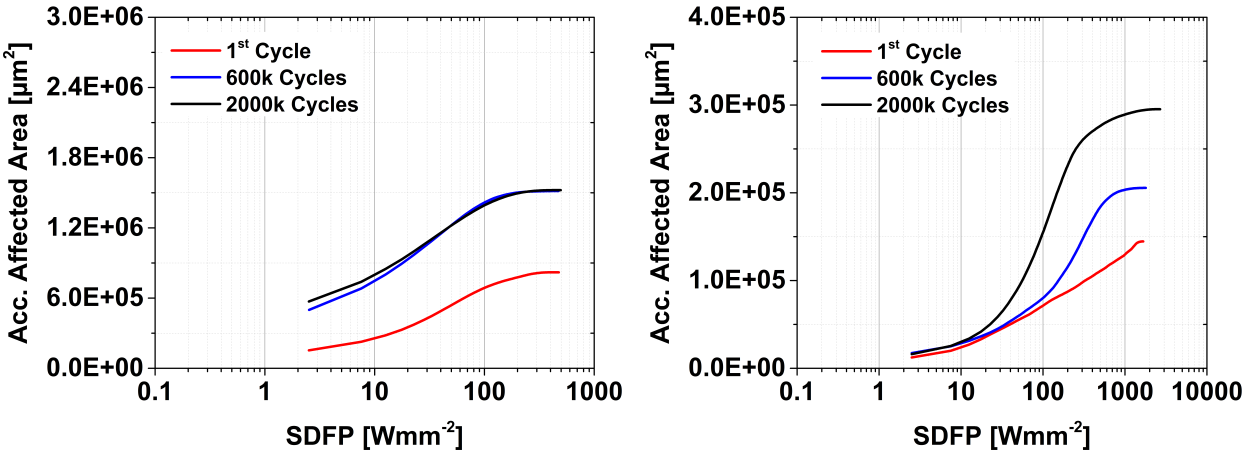

(a) (b)

Figure 48: SDFP vs. acc. A_{Aff} of milled surface topography, CHI wear test series; (a) base body, (b) counter body

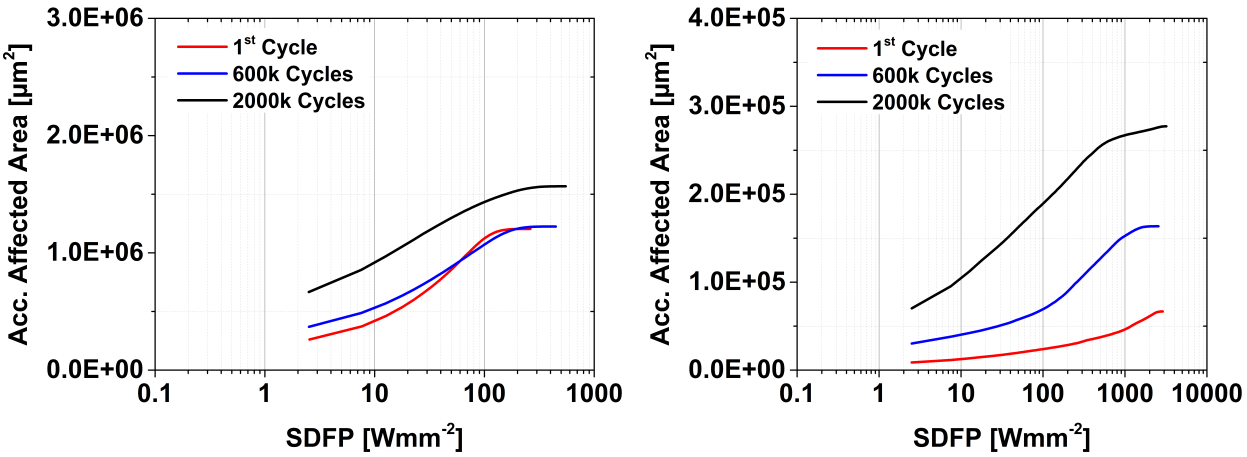

(a) (b)

Figure 49: SDFP vs. acc. A_{Aff} of ground surface topography, CHI wear test series; (a) base body, (b) counter body

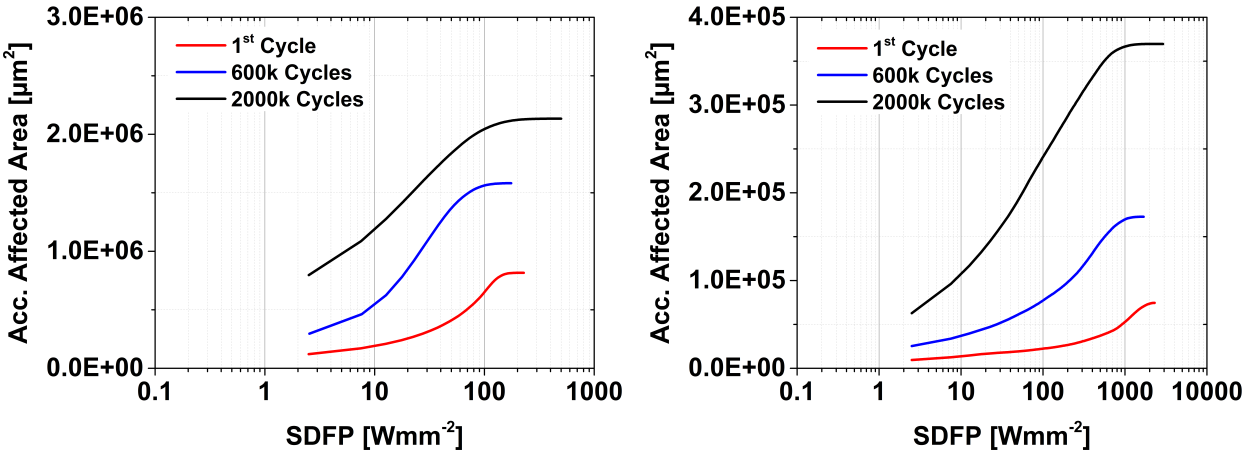

(a) (b)

Figure 50: SDFP vs. acc. A_{Aff} of M&F surface topography, CHI wear test series; (a) base body, (b) counter body

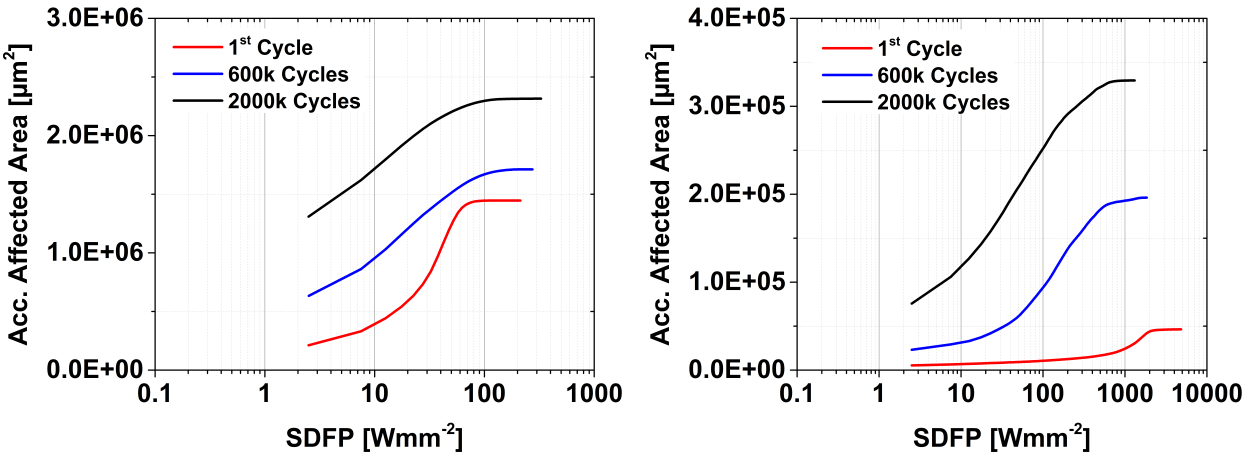

(a) (b)

Figure 51: SDFP vs. acc. A_{Aff} of polished surface topography, CHI wear test series; (a) base body, (b) counter body

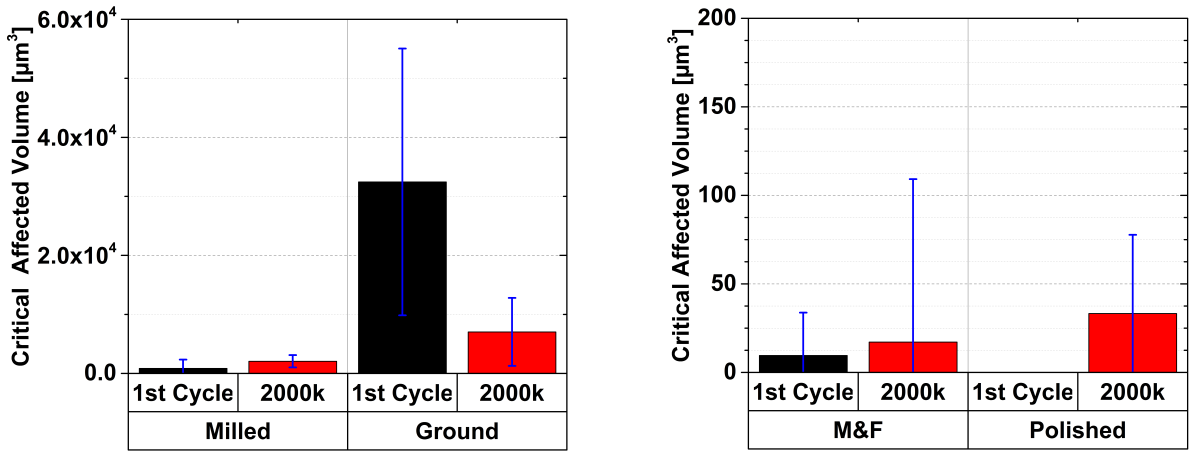

(a) (b)

Figure 52: Critically affected volume ($d \geq 1$) over one half cycle of the wear test; CS wear test series

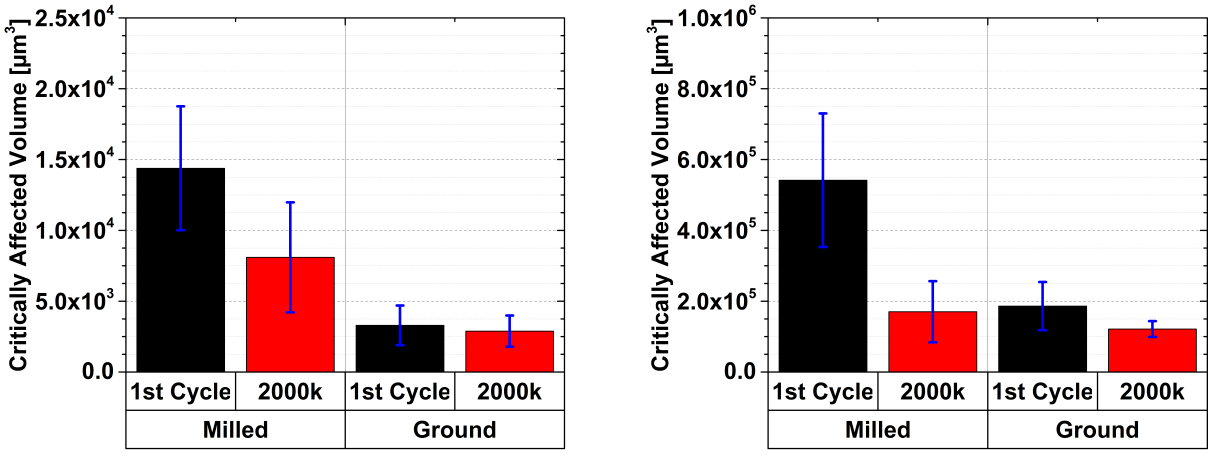

(a) (b)

Figure 53: Critically affected volume ($d \geq 1$) over one half cycle of the wear test; CHI wear test series, (a) base body, (b) counter body

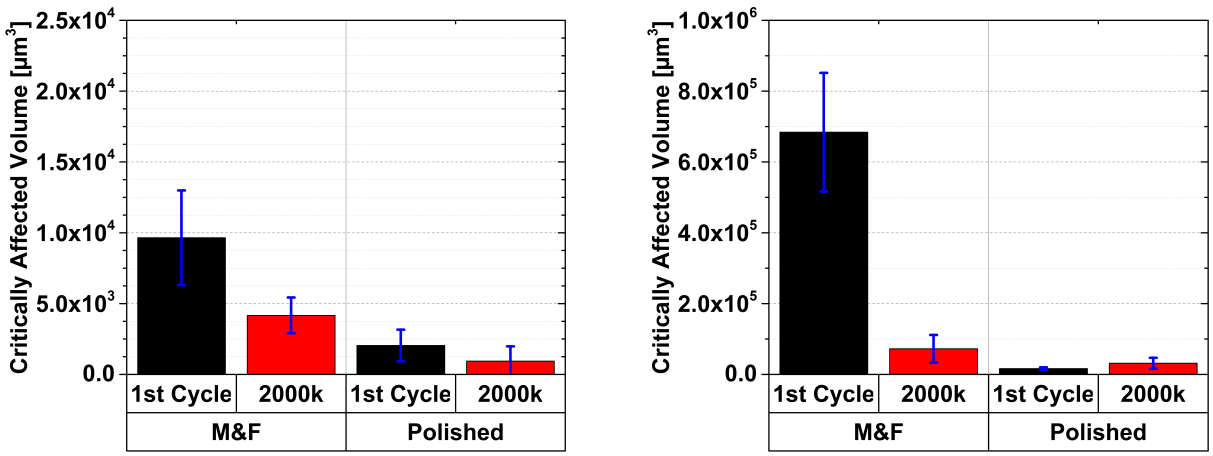

(a) (b)

Figure 54: Critically affected volume ($d \geq 1$) over one half cycle of the wear test; CHI wear test series, (a) base body, (b) counter body

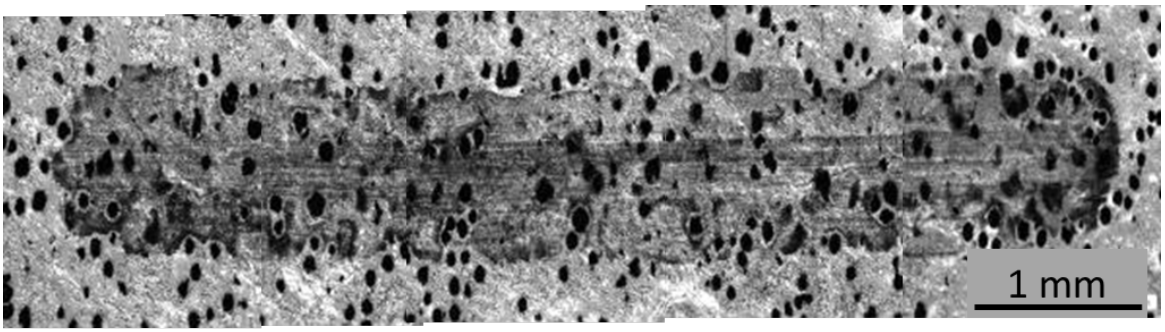

Figure 55: Macroscopic wear appearance after 2M wear test cycles; polished surface topography EN-GJS-HB 265

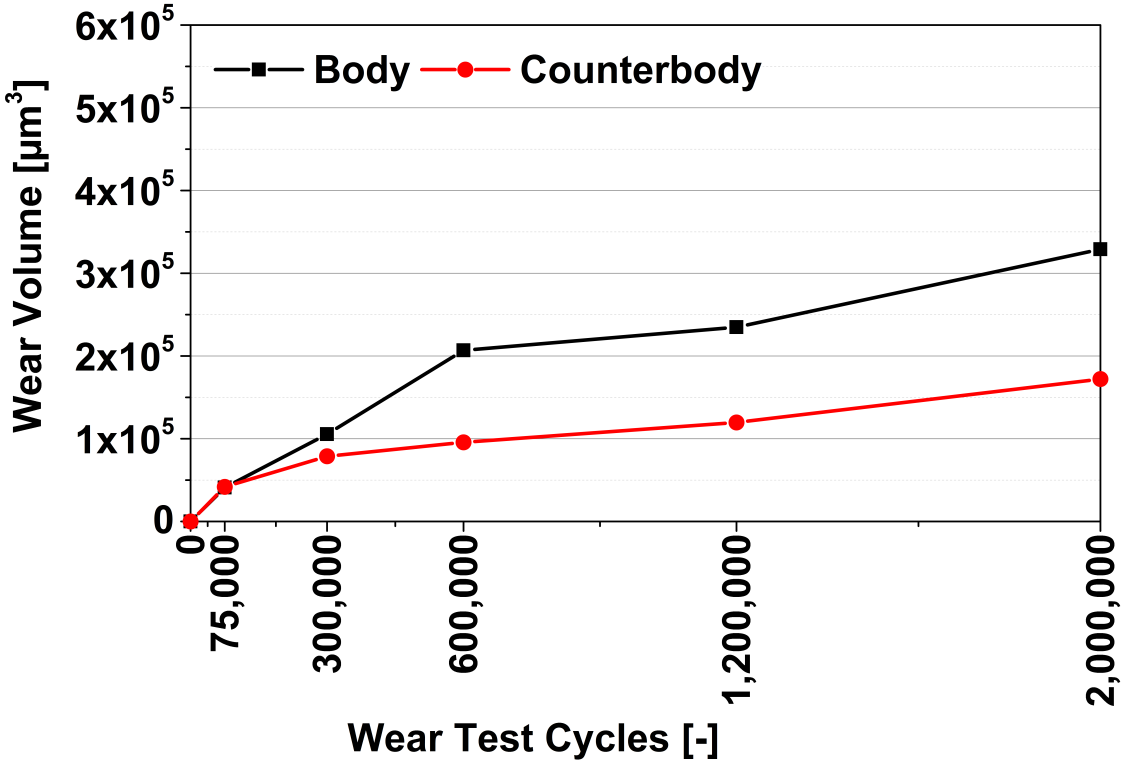

Figure 56: Characterisitc of the wear volume during wear testing time; milled surface topography 18CrNiMo7-6

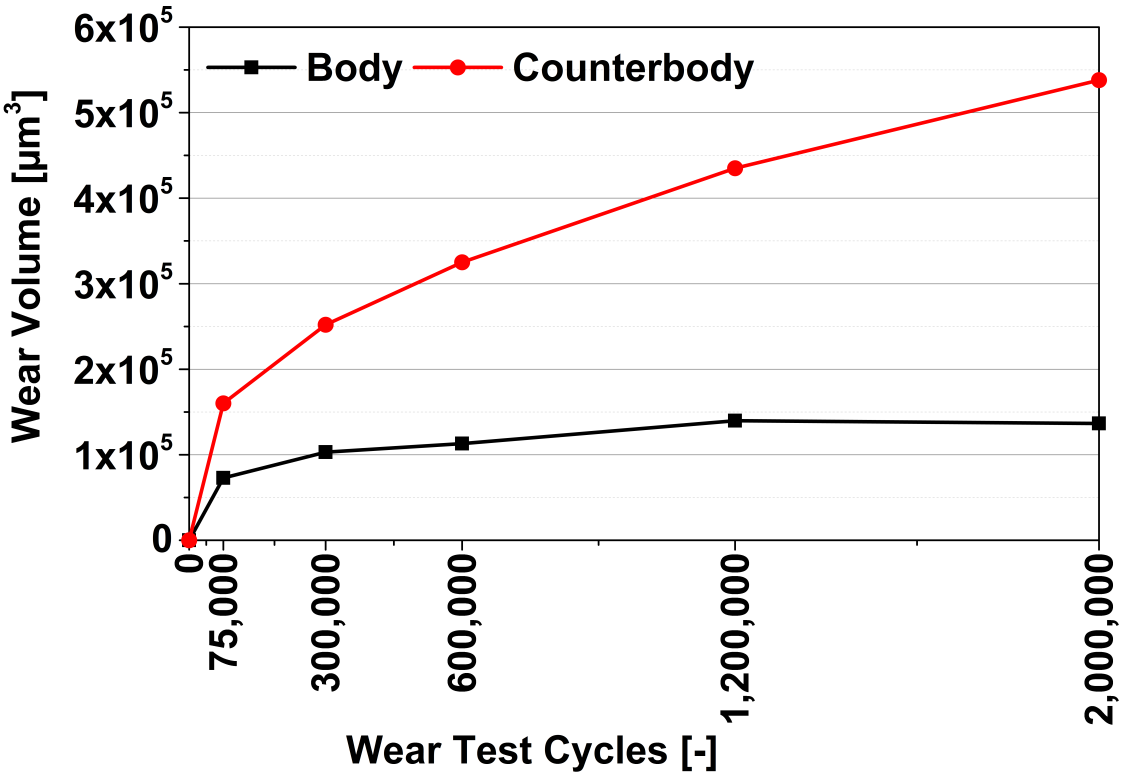

Figure 57: Characterisitc of the wear volume during wear testing time; ground surface topography 18CrNiMo7-6

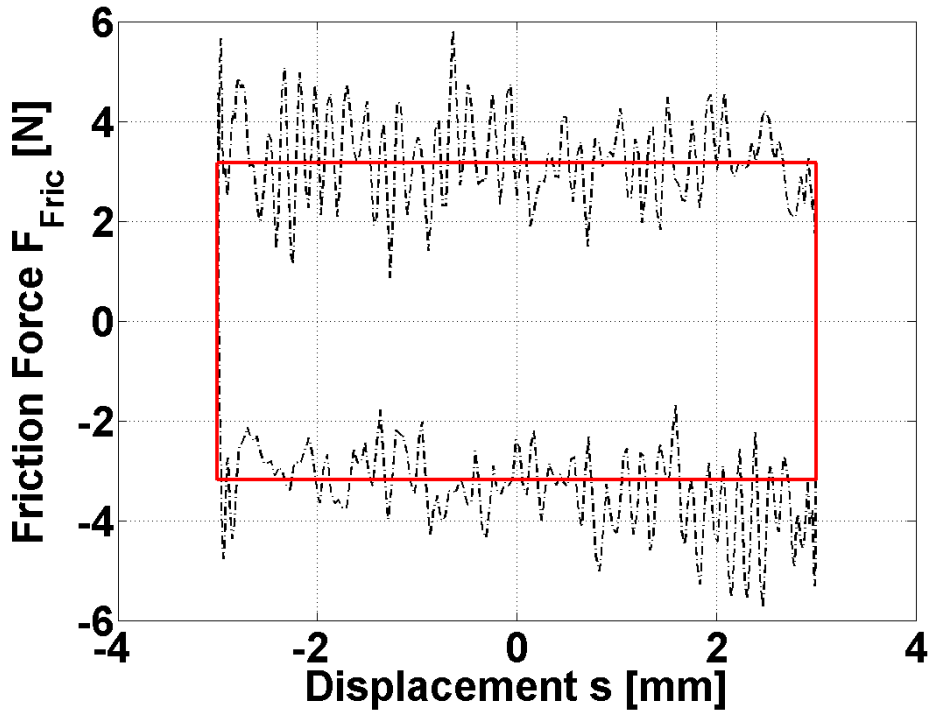

Figure 58: Approximation of the friction energy approach during one wear test cycles

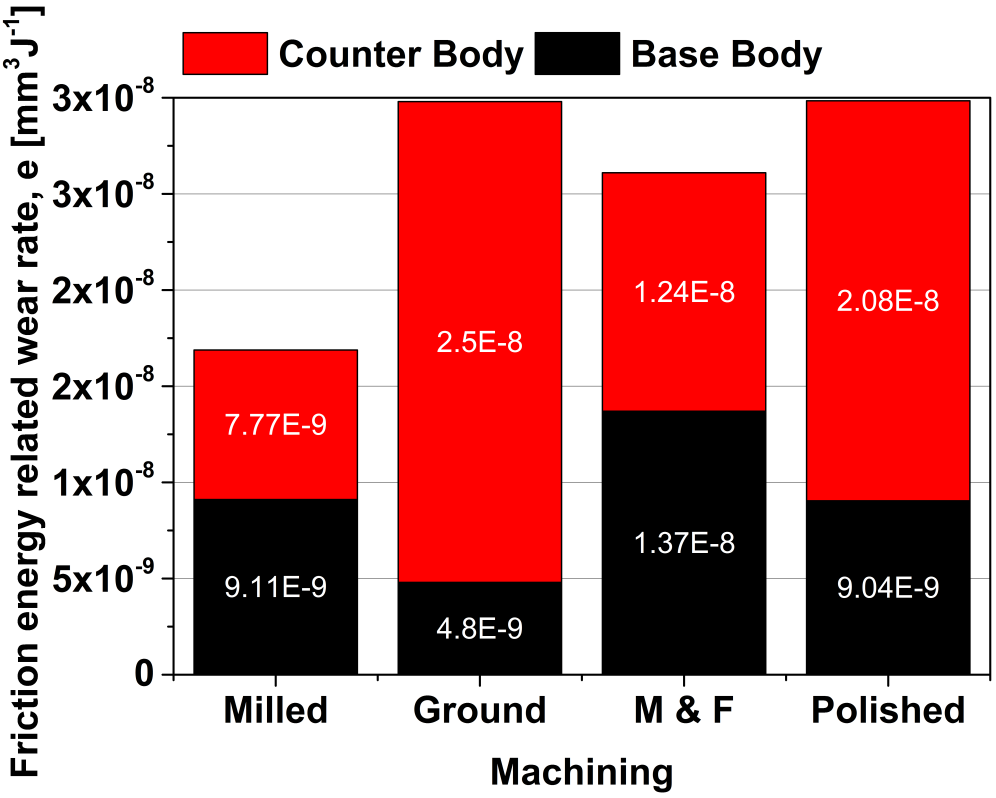

Figure 59: Friction energy related wear rate of CHI wear test series

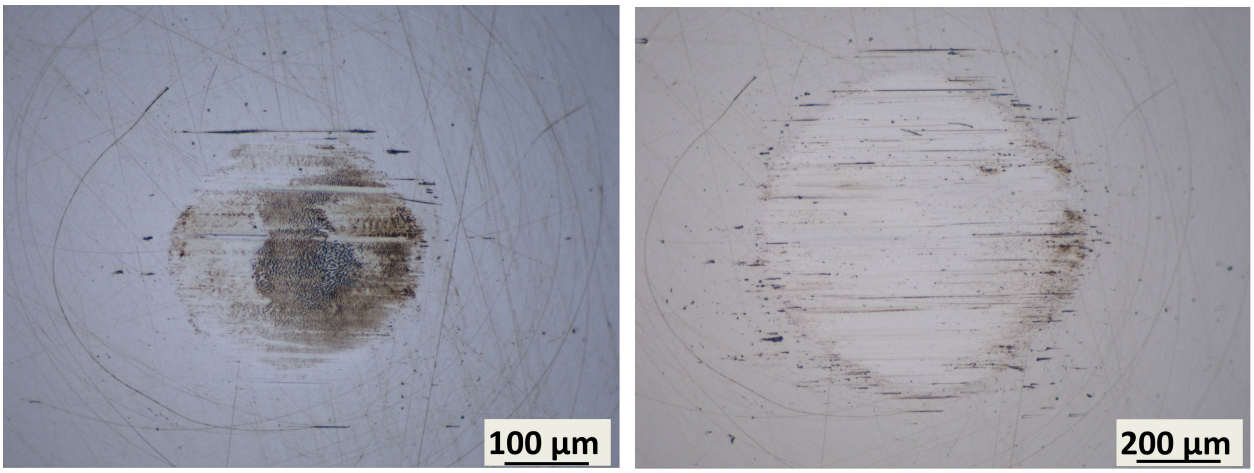

(a) (b)

Figure 60: Macroscopic wear appearances after (a) 75k wear test cycles (b) 2.0M wear test cycles; counter body of milled surface topography, 18CrNiMo7-6

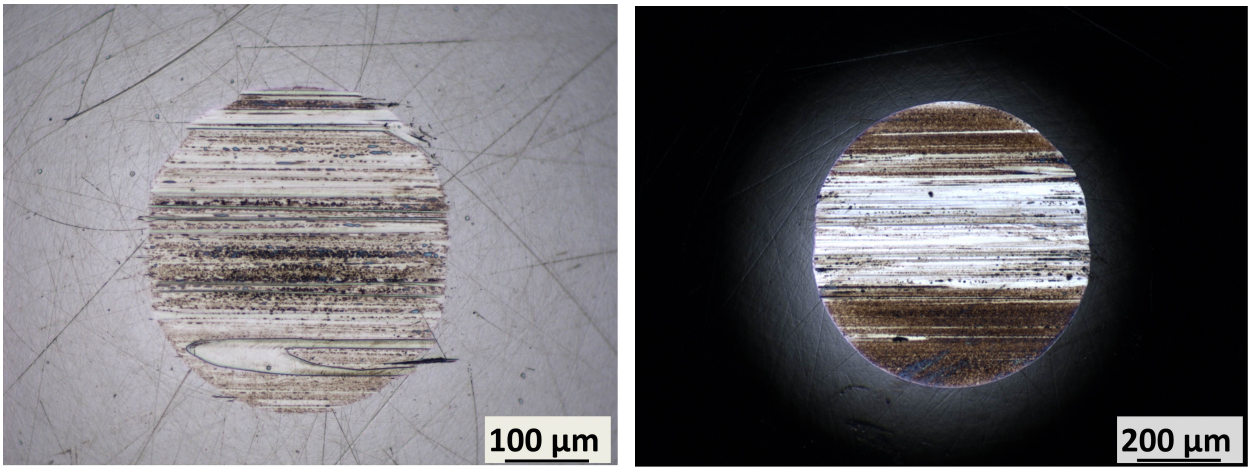

(a) (b)

Figure 61: Macroscopic wear appearances after (a) 75k wear test cycles (b) 2.0M wear test cycles; counter body of polished surface topography, EN-GJS-HB 265

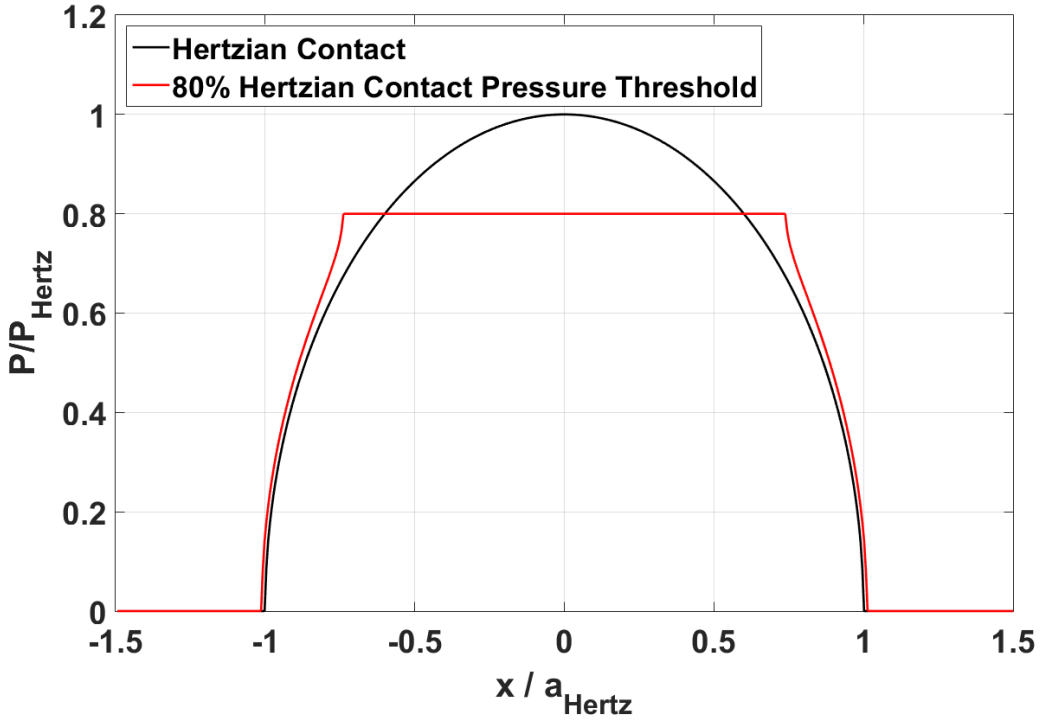

Figure 62: Comparison of linear-elastic and linear-elastic + ideal-plastic solution

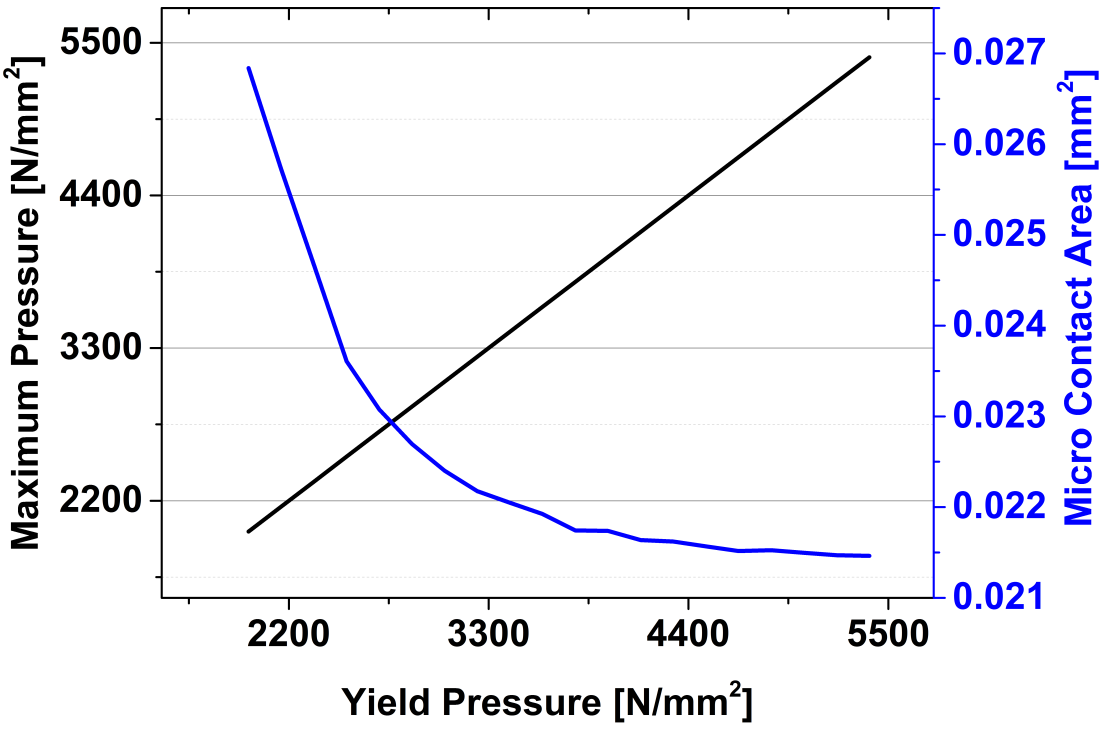

Figure 63: Contact Solver characteristics with the variation of the yielding pressure, milled & finished surface topography EN-GJS-HB 265

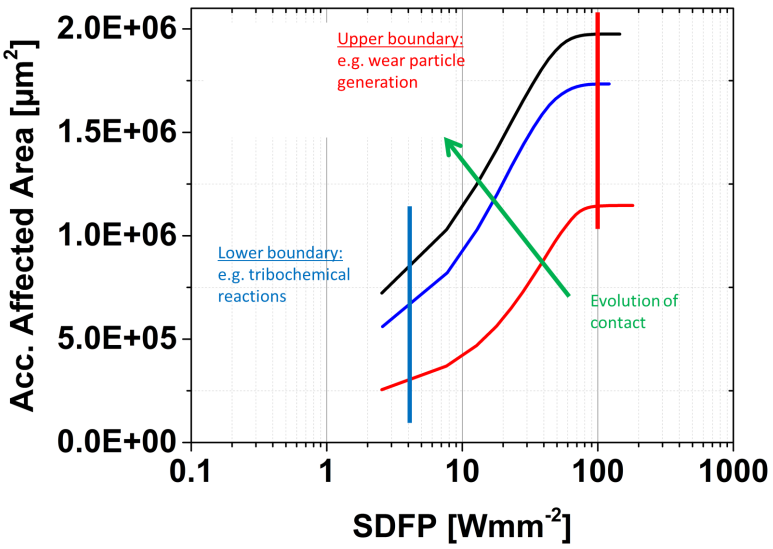

Figure 64: Design-space for highly wear resistant tribosystems

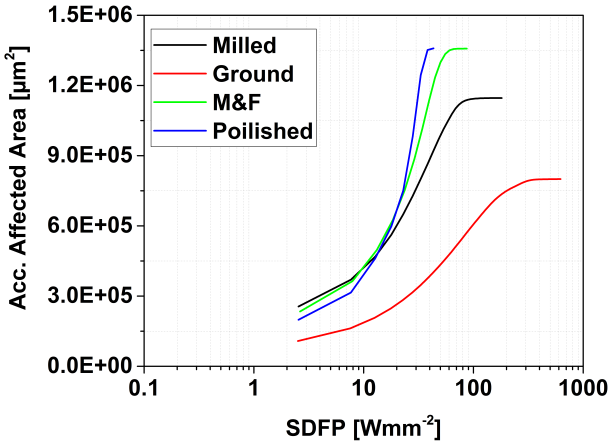

(a)

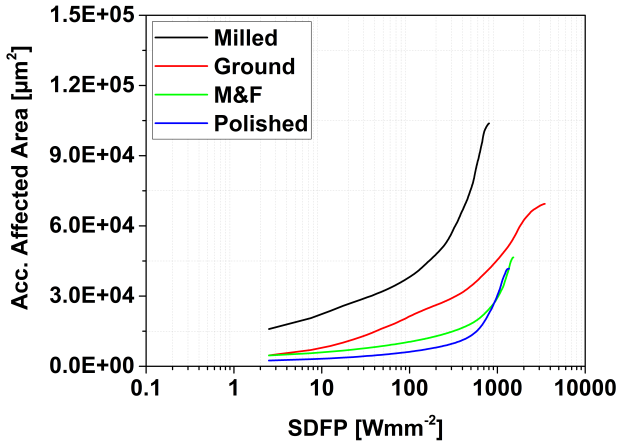

(b)

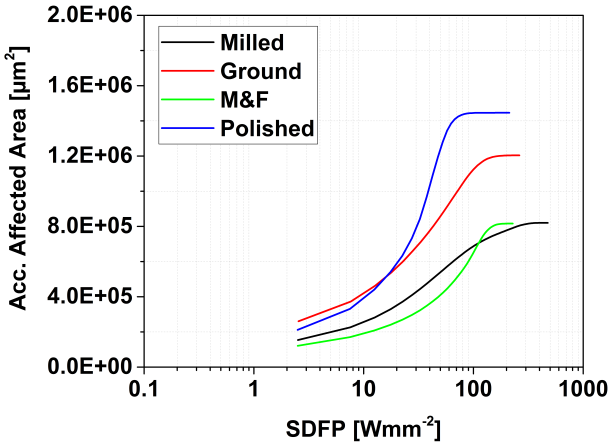

(c)

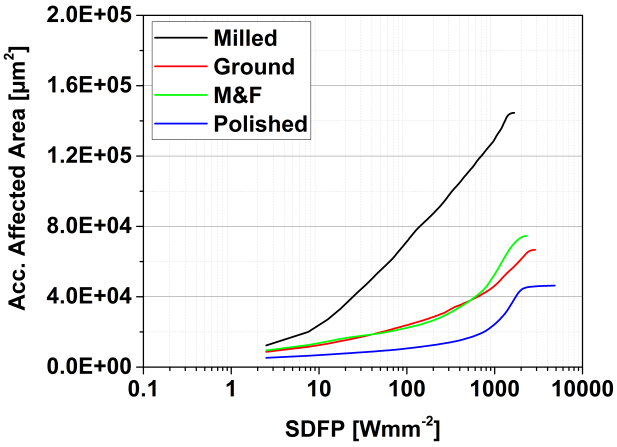

(d)

Figure 65: Comparison of initial SDFP vs A_{Aff} characteristics; (a) **BB**, CS wear test series, (a) **CB**, CS wear test series, (c) **BB**, CHI wear test series, (d) **CB**, CHI wear test series

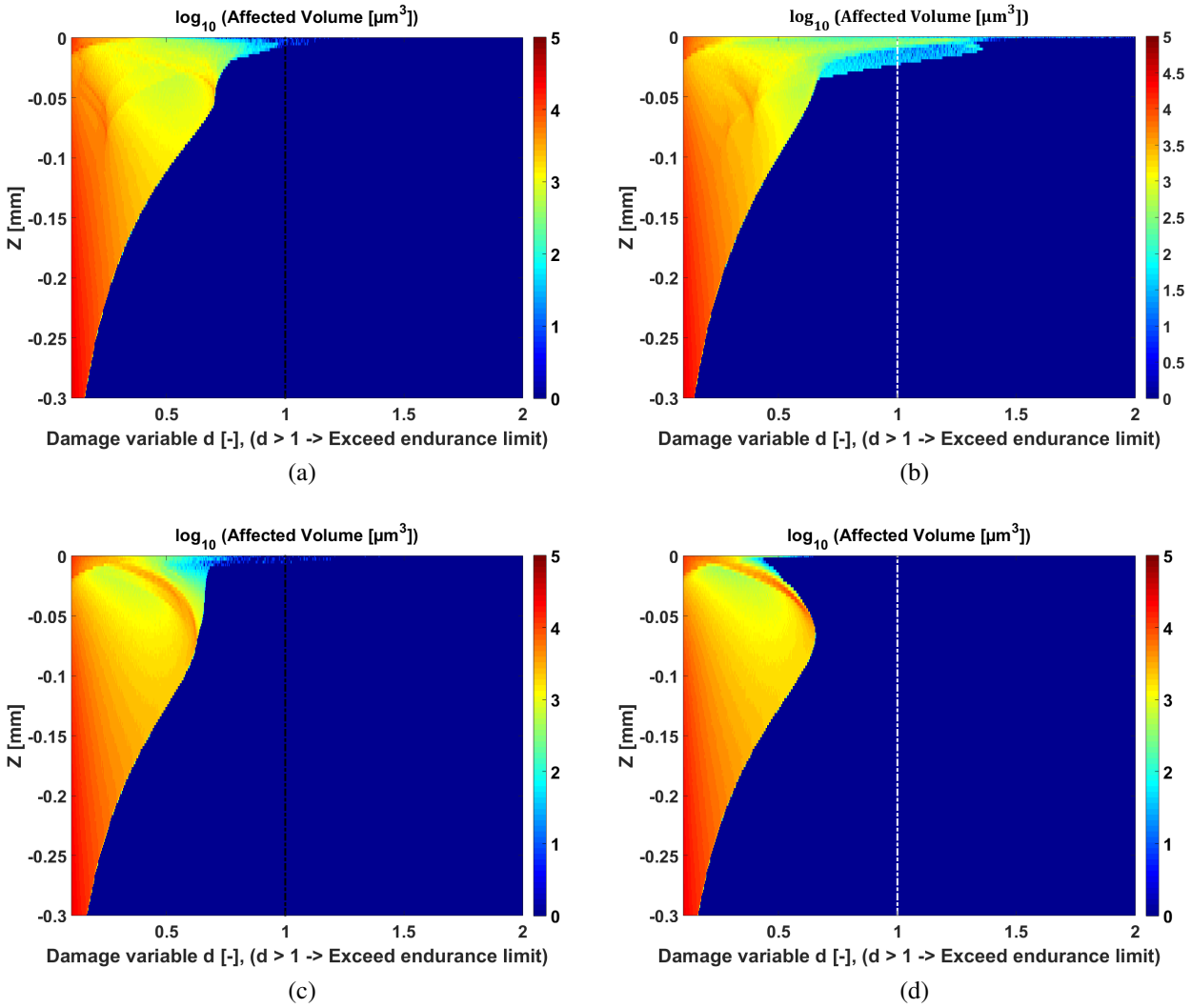

Figure 66: Contact fatigure criterion; Initial contact CS wear test series; (a) milled, (b) ground, (c) milled & finished, (d) polished

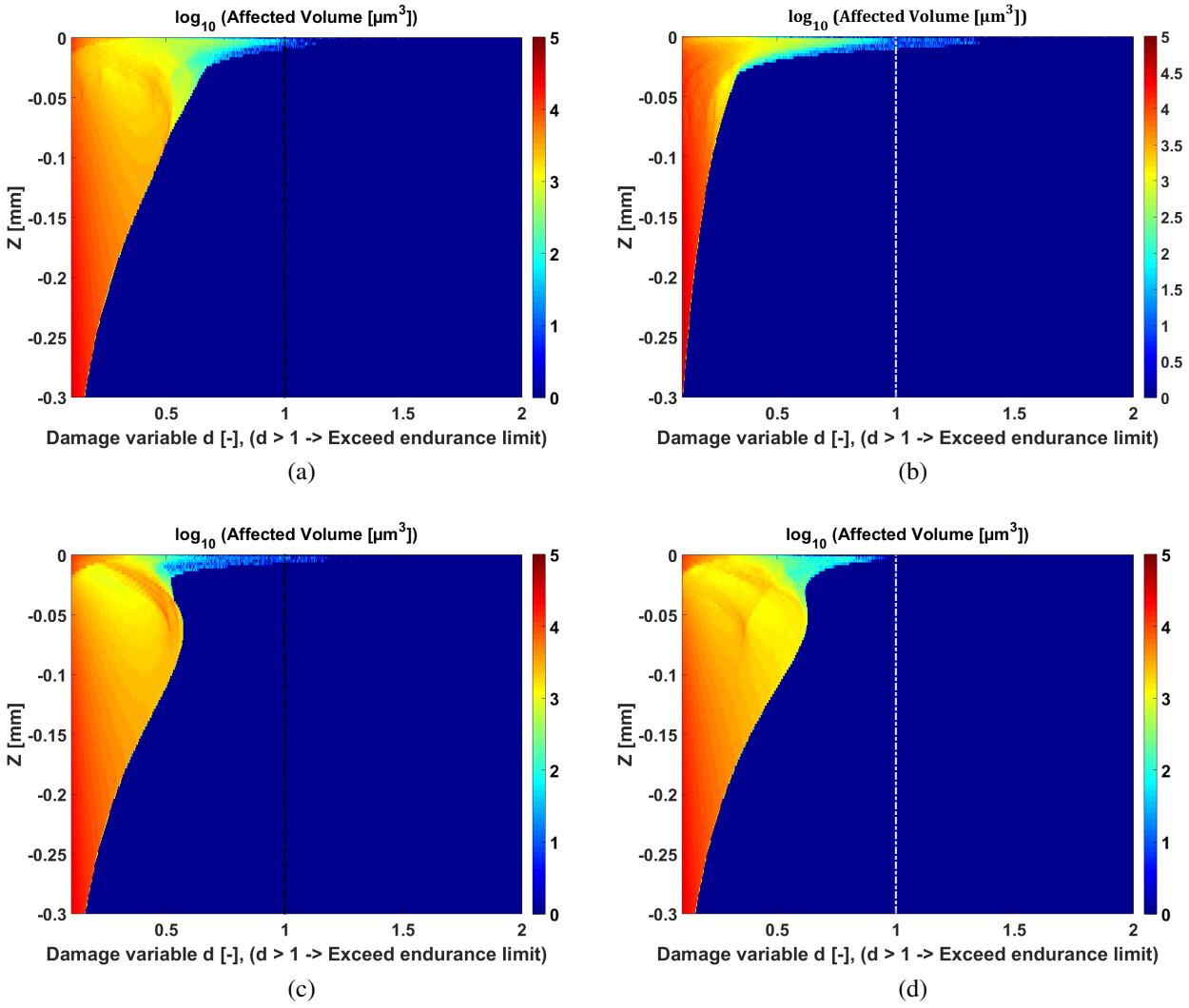

Figure 67: Contact fatigue criterion; Final contact CS wear test series; (a) milled, (b) ground, (c) milled & finished, (d) polished

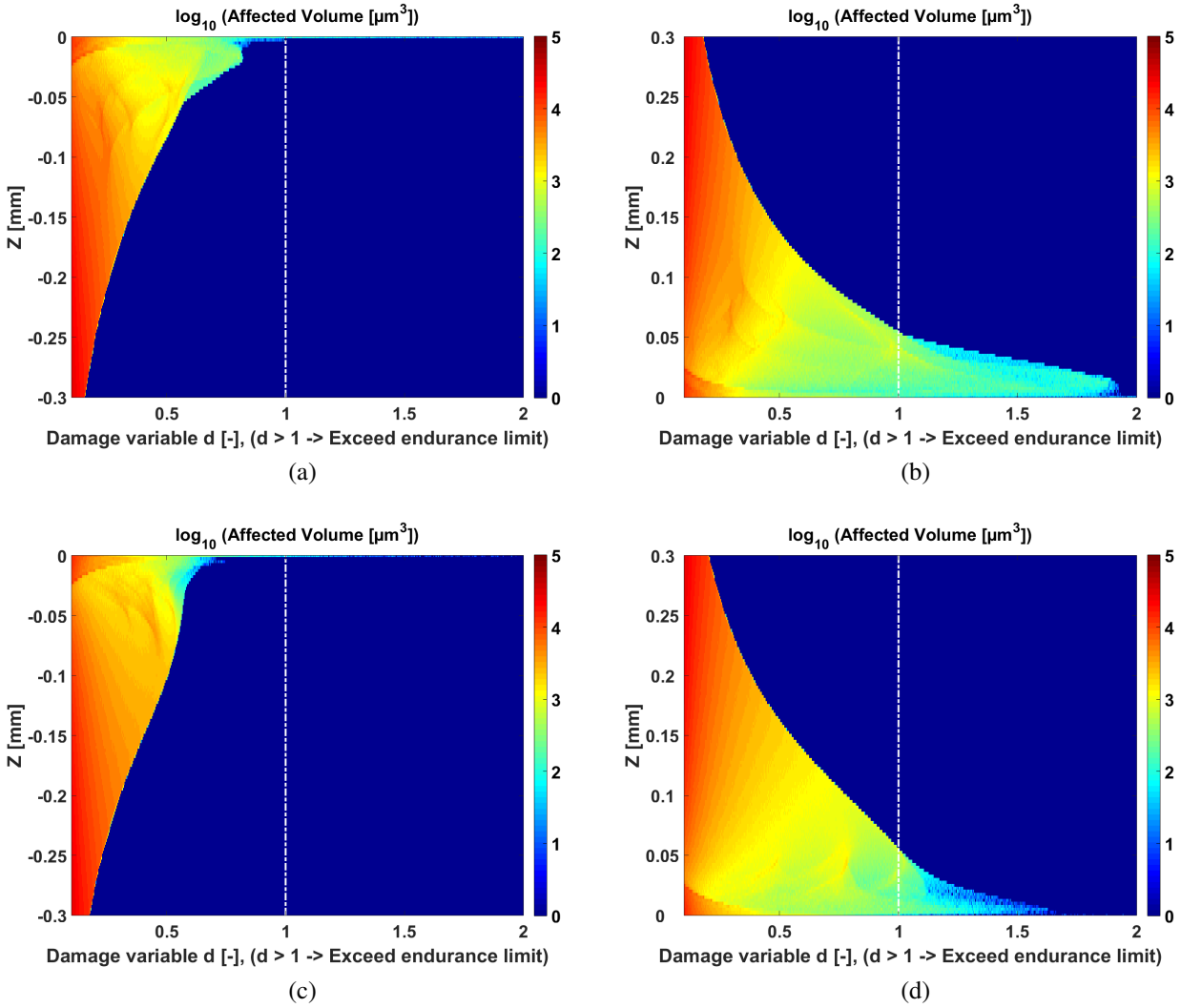

Figure 68: Contact fatigure criterion; Initial contact CHI wear test series; (a) milled base body, (b) milled counter body, (c) ground base body, (d) ground counter body

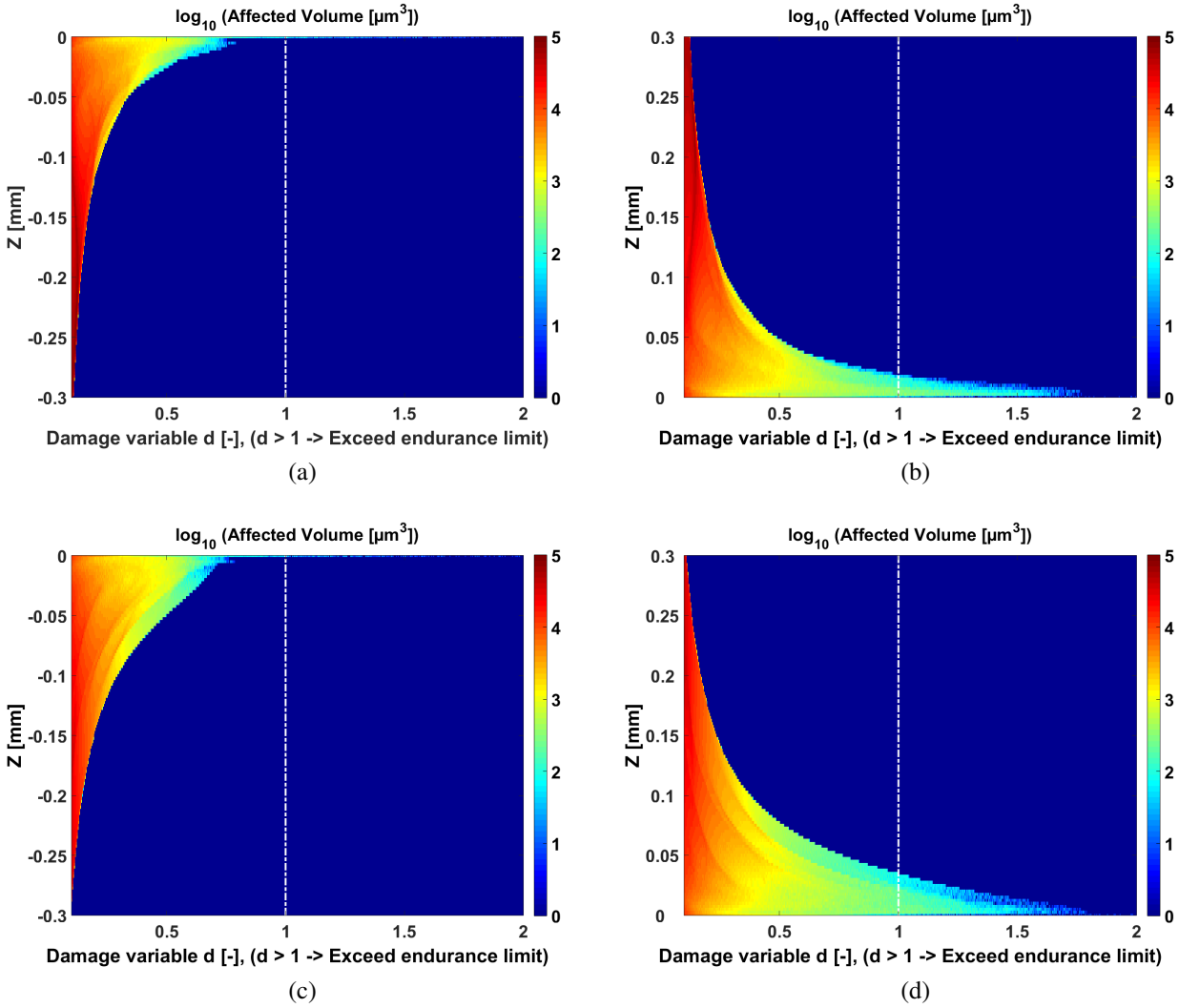

Figure 69: Contact fatigure criterion; Final contact CHI wear test series; (a) milled base body, (b) milled counter body, (c) ground base body, (d) ground counter body

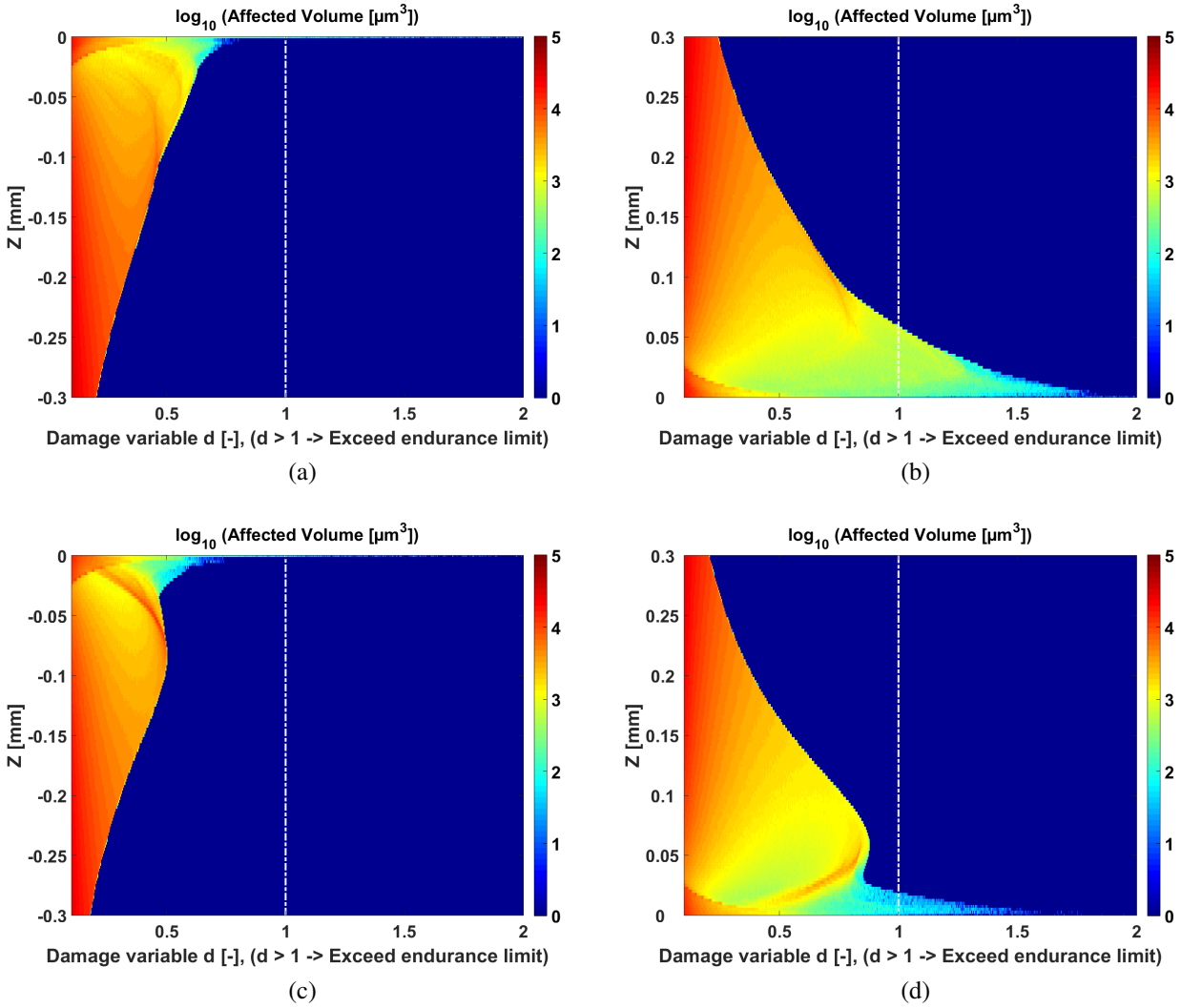

Figure 70: Contact fatigure criterion; Initial contact CHI wear test series; (a) milled & finished base body, (b) milled & finished counter body, (c) polished base body, (d) polished counter body

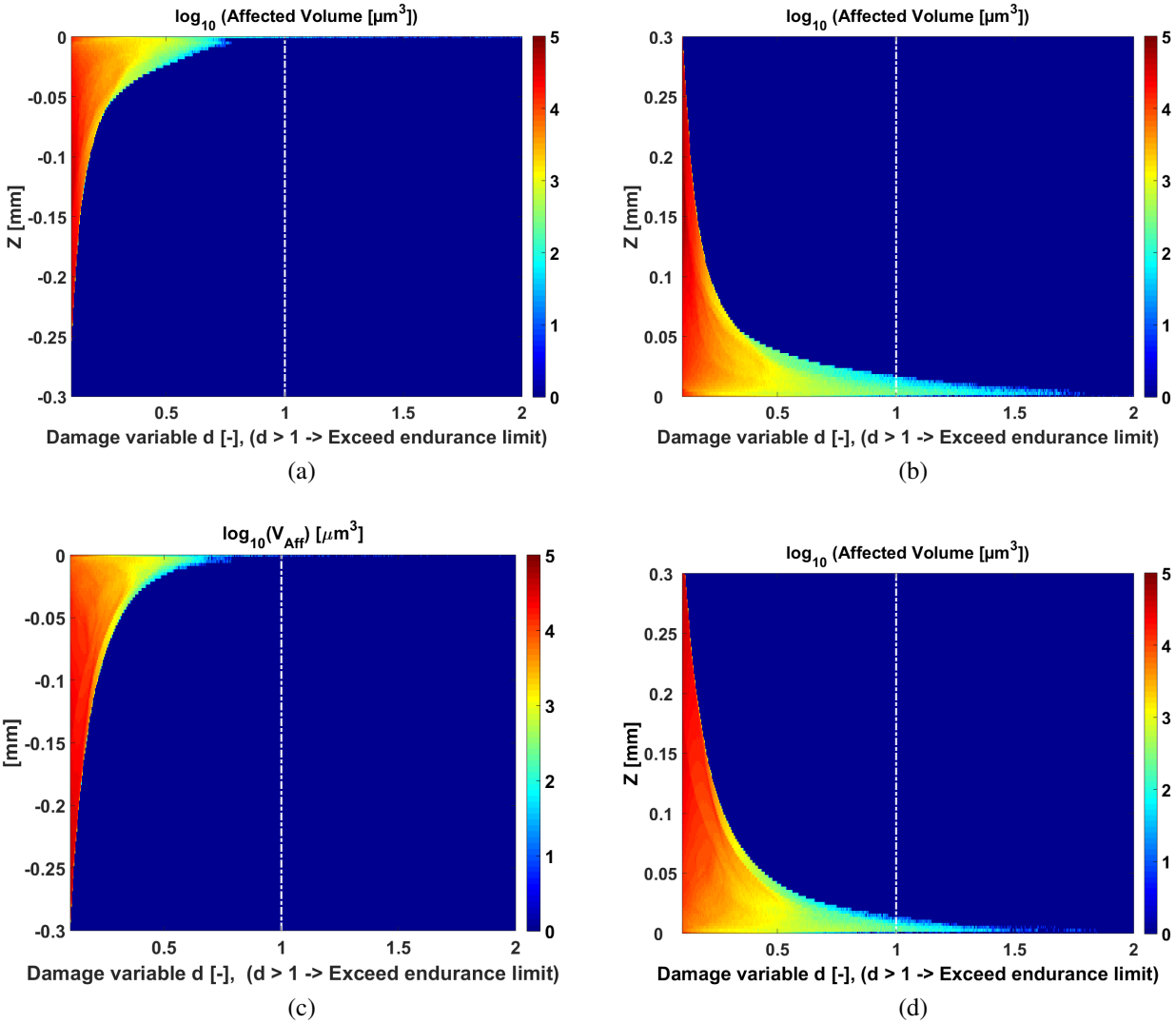

Figure 71: Contact fatigure criterion; Final contact CHI wear test series; (a) milled & finished base body, (b) milled & finished counter body, (c) polished base body, (d) polished counter body

References

[1] Holmberg, K. , Andersson, P. , Erdemir, A.: Global energy consumption due to friction in passenger cars: Tribol. Int. 47 (2012), p. 221–234

[2] Tzanakis, I. , Hadfield, M. , Thomas, B. , Noya, S.M. , Henshaw, I. , Austen, S.: Future perspectives on sustainable tribology: Renew. Sust. Energ. Rev. 16 (2012), p. 4126–4140

[3] Berns, H. , Theisen, W.: Ferrous Materials Steel and Cast Iron. Berlin Heidelberg : Springer, 2008

[4] Wang, S. Q. , Wang, L. , Zhao, Y. T. , Sun, Y. , Yang, Z. R.: Mild-to-severe wear transition and transition region of oxidative wear in steels: Wear 306 (2013), p. 311–320

[5] Kovalchenko, A. , Ajayi, O. , Erdemir, A. , Fenske, G.: Friction and wear behavior of laser textured surface under lubricated initial point contact: Wear 271 (2011), p. 1719–1725

[6] Mao, K.: Gear tooth contact analysis and its application in the reduction of fatigue wear: Wear 262 (2007), p. 1281–1288

[7] Amarnath, M. , Sujatha, C. , Swarnamani, S.: Experimental studies on the effects of reduction in gear tooth stiffness and lubricant film thickness in a spur geared system: Tribol. Int. 42 (2009), p. 340–352

[8] Dienwiebel, M. , Scherge, M.: Nanotribology in Automotive Industry. In: Gnecco, E. (Ed.) , Meyer, E. (Ed.): Fundamental of Friction and Wear on the Nanoscale: Springer (2007): p. 548 – 560

[9] Berlet, P. , Dienwiebel, M. , Scherge, M.: The effect of sample finishing on the tribology of metal/metal lubricated contacts: Wear 268 (2010), p. 1518–1523

[10] Scherge, M. , Shakhvorostov, D. , Pöhlmann, K.: Fundamental wear mechanism of metals: Wear 255 (2003), p. 395 - 400

[11] Stickel, D , Goeke, S , Geenen, K , Huth, S , WTheisen , Biermann, D , Fischer, A: Reciprocating sliding wear of case-hardened spheroidal cast iron against 100Cr6 under boundary lubrication: Proc. Inst. Mech. Eng. Part J J. Eng. Tribol. (2015)

[12] Shakhvorostov, D. et al.: Microstructure of tribologically induced nanolayers produced at ultra-low wear rates: Wear 263 (2007), p. 1259–1265

[13] Czichos, Horst: In: Tribology: A systems approach to the science and technology of friction, lubrication and wear, Vol. 1: Elsevier (1978)

[14] Williams, J. A. , Le, H. R.: Tribology and MEMS: Journal of Physics D: Applied Physics 39 (2006)

[15] Archard, J. F.: Contact and Rubbing of Flat Surfaces: Journal of Applied Physics 24 (1953), p. 981-988

[16] Archard, J. F. , Hirst, W.: The Wear of Metals under Unlubricated Conditions: Proc. R. Soc. London, Ser. A 236 (1956), p. 397–410

[17] Dowson, Duncan: Men of Tribology: Leonardo da Vinci (1452 - 1519): J. Tribol. 99 (1977), p. 382–386

[18] Czichos, H.: Tribological Processes. In: Tribology: A systems approach to the science and technology of friction, lubrication and wear, Vol. 1: Elsevier (1978): p. 45 – 175

[19] Fischer, Alfons: Subsurface microstructural alterations during sliding wear of biomedical metals. Modelling and experimental results: Comput. Mater. Sci. 46 (2009), p. 586 – 590

[20] Rigney, D.A: Transfer, mixing and associated chemical and mechanical processes during the sliding of ductile materials: Wear 245 (2000), p. 1 - 9

[21] Rigney, D.A. , Fu, X.Y. , Hammerberg, J.E. , Holian, B.L. , Falk, M.L.: Examples of structural evolution during sliding and shear of ductile materials: Scr. Mater. 49 (2003), p. 977 – 983

[22] Zum Gahr, K.-H.: Microstructure and Wear of Materials. New York : Elsevier, 1987

[23] Rigney, D.A.: The roles of hardness in the sliding behavior of materials: Wear 175 (1994), p. 63 - 69

[24] Ashby, M.F. , Lim, S.C.: Wear-mechanism maps: Scripta Metallurgica et Materialia 24 (1990), 805 - 810

[25] *ASM Handbook*. Vol. 4: *Heat treating*. ASM International (1991)

[26] Shakhvorostov, D. , Pöhlmann, K. , Scherge, M.: Structure and mechanical properties of tribologically induced nanolayers: Wear 260 (2006), p. 433–437

[27] Greenwood, J. A. , Williamson, J. B. P.: Contact of nominally flat surfaces: Proc. Roy. Soc. (1966)

[28] Whitehouse, D J.: Surface metrology: Measurement Science and Technology 8 (1997), 955

[29] Hertz, H.: Über die Berührung fester elastischer Körper: Journal für die Reine und Angewandte Mathematik 92 (1881), p. 156–171

[30] Stickel, D. , Fischer, A.: The Alteration of Micro-Contact Parameters during Run-In and their Effect on the Specific Dissipated Friction Power: Tribol. Int. (2015), p. 287–296

[31] Willner, K.: Fully Coupled Frictional Contact Using Elastic Halfspace Theory: ASME Journal of Tribology 130 (2008), p. 1 –8

[32] Polonsky, I. A. , Keer, L. M.: A numerical method for solving rough contact problems based on the multi-level multi-summation and conjugate gradient techniques: Wear 231 (1999), p. 206-219

[33] Polonsky, I. A. , Keer, L. M.: A Fast and Accurate Method for Numerical Analysis of Elastic Layered Contacts: J. Tribol. 122 (1999), p. 30-35

[34] Brandt, A. , Lubrecht, A. A.: Multilevel Matrix Multiplication and Fast Solution of Integral Equations: J. Comput. Phys. 90 (1990), p. 348–370

[35] Liu, S. , Wang, Q. , Liu, G.: A versatile method of discrete convolution and FFT (DC-FFT) for contact analyses: Wear 243 (2000), p. 101–111

[36] Wu, Jiunn-Jong: Simulation of rough surfaces with {FFT}: Tribol. Int. 33 (2000), p. 47 - 58

[37] Liu, S. , Wang, Q.: Studying Contact Stress Fields Caused by Surface Tractions With a Discrete Convolution and Fast Fourier Transform Algorithm: J. Tribol. 124 (2002), p. 36 – 45

[38] Hamilton, G M.: Explicit Equations for the Stresses beneath a Sliding Spherical Contact: Proc. Inst. Mech. Eng. Part C J. Mech. Eng. Sci. 197 (1983), p. 53-59

[39] Von Mises, R.: Mechanik der festen Körper im plastisch- deformablen Zustand: Nachrichten von der Gesellschaft der Wissenschaften zu Göttingen, Mathematisch-Physikalische Klasse (1913), p. 582-592

[40] Tresca, Henri-Edouard: Memoire sur l'ecoulement des corps solides soumis a de fortes pressions. Gauthier-Villars (1864)

[41] Rousselier, G.: Ductile fracture models and their potential in local approach of fracture: Nucl. Eng. Des. 105 (1987), p. 97-111

[42] Dang Van, K. , Paradopoulos, I. V.: High-Cycle Metal Fatigue: From Theory to Applications. Springer, Wien (1999)

[43] Dang Van, K.. , Maitournam, M.H.: On some recent trends in modelling of contact fatigue and wear in rail: Wear 253 (2002), p. 219–227

[44] Hanke, St , Samerski, I. , Schöfer, J. , Fischer, A.: The role of wear particles under multidirectional sliding wear: Wear 267 (2009), p. 1319-1324

[45] Fouvry, S. , Paulin, C.: An effective friction energy density approach to predict solid lubricant friction endurance: Application to fretting wear: Wear 319 (2014), p. 211 - 226

[46] Hamrock, B. J.: Fundamentals of Fluid Film Lubrication. Hoboken : Taylor and Francis (2004)

[47] Stribeck, R.: Die wesentlichen Eigenschaften der Gleit- und Rollenlager. Julius Springer (1903)

[48] Tallian, T. E.: On competing failure modes in rolling contact: ASLE Transactions 10 (1967), p. 418 – 439

[49] Reynolds, Osborne: On the Theory of Lubrication and Its Application to Mr. Beauchamp Tower's Experiments, Including an Experimental Determination of the Viscosity of Olive Oil: Philos. Trans. R. Soc. London, Ser. A 177 (1886), p. 157–234

[50] Dowson, D. , Higginson, G. R.: A Numerical Solution to the Elasto-Hydrodynamic Problem: Proc. Inst. Mech. Eng. C J. Mech. Eng. Sci. 1 (1959), p. 6-15

[51] Hardy, W. B. , Doubleday, Ida: Boundary Lubrication. The Paraffin Series: Proc. Roy. Soc. A 100 (1922), p. 550–574

[52] Zhang, Yongbin: Boundary lubrication - An important lubrication in the following time: J. Mol. Liq. 128 (2006), p. 56 - 59

[53] Dowson, D.: Thin Films in Tribology. In: D. Dowson, C. M. Taylor T. H. C. Childs M. G. (Ed.) , Dalmaz, G. (Ed.): Tribology Series, Vol. Volume 25: Elsevier (1993): 3-12

[54] Hsu, S.M. , Gates, R.S.: Boundary lubricating films: formation and lubrication mechanism: Tribology International 38 (2005), 305 - 312. – Boundary Lubrication

[55] Ghanbarzadeh, Ali , Wilson, Mark , Morina, Ardian , Dowson, Duncan , Neville, Anne: Development of a new mechano-chemical model in boundary lubrication: Tribol. Int. (2014)

[56] Bosman, R. , Hol, J. , Schipper, D. J.: Running-in of metallic surfaces in the boundary lubrication regime: Wear 271 (2011), p. 1134-1146

[57] Goeke, S. et al.: Enhancing the Surface Integrity of Tribologically Stressed Contacting Surfaces by an Adjusted Surface Topography: Procedia CIRP 13 (2014), p. 214–218

[58] Ungureanu, I. , Spinu, S.: A simplified model for pressure distribution in elastic - perfectly plastic contact: Annals of the Oradea University IX (2010), p. 1–8

[59] Tabor, D.: The Hardness of Metals. ClarendonP (1951)

[60] Maschinenbau, Forschungskuratorium: Rechnerischer Festigkeitsnachweis für Maschinenbauteile. VDMA-Verlag (2012)

[61] Gabelli, A. , Lai, J. , Lund, T. , Ryden, K. , Strandell, I. , Morales-Espejel, G. E.: The fatigue limit of bearing steels - Part II: Characterization for life rating standards: Int. J. Fatigue 38 (2012), p. 169 - 180

[62] Blau, Peter J.: On the nature of running-in: Tribol. Int. 38 (2006), p .1007 - 1012

[63] I.V., Kragelsky , Dobychin, M. N. , Kombalov, V. S.: Friction and wear: calculation methods. Oxford ; New York : Pergamon Press, 1982. – ix, 464 p.– p.

[64] Fuller, K. N. G. , Tabor, D.: The Effect of Surface Roughness on the Adhesion of Elastic Solids: Proc. Roy. Soc. A 345 (1975), p. p. 327–342

[65] Godet, Maurice: Third-bodies in tribology: Wear 136 (1990), p. 29–45

[66] Samerski, I. , Vdovak, J. , Schäffer, J. , Fischer, A.: The transition between high and low wear regimes under multidirectional reciprocating sliding: Wear 267 (2009), p. 1446-1451

[67] Stickel, D. , Wimmer, M.A. , Fischer, A.: Analyzing pin-on-ball wear tests by means of the Greenwood - Williamson contact model: Wear 301 (2013), p. 4–10

[68] Ponter, Alan R. , Chen, H.F. , Ciavarella, M. , Specchia, G.: Shakedown analyses for rolling and sliding contact problems: Int. J. Solids Struct. 43 (2006), p.4201 - 4219

[69] Scherge, M , Pöhlmann, K , Gerve, A: Wear measurement using radionuclide-technique (RNT): Wear 254 (2003), p. 801 - 817

[70] Wimmer, M.A. , Laurent, M.P. , Mathew, M.T. , Nagelli, C. , Liao, Y. , Marks, L.D. , Jacobs, J.J. , Fischer, A.: The effect of contact load on CoCrMo wear and the formation and retention of tribofilms: Wear 332 - 333 (2015), p. 643 - 649

[71] Bosman, R.: Mild Microscopic Wear Modeling in the Boundary Lubrication Regime. Enschede, the Netherlands: University of Twente: Diss.: 2011

[72] Nelias, D. , Antaluca, E. , Boucly, Vincent , Cretu, S.: A Three-Dimensional Semianalytical Model for Elastic-Plastic Sliding Contacts: ASME Journal of Tribology 129 (2007), 761 - 771

[73] Nyqvist, J. , Kadiric, A. , Ioannides, S. , Sayles, R.: Semi-analytical model for rough multilayered contacts: Tribol. Int. 87 (2015), p. 98 - 112

[74] Chen, W. W. , Zhou, K. , Keer, L. M. , Wang, Q. J.: Modeling elasto-plastic indentation on layered materials using the equivalent inclusion method: Int. J. Solids Struct. 47 (2010), p. 2841-2854

[75] Zhou, Kun , Chen, W. W. , Keer, Leon M. , Wang, Q. J.: A fast method for solving three-dimensional arbitrarily shaped inclusions in a half space: Comput. Meth. Appl. Mech. Eng. 198 (2009), p. 885-892

[76] Zhou, K. , Chen, H.W. W. , Keer, L. M. , Xiaolan, A. , Sawamiphakdi, K. , Glaws, Peter , Wang, Q. J.: Multiple 3D inhomogeneous inclusions in a half space under contact loading: Mechanics of Materials 43 (2011), p. 444-457

[77] Stickel, D. , Fischer, A. , Bosman, R.: Specific dissipated friction power distributions of machined carburized martensitic steel surfaces during running-in: Wear 330 - 331 (2015), p. 32 - 41

[78] Desimone, H. , Bernasconi, A. , Beretta, S.: On the application of Dang Van criterion to rolling contact fatigue: Wear 260 (2006), 567 - 572

[79] Bernasconi, A. , Davoli, P. , Filippini, M. , Foletti, S.: An integrated approach to rolling contact sub-surface fatigue assessment of railway wheels: Wear 258 (2005), p. 973 - 980

[80] Cardoso, N.F.R. , Martins, R.C. , Seabra, J.H.O. , Igartua, A. , Rodríguez, J.C. , Luther, R.: Micropitting performance of nitrided steel gears lubricated with mineral and ester oils: Tribol. Int. 42 (2009), p. 77 - 87

[81] Mughrabi, H. , Höppel, H. W.: Cyclic deformation and fatigue properties of very fine-grained metals and alloys: Int. J. Fatigue 32 (2010), p. 1413 - 1427

[82] Um, H. Y. , Yoon, E. Y. , Lee, D. J. , Lee, C. S. , Park, L. J. , Lee, S. , Kim, H. S.: Hollow cone high-pressure torsion: Microstructure and tensile strength by unique severe plastic deformation: Scripta Materialia 71 (2014), p. 41 - 44

[83] Zhilyaev, A. P. , Langdon, T. G.: Using high-pressure torsion for metal processing: Fundamentals and applications: Progress in Materials Science 53 (2008), p. 893 - 979

[84] Hummel, S. R.: Development of a galling resistance test method with a uniform stress distribution: Tribol. Int. 41 (2008), p. 175 - 180

[85] Waite, R.A. , Hummel, S.R. , Herr, A. , Dalton, G.: Analysis of the stress field in a threshold-galling test: Tribol. Int. 39 (2006), 1421 - 1427

[86] Vinogradov, A. , Hashimoto, S.: Multiscale Phenomena in Fatigue of Ultra-Fine Grain Materials; an Overview: Material Transactions 42 (2001), p. p. 74–84

[87] Mughrabi, H.: Fatigue, an everlasting materials problem - still en vogue: Procedia Engineering 2 (2010), p. 3 - 26

[88] Spriestersbach, D. , Grad, P. , Kerscher, E.: Crack Initiation Mechanisms and Threshold Values of Very High Cycle Fatigue Failure of High Strength Steels: Procedia Engineering 74 (2014), p. 84 - 91. – {XVII} International Colloquium on Mechanical Fatigue of Metals (ICMFM17)

[89] Sobahan, M. , Mizukami, S. , Fukuda, R. , Morita, S. , Ohno, N.: High-pressure behavior and tribological properties of wind turbine gear oil: J. Mech. Sci. Technol. 24 (2010), p. 111-114